

© Copyright by Mohammad Shabouei, 2016

All Rights Reserved

**THEORETICAL AND NUMERICAL STUDY IN POROUS
MEDIA: SOLUTION VERIFICATION AND VISCOUS
FINGERING INSTABILITY**

A Dissertation

Presented to

the Faculty of the Department of Civil and Environmental Engineering

University of Houston

In Partial Fulfillment

of the Requirements for the Degree of

Doctor of Philosophy

in Civil and Environmental Engineering

by

Mohammad Shabouei

August 2016

**THEORETICAL AND NUMERICAL STUDY IN POROUS
MEDIA: SOLUTION VERIFICATION AND VISCOUS
FINGERING INSTABILITY**

Mohammad Shabouei

Approved:

Chair of the Committee
Kalyana B. Nakshatralla, Assistant Professor
Department of Civil and Environmental Engineering

Committee Members:

Kaspar J. Willam, Professor
Department of Civil and Environmental Engineering

Cumaraswamy Vipulanandan, Professor
Department of Civil and Environmental Engineering

Ahmet Omurtag, Associate Professor
Department of Biomedical Engineering

Debora Rodrigues, Associate Professor
Department of Civil and Environmental Engineering

Suresh. K. Khator, Associate Dean
Cullen College of Engineering

Roberto Ballarini, Chair
Department of Civil and Environmental Engineering

**THEORETICAL AND NUMERICAL STUDY IN POROUS
MEDIA: SOLUTION VERIFICATION AND VISCOUS
FINGERING INSTABILITY**

An Abstract
of a
Dissertation
Presented to
the Faculty of the Department of Civil and Environmental Engineering
University of Houston

In Partial Fulfillment
of the Requirements for the Degree of
Doctor of Philosophy
in Civil and Environmental Engineering

by
Mohammad Shabouei

August 2016

Abstract

The central objective of this dissertation is to develop predictive mathematical and numerical tools for modeling flow and transport in porous media. Specifically, the dissertation presents mathematical models for coupling flow and transport in porous media at the continuum scale; develops associated predictive numerical formulations to solve the resulting governing equations; derives mechanics-based verification methods to assess numerical accuracy; obtains scaling laws pertaining to mixing, miscible displacement and viscous fingering; and highlights the pitfalls of several popular stabilized finite element formulations in simulating physical instabilities like viscous fingering. Success of several important technological endeavors (e.g., hydraulic fracturing, geological carbon-dioxide sequestration) requires a fundamental understanding of coupled processes at multiple scales. Although tremendous progress has been made in the areas of flow and transport (and, of course, in the areas of mechanics, geochemistry, digital imaging, experimental techniques), time has come for another wave of intense research to model coupled processes. Future advancements certainly depend on *predictive* numerical simulations and careful experiments. The current modeling tools are good at providing qualitative trends, however they are not necessarily accurate to provide predictive quantitative results, which are required for the success of the aforementioned technological endeavors. The main motivation of this dissertation is to improve the predictive capabilities of the continuum modeling tools for flow and transport in porous media. *First*, a novel mechanics-based accuracy assessment methodology is developed for porous media models and is used to investigate the performance of finite element stabilized formulations with respect to accuracy and convergence. *Second*, a mathematical model is presented to study the combined effect of temperature and concentration on miscible displacement and viscous fingering. It is also shown that the popular numerical stabilized formulations, which are primarily

developed to avoid numerical instabilities, may also eliminate physical instabilities. Hence, care should be exercised in using these formulations to study physical instabilities like viscous fingering. *Third*, scaling laws and reduced-order models are derived for double-diffusive miscible viscous fingering. One of the main findings is that the evolution of the variances of the concentration and temperature fields scales with the norm of the gradient of the velocity. *Fourth*, a theoretical and numerical study is performed on viscous fingering in a porous medium which has two dominant pore-networks with possible mass transfer across them. A linear stability analysis is also performed to understand the effects of various parameters (e.g., log-mobility ratio, permeabilities of micro- and macro-pore networks, mass transfer between the pore-networks) on the physical instability.

To Syrian children

who have not been at school since 2011.

Acknowledgements

I am grateful to my advisor, Dr. Kalyana Babu Nakshatrala for his valuable guidance and support during the course of my research. I would like to thank my friends and fellows in CAML, Dr. Maruti Kumar Mudunuru, Saeid Karimi, Justin Chang, Can Xu, Seyedeh Hanie Seyed Joodat, and Mohammad Sarraf Joshaghani, for our arguments and their valuable questions and suggestions at various occasions. My deepest gratitude goes to my beloved family; my Mom, Dad, Shokoofeh, Maryam, Mahdi, Mohsen, and Zahra. I have started this journey because of their confidence in my abilities. Without their love, sacrifice and support, this accomplishment would not have been possible.

Lastly, I acknowledge the contributions of many great researchers who work in this field. I try to learn from them.

Table of Contents

- Abstract vi
- Acknowledgments ix
- Table of Contents x
- List of Figures xiii
- List of Tables xxii
- 1 INTRODUCTION AND MOTIVATION 1**
- 2 MECHANICS-BASED SOLUTION VERIFICATION FOR POROUS MEDIA MODELS 5**
 - 2.1 Introduction 5
 - 2.1.1 Validation and Verification (V&V) 7
 - 2.1.2 *A posteriori* techniques 9
 - 2.1.3 An outline of the chapter 10
 - 2.2 Darcy and Darcy-Brinkman models 10
 - 2.3 Mathematical properties: Statements and derivations 13
 - 2.4 Steady-state numerical results 24
 - 2.4.1 Body force problem 27
 - 2.4.2 Lid-driven cavity problem 28
 - 2.4.3 Pipe bend problem 30
 - 2.4.4 Pressure slab problem 36
 - 2.4.5 Pressure driven problem 37
 - 2.4.6 Vorticity results 39
 - 2.4.7 Synthetic reservoir data: Marmousi dataset 39
 - 2.5 Transient case 43
 - 2.5.1 Governing equations 43
 - 2.5.2 Mathematical properties 45

2.5.3	Representative numerical results	46
2.6	Concluding remarks	48
3	VISCOUS FINGERING AND MIXING FOR DOUBLE DIFFU- SION MODEL: EFFECT OF TEMPERATURE AND NUMERI- CAL STABILIZATION	50
3.1	Introduction to viscous fingering phenomena	50
3.2	Governing equations: Coupled flow, transport, and thermal processes	53
3.3	Computational framework: Mixed and stabilized finite element formu- lations	56
3.3.1	Mixed two-field weak formulation for Darcy equations	56
3.3.2	Stabilized formulations for ADR equations	57
3.3.3	Violation of maximum principle and non-negative constraint .	60
3.4	A reduced order model for mixing	61
3.5	Effect of temperature on viscous fingering	68
3.5.1	A qualitative study	70
3.5.2	A quantitative study	77
3.6	Numerical results: Impact of employing stabilized formulations	80
3.7	Concluding remarks	83
4	VISCOUS FINGERING IN POROUS MEDIA WITH DOUBLE PERMEABILITY: MODEL, STABILITY, AND NUMERICAL SOLUTION	86
4.1	Introduction and background	86
4.2	Governing equations and linearization	88
4.2.1	Two-scale expansion and linearization	90
4.3	Model problem: Rectilinear flow	92
4.3.1	Problem description	92

4.3.2	Non-dimensionalization	93
4.3.3	Base-state solution	94
4.4	Stability analysis	95
4.4.1	Special case: Isotropic double permeability ($K_1 = K_2 = K$ and $k_1 = k_2 = k$)	97
4.4.2	Special case: Isotropic single permeability ($K_1 = K_2 = k_1 =$ $k_2 = k$)	97
4.4.3	Initial growth rate	97
4.4.4	Parametric study for linear stability	103
4.4.5	Concentration profiles	107
4.5	Concluding remarks	111
5	CONCLUSION AND FUTURE RESEARCH DIRECTIONS . . .	113
	Bibliography	116

List of Figures

Figure 2.1	This figure shows the typical employed structured finite element. We use Q2P1 and P2P1 mixed interpolations for unknowns (i.e., second-order interpolation for the velocity field, and first-order for the pressure field).	26
Figure 2.2	Body force problem: The computational domain is a square with $L = 1$. The prescribed conservative body force is $\rho \mathbf{b}(\mathbf{x}) = 10 \times [\sin(\pi x), \cos(\pi y)]$. Homogeneous velocity is enforced on the entire boundary (i.e., $\Gamma^v = \partial\Omega$).	27
Figure 2.3	Body force problem: This figure shows the variation of dissipation and total mechanical power with mesh refinement under the Darcy and Darcy-Brinkman models using quadrilateral and triangular elements for parameters provided in Table 2.1.	28
Figure 2.4	Body force problem: This figure shows the variation of $\varepsilon_{\text{reciprocal}}$ with mesh refinement for the Darcy and Darcy-Brinkman models using quadrilateral and triangular elements for parameters provided in Table 2.1.	29
Figure 2.5	Lid-driven cavity problem: The computational domain is a unit square. Velocity is prescribed on the entire boundary (i.e., $\Gamma^v = \partial\Omega$). The prescribed velocity on the top side is $v_x = 1$ and $v_y = 0$ and on the remaining sides is zero.	30
Figure 2.6	Lid-driven cavity problem: The top figures show a uniform structured mesh, and an adaptive mesh near the top corners. The bottom figures show the variation of total dissipation with mesh refinement.	31

Figure 2.7	Pipe bend problem (velocity boundary condition): A pictorial description of the problem. The computational domain Ω is a unit square. The velocity boundary condition is prescribed on the entire boundary (i.e., $\Gamma^v = \partial\Omega$).	32
Figure 2.8	Pipe bend problem (velocity boundary condition): The figure shows that the dissipation and total mechanical power decrease uniformly with mesh refinement for the Darcy and Darcy-Brinkman models.	32
Figure 2.9	Pipe bend problem (velocity-pressure boundary condition): The computational domain Ω is a square with $L = 1$. The traction boundary condition is $\mathbf{t}^p(\mathbf{x}) = -p_{\text{atm}}\hat{\mathbf{n}}(\mathbf{x})$ on Γ^t .	33
Figure 2.10	Pipe bend problem (velocity-pressure boundary condition): The top figures show the uniform structured mesh and the adaptive mesh near the corners of the outlet. The bottom figures show the variation of the total mechanical power with mesh refinement.	34
Figure 2.11	Pressure pipe bend problem (pressure-pressure boundary condition): The computational domain Ω is a unit square. The traction is prescribed on a part on the left side and on a part on the bottom side.	35
Figure 2.12	Pressure pipe bend problem (pressure-pressure boundary condition): The figure shows the variation of $\varepsilon_{\text{reciprocal}}$ with mesh refinement for the Darcy and Darcy-Brinkman models using quadrilateral and triangular finite elements.	36
Figure 2.13	Pressure slab problem: The computational domain is a $W \times L$ rectangle. The traction is prescribed on the left side of the boundary and on the right side. Elsewhere, homogeneous velocity is enforced.	37

Figure 2.14	Pressure slab problem: The figure shows the variation of $\varepsilon_{\text{reciprocal}}$ with mesh refinement for Darcy and Darcy-Brinkman equations using quadrilateral and triangular grids. The parameters in this problem are provided in Table 2.5.	38
Figure 2.15	Pressure-driven problem: computational domain Ω is a square with $L = 1$. The traction is prescribed on the left side of the boundary and on the middle of right side.	39
Figure 2.16	Pressure-driven problem: The top figures show the uniform structured mesh and the adaptive mesh near the corners of the outlet (i.e., Γ_2^t). The bottom figures show the variation of $\varepsilon_{\text{reciprocal}}$ with mesh refinement.	40
Figure 2.17	The figure verifies the maximum principle for the vorticity for various two-dimensional problems under the Darcy-Brinkman model. The numerical results corroborate the theoretical predictions given in Theorem 2.3.8.	41
Figure 2.18	Synthetic reservoir problem: This figure shows the contours of (smooth) Marmousi dataset [Benamou, 2014]. It provides values on a 384×122 grid which scaled to our rectangular computational domain of $L = 2$ and $H = 1$	42
Figure 2.19	Synthetic reservoir problem: The domain of the problem is a rectangle of size $H \times L$. The injection pressure is prescribed on the left and right boundaries and the atmosphere pressure is prescribed on the middle of top side.	43

Figure 2.20	Synthetic reservoir problem: The figures show the variation of $\varepsilon_{\text{reciprocal}}$ with h for the Darcy and Darcy-Brinkman models using structured and adaptive meshes. The parameters in this problem are provided in Table 2.7.	44
Figure 2.21	Synthetic reservoir problem: The figure shows the magnitude of vorticity for two-dimensional Darcy-Brinkman equations using quadrilateral elements. The parameters used in this problem are provided in Table 2.7.	44
Figure 2.22	Pressure slab problem: The figure verifies the theoretical results for the vorticity under transient Darcy equations. The results show that the slope of $\log(\frac{\omega}{\omega_0})$ for various spatial points in the domain are close to $-\frac{\alpha}{\rho} = -1$	47
Figure 2.23	The figure verifies the maximum principle for the vorticity under transient Darcy-Brinkman equations for various two-dimensional problems. The numerical results satisfy the maximum principle for all the test problems.	48
Figure 3.1	Mixing evolution: Time evolution for the equation (3.4.11) using numerical simulation for different $\mathbb{P}e$, $\mathbb{L}e$, and R_θ . For all we keep $R_c = 2$. For each value of R_θ , the evolution in time for left hand side and right hand side of the equation (3.4.11) is very similar.	63
Figure 3.2	Mixing evolution: Evolution of $\varepsilon_{\mathbf{v}}$ and $\varepsilon_{c\theta}$ in time using numerical simulation for different $\mathbb{P}e$, $\mathbb{L}e$, and R_θ . For all we keep $R_c = 2$. For each value of R_θ , the two variables evolve similarly which completely satisfies the equation (3.4.14).	64

Figure 3.3	Mixing evolution: Time evolution for the equation (3.4.19) using numerical simulation for different $\mathbb{P}e$, $\mathbb{L}e$, and R_θ . For all we keep $R_c = 2$. The scaling expressions $\langle \chi^2 \rangle \sim t^2$ and $-2\varepsilon_{c\theta} + 2\mathbb{P}eR_c^2 \left(\frac{\mathbb{L}e-1}{\mathbb{L}e+1}\right)^2 \varepsilon_c \sim t$ are identified which satisfy the equation (3.4.19). Note that $\lambda = 2\mathbb{P}eR_c^2 \left(\frac{\mathbb{L}e-1}{\mathbb{L}e+1}\right)^2$, in the plot.	66
Figure 3.4	Mixing evolution: These figures show mixing parameters $\langle c^2 \rangle$, ε_c , $\langle \theta^2 \rangle$, and ε_θ vs. time for $\mathbb{P}e = 10^4$, $\mathbb{L}e = 10$ and $R_c = 2$. The scaling expression $\langle c^2 \rangle \sim t^2$ and $\langle \theta^2 \rangle \sim t^2$ are found. Moreover, scaling statement $\varepsilon_c \sim t$ and $\varepsilon_\theta \sim t$ are identified which satisfy equations (3.4.24) and (3.4.25).	67
Figure 3.5	Hele-Shaw cell: Pictorial description of the problem including boundary and initial conditions. The computational domain is a $L_x \times L_y$ rectangle. The disturbed fluid $(\mu_1(c, \theta), c, \theta)$ flows into the domain which contains second flow at rest (μ_2, c^0, θ^0)	69
Figure 3.6	Concentration: These figures show concentration profile for $\mathbb{P}e = 10^4$, $\mathbb{L}e = 10$ and $R_c = 2$. Thermal log-mobility is also (a) $R_\theta = -3$, (b) $R_\theta = 0$, and (c) $R_\theta = 3$. The frame numbers indicate the time. Note that $0 \leq c(\mathbf{x}, t) \leq 1$	72
Figure 3.7	Temperature: These figures show temperature $\theta(\mathbf{x}, t)$ for $\mathbb{P}e = 10^4$, $\mathbb{L}e = 10$, and $R_c = 2$. Thermal log-mobility is also (a) $R_\theta = -3$ and (b) $R_\theta = 3$. The frame numbers indicate the time.	73
Figure 3.8	Viscosity: These figures show viscosity $\mu_1(c, \theta)$ for $\mathbb{P}e = 10^4$, $\mathbb{L}e = 10$, and $R_c = 2$. Thermal log-mobility is also (a) $R_\theta = 0$ and (b) $R_\theta = 3$. The frame numbers indicate the time.	74

Figure 3.9	Concentration: These figures show concentration $c(\mathbf{x}, t)$ for $\mathbb{P}e = 10^4$, $R_c = 2$, and $R_\theta = 2$. Lewis number is also (a) $\mathbb{L}e = 10$ and (b) $\mathbb{L}e = 4$. The frame numbers indicate the time.	74
Figure 3.10	Temperature and viscosity: These figures show temperature θ and viscosity μ for $\mathbb{P}e = 10^4$, $R_c = 2$, and $R_\theta = 2$. Lewis number is also (a) $\mathbb{L}e = 10$ and (b) $\mathbb{L}e = 4$. Upper figures depict temperature and lower viscosity profiles.	75
Figure 3.11	Concentration: These figures show concentration $c(\mathbf{x}, t)$ for $\mathbb{P}e = 2 \times 10^3$, $\mathbb{L}e = 10$, and $R_c = 2$. Thermal log-mobility is also (a) $R_\theta = -3$, (b) $R_\theta = 0$, and (c) $R_\theta = 3$. The frame numbers indicate time.	75
Figure 3.12	Viscosity: These figures show viscosity $\mu_1(c, \theta)$ for $\mathbb{P}e = 2 \times 10^3$, $\mathbb{L}e = 10$, and $R_c = 2$. Thermal log-mobility is also (a) $R_\theta = 0$ and (b) $R_\theta = 3$. The frame numbers indicate time.	76
Figure 3.13	Concentration: These figures show concentration $c(\mathbf{x}, t)$ for $R_c = 2$ and $R_\theta = 2$. The frame numbers indicate time. Mechanisms for high log-mobility introduced in [Islam and Azaiez, 2005] such as skewering and alternating side branching are observed.	77
Figure 3.14	Mixing time: These figures show average transverse concentration $\bar{C}(t)$ vs. time $R_c = 2$ at $L_x/2$. Mixing time is shorter for smaller values of $ R_c - R_\theta $ and <i>minimum</i> mixing time occurs for $R_\theta = 2$. For $R_\theta = -3$, it is observed that the tip splitting and finger channeling increase mixing time.	79

Figure 3.15	Mixing length: These figures show average transverse concentration $\bar{c}(x)$ vs. x for $R_c = 2$. Mixing length is shorter for smaller values of $ R_c - R_\theta $ and <i>minimum</i> mixing length occurs again for $R_\theta = 2$. For $R_\theta = -3$, it is observed that the tip splitting and finger channeling increase mixing length.	80
Figure 3.16	Quarter five-square: Pictorial description of the problem including initial and boundary conditions. The computational domain includes a unit square and two small squares with length W as injection and production wells.	81
Figure 3.17	Violation of maximum principle: The upper figures are concentrations for SUPG formulation (eq. (3.3.5)). the middle figures are for modified SUPG in which we added isotropic artificial diffusion (eq. (3.3.7)) and bottom figures are for modified SUPG with crosswind artificial diffusion (eq. (3.3.8)).	82
Figure 3.18	Physical instability diminishing: These figures show concentration at different time steps for quarter five-square with modified SUPG stabilized formulation in which we added both isotropic and crosswind artificial diffusion.	83
Figure 4.1	Double permeability: Pictorial description of the problem for stability analysis in which the domain is unbounded. The displacing fluid ($\mu_1(c)$ and c_1) flows into the domain which contains displacing fluid (μ_2, c_2).	103
Figure 4.2	Effect of K_2 : The figures show the effect of K_2 on dispersion curve for $\beta = 0.001$ and 0.01 , $K_1 = k_1 = k_2 = 1$, and $R = 3, 4$, and 5	104
Figure 4.3	Effect of β : The plots show the effect of β on dispersion curve for $K_1 = k_1 = k_2 = 1$, $R = 2, 3$, and 4 , and $K_2 = 0.1$ and 10	105

Figure 4.4	Effect of R : The figures show the effect of R on dispersion curve for $\beta = 0.1$ and 0.01 , $K_1 = k_1 = k_2 = 1$, and different K_2	106
Figure 4.5	Hele-Shaw cell - double permeability: Pictorial description of the problem including boundary and initial conditions. The computational domain is a $L_x \times L_y$ rectangle. The disturbed fluid ($\mu_1(c)$ and c) flows into the domain which contains second flow at rest (μ_2, c^0).	108
Figure 4.6	Effect of K_2 : The figures show the effect of K_2 on concentration profiles for $\beta = 0.001$, $K_1 = k_1 = k_2 = 1$, and $R = 1.5$. Increasing the values of K_2 destabilize the system.	109
Figure 4.7	Effect of β : The figures show the effect of β on concentration profiles for $R = 4$, $K_1 = k_1 = k_2 = 1$, and $K_2 = 10$. Increasing the values of β also destabilize the system.	110
Figure 4.8	Effect of R : The figures show the effect of R on concentration profiles for $\beta = 0.001$, $K_1 = k_1 = k_2 = 1$, and $K_2 = 2$. In this case also, by increasing the values of R the system becomes less stable.	110

List of Tables

Table 2.1	Body force problem: Non-dimensional parameters used in the problem.	27
Table 2.2	Lid-driven cavity problem: Non-dimensional parameters used in the problem.	28
Table 2.3	Pipe bend problem: Non-dimensional parameters of the parabolic velocity boundary condition problem.	32
Table 2.4	Pipe bend problem: Non-dimensional parameters of the zero velocity (wall)-pressure boundary conditions.	33
Table 2.5	Pressure slab problem: Non-dimensional parameters used in the problem.	37
Table 2.6	Pressure driven problem: Non-dimensional parameters used in the problem.	38
Table 2.7	Synthetic reservoir problem: Non-dimensional parameters used in the problem.	42
Table 2.8	Pressure slab problem: Initial condition used in the problem.	46
Table 3.1	Hele-Shaw cell: Parameters used in the problem.	71
Table 3.2	Quarter five-square: Parameters used in the problem.	81

Chapter 1

INTRODUCTION AND MOTIVATION

The true sign of intelligence is not knowledge but imagination.

Albert Einstein

Porous media models are widely employed to make predictions in many subsurface problems which typically involves complex geometries, coupled processes, and heterogeneous material properties. For a problem with no known analytical or reference solution (which is generally the case in realistic porous media problems), it therefore is necessary to rely on numerical simulations to solve problems and to make critical decisions. Moreover, it is a major task for scientists to ensure that the employed numerical formulations and obtained solutions are sufficiently accurate. On the other hand, due to advancements in digital imaging in porous media, high-resolution numerical methods, and high performance computing methods, the accuracy and verification of numerical results are still highly challenging.

To answer the questions about solution verification of porous media models, herein, we address several mathematical properties include the total minimum mechanical power, minimum dissipation theorem, reciprocal relation, and maximum principle for the vorticity. All the developed theorems have firm mechanical bases

and are independent of numerical methods. So, these can be utilized for solution verification of finite element, finite volume, finite difference, lattice Boltzmann methods and so forth. Using several numerical examples, we will demonstrate the predictive capabilities of the proposed *a posteriori* techniques to assess the accuracy of numerical solutions for a general class of problems, which could involve complex domains and general computational grids.

In coupled, multi-process porous media problems, there is also observed a physical instability so-called miscible displacement and viscous fingering. This phenomena is found at the interface of two miscible flows with different viscosities while each flow conveys a different transport. It should be noted that the viscosity of a fluid can be influenced by altering physical properties and parameters like thermal and transport mobility ratios, chemical reaction, Péclet number, and Lewis number. A number of experimental, theoretical and numerical works have been done to understand various aspects of the viscous fingering instability [Bacri et al., 1992, de Bruyn, 1995, Petitjeans and Maxworthy, 1996, Wit et al., 2005, Islam and Azaiez, 2007, Maes et al., 2010, Nagatsu and Wit, 2011, Nicolaidis et al., 2015]. The simplified model to capture viscous fingering numerically, is a coupled Darcy flow and advection-dominated advection-diffusion (AD) equations. If the chemical reaction affects the viscosity, then solution of advection-diffusion-reaction (ADR) model is necessary. It is, in general, not possible to obtain analytical solutions under this system of partial differential equations (PDEs) and one commonly seeks numerical solutions for the problem. Herein, the influence of temperature on viscous fingering, which is interpreted as double diffusive effects, is studied. To consider temperature effects, the model shall include thermal equations by adding the balance of energy. Some of the studies which take into account the impact of temperature in their experimental, theoretical and numerical works are [Pritchard, 2004, Nagatsu et al., 2009, Islam and Azaiez, 2010b, Mishra et al., 2010]. We also characterize mixing for double diffusive viscous fingering

by proposing a reduced order model (ROM) and constructing two scaling expressions. The mixing in viscous fingering is studied before by [Jha et al., 2011]. Herein, we show drawbacks of previous hypothesis and its assumptions. Employing finite element formulation to numerically solve strongly nonlinear coupled porous media flow, transport, and thermal problem, motivate us to study the effects of numerical stabilization on viscous fingering. By investigating the impact of violation of non-negative constraint on the development of viscous fingering instabilities, we show that the popular numerical stabilized formulations including Streamline Upwind Petrov-Galerkin (SUPG) and its modification, Spurious Oscillation at Layers Diminishing (SOLD), can not eliminate the violation of the non-negative constraint for the concentration. Moreover, these stabilized formulations may also suppress the physical viscous fingering instabilities, which raise the question of their utility for simulating physical instabilities.

The linear stability analysis and numerical simulations of coupled flow and transport in porous media with double permeability is also conducted in current study. The motivation to analyze stability of viscous fingering phenomena in double permeability model is to understand the effect of micro and macro-network in coupled porous media flow and advective-diffusive transport which is more realistic model than the single permeability assumption. We show that the parameters like permeability of micro and macro-structure and mass transfer between micro and macro-network have significant effect on the dynamics of fingers. To performed a linear stability analysis we utilize a quasi-steady state method, in which the base state change is slow compared to the perturbation growth rate. A generalized Fourier series expansion is used for the perturbed equations to validate the results of the quasi-steady state method. It have been found that the both solutions are in good agreement at small time [Pranmanik and Mishra, 2013]. Linear stability analysis for the growth rate of instabilities

in single permeability problems for anisotropic, heterogeneous, and chemical reactive cases have been performed before (see [Tan and Homsy, 1986, Zimmerman and Homsy, 1991, Norouzi and Shoghi, 2014, Hejazi et al., 2010] and references therein). The linear stability of double diffusive viscous fingering have been also studied in some researches including [Pritchard, 2004, 2009, Islam and Azaiez, 2010a]. To the best of our knowledge, there is not a prior work for the stability analysis and numerical solutions of double permeability/porosity models. In this dissertation, we use the mathematical framework recently developed by [Nakshatrala et al., 2016a] and perform the analysis. Then, we provide the numerical solutions of coupled anisotropic double permeability porous media flow and advection-diffusion models by employing finite element formulation.

The rest of the dissertation is organized as follows. Chapter 2 presents the mechanics-based solution verification for porous media models. In Chapter 3, we study effect of double diffusion and impact of finite element stabilized formulations on viscous fingering and mixing in porous media. Chapter 4 provides linear stability analysis and numerical solutions for viscous fingering in porous media with double permeability. Conclusions of this dissertation are drawn in Chapter 5.

Chapter 2

MECHANICS-BASED SOLUTION VERIFICATION FOR POROUS MEDIA MODELS

Errors are not in the art but in the artificers.

Isaac Newton

2.1 Introduction

The simplest and yet the most popular model that subsurface modelers use is the Darcy model [Darcy, 1856], which describes the flow of an incompressible fluid in a rigid porous media. The Darcy model has been employed in several branches of engineering and in several important technological applications. Some specific examples include groundwater hydrology [Raats, 1984, Munaf et al., 1993], enhanced oil recovery [Minkoff et al., 2003], and simulation of flow of resin in composite manufacturing [Turner et al., 2006, Lee et al., 2009]. The Darcy model has also been a cornerstone for the theoretical development of mixture theories [Bowen, 1976, de Boer, 2000]. However, the Darcy equations posed several challenges to the finite element community but played a crucial role in the development of mixed and stabilized formulations [Brezzi and Fortin, 1991, Masud and Hughes, 2002, Nakshatrala et al.,

2006]. These equations have received considerable attention even from the mathematical community, especially in the area of mathematical homogenization [Hornung, 1996]. Brinkman [Brinkman, 1947a,b] proposed a popular extension to the Darcy model which is commonly referred to as the Darcy-Brinkman model. In addition to drag between the fluid and porous solid, Darcy-Brinkman model accounts for friction between fluid layers.

The Darcy and Darcy-Brinkman models are adequate for most of the civil engineering and geotechnical applications in which the velocities and its gradient are small. It is, however, not possible to obtain analytical solutions under these models, and one commonly seeks numerical solutions for realistic problems. Some notable numerical formulations for Darcy and Darcy-Brinkman equations are [Chavent et al., 1984, Ewing and Heinemann, 1984, Durlofsky, 1994, Arbogast et al., 1997, Masud and Hughes, 2002, Brezzi et al., 2005a, Nakshatrala et al., 2006, Burman and Hansbo, 2007, Nakshatrala and Rajagopal, 2011, Srinivasan and Nakshatrala, 2012]. Below are some specific challenges that a computational scientist may face in using numerical simulators:

1. How much mesh refinement is required to obtain solutions with desired degree of accuracy for a problem that does not have an analytical or reference solution?
2. Will the chosen mesh be able to resolve singularities in the solution and avoid pollution errors? That is, can we identify whether a particular type of mesh suffers from pollution errors for a problem with singularities?
3. Has the computer implementation been done properly?
4. Is the chosen numerical formulation accurate/appropriate for the chosen problem?

In the literature, one finds the usual approach of employing tools from functional

analysis to obtain *a priori* estimates and assess stability. For example, see [Brezzi and Fortin, 1991, Babuška and Strouboulis, 2001].

This study aims to address the aforementioned challenges for popular porous media models by providing various *a posteriori* techniques with firm mechanics underpinning. It needs to be emphasized that the techniques presented in this paper will not be able to *completely* address all the aforementioned challenges. For example, there is currently no methodology that can judge with certainty the correctness of a computer implementation. The proposed techniques are no exception. However, the proposed *a posteriori* techniques can be judiciously utilized to increase the confidence or detect shortcomings of a computer implementation and to assess the accuracy of numerical solutions.

2.1.1 Validation and Verification (V&V)

Errors can arise in both physical modeling and numerical simulation. The study of errors due to physical modeling is referred to as validation, and the study of error in a numerical simulation is referred to as verification. As Blottner [Blottner, 1990] nicely puts it, validation is to solve “*right governing equations*” and verification is to solve “*governing equation right*”.

Validation errors arise when a model is used out of its application range. Boundary conditions are also an important source of validation errors. The validation is beyond the scope of this study, and the reader can consult [Roache, 1998] and the references therein. The errors in the verification can arise from three broad sources including numerical errors, round-off errors (due to the finite precision arithmetic), and programming mistakes [Oberkampf et al., 2004]. Basically, the verification is to ensure that the code produces a solution to the model with some degree of accuracy, and the numerical solution is consistent. Verification itself can be divided into two categories: verification of code and verification of calculation [Roache, 1998].

2.1.1.1 Verification of code

Verification of code addresses the question of whether the numerical algorithms have been programmed and implemented correctly in the code. The two currently popular approaches to verify a code are the *method of exact solutions* (MES) and the *method of manufactured solutions* (MMS). In the MES, one first seeks exact solutions often with simplifications to the equations and/or the boundary conditions. The numerical results with corresponding inputs are then compared to the exact solutions. In the MMS, an analytical solution is manufactured *a priori* and a source term is then calculated that satisfies the governing equations. Steinberg and Roache [Steinberg and Roache, 1985] advocate the combined use of the MMS and grid convergence for the verification of code. If the code passes a desired number of test problems constructed by MES and/or MMS, then the code is certified to be verified adequately. This by no means implies that the code is completely bug free. More thorough discussions on MES and MMS can be found in [Knupp and Salari, 2003, Roy et al., 2004, Roache, 1998].

2.1.1.2 Verification of calculation

Verification of calculation (which is also referred to as solution verification) estimates the overall magnitude (not just the order) of the numerical errors in a calculation, and the procedure invariably involves *a posteriori* error estimation [Salari and Knupp, 2000]. The numerical errors in the solution verification can arise from two different sources including discretization errors and solution errors. The discretization errors refer to all the errors caused by conversion of the governing equations (PDEs and boundary conditions) into discrete algebraic equations whereas the solution errors refer to the errors in approximate solution of the discrete equations. The numerical errors may arise from insufficient mesh resolution, improper selection of time-step, and incomplete iterative convergence. For more details on verification of calculation,

see [Roy et al., 2004, Salari and Knupp, 2000, Roache, 1997, 1998, Babuška and Oden, 2004, Oberkampf and Blottner, 1998, Oberkampf et al., 2004].

2.1.2 *A posteriori* techniques

The aim of *a posteriori* error estimation is to assess the accuracy of the numerical approximation in the terms of *known* quantities such as geometrical properties of computational grid, the input data, and the numerical solution. *A posteriori* error techniques monitor various forms of the error in the numerical solution such as velocity, stress, mean fluxes, and drag and lift coefficients [Becker and Rannacher, 2001]. Such error estimation differ from *a priori* error estimates in that the error controlling parameters depend on *unknown* quantities. *A priori* error estimation investigates the stability and convergence of a solver and can give rough information on the asymptotic behavior of errors in calculations when grid parameters are changed appropriately [Ainsworth and Oden, 1997].

In the current study, we propose new mechanics-based criteria that can be used to verify the accuracy and convergence of numerical solutions to Darcy and Darcy Brinkman equations. The solution verification requires confirmation of grid convergence which is one of the most common and reliable error estimation methods [Roache, 1997]. Similar to other grid convergence studies, we address only solution verification. Since the aim of this paper is *a posteriori* error estimation, we assume that the code has already been verified for the Darcy and Darcy-Brinkman class of problems so that programming mistakes are not an issue. Likewise, we are not also concerned with validation. It means that the Darcy and Darcy-Brinkman models are physically adequate to model the problems.

2.1.3 An outline of the chapter

Section 2.2 presents the governing equations arising from the Darcy and Darcy-Brinkman models. In Section 2.3, we propose various mathematical properties that the solutions to these governing equations satisfy. We also discuss how these properties can be utilized as robust *a posteriori* criteria to assess the accuracy of numerical solutions. Section 2.4 presents several steady-state numerical results to illustrate the predictive capabilities of the proposed *a posteriori* criteria with respect to singularities, pollution errors, and discretization errors in the implementation of (Neumann) boundary conditions. We also utilize synthetic reservoir data to demonstrate the usefulness of the proposed *a posteriori* techniques, especially for problems involving spatially heterogeneous permeability properties. Section 2.5 discusses *a posteriori* criteria for transient problems, and presents representative numerical results in support of the theoretical predictions. Finally, conclusions are drawn in Section 2.6.

2.2 Darcy and Darcy-Brinkman models

Let $\Omega \subset \mathbb{R}^{nd}$ be an open and bounded domain, where “ nd ” denotes the number of spatial dimensions. We shall denote the set closure of Ω by $\bar{\Omega}$. Let $\partial\Omega := \bar{\Omega} - \Omega$ denote the boundary, which is assumed to be piecewise smooth. A spatial point in $\bar{\Omega}$ is denoted by \mathbf{x} . The spatial gradient and divergence operators are, respectively, denoted as $\text{grad}[\cdot]$ and $\text{div}[\cdot]$. Let $\mathbf{v} : \Omega \rightarrow \mathbb{R}^{nd}$ denote the velocity field and $p : \Omega \rightarrow \mathbb{R}$ denote the pressure field. The symmetric part of the gradient of velocity is denoted by $\mathbf{D}(\mathbf{x}) = \frac{1}{2} (\text{grad}[\mathbf{v}] + \text{grad}[\mathbf{v}]^T)$. The unit outward normal to the boundary is denoted as $\hat{\mathbf{n}}(\mathbf{x})$. The boundary is divided into two parts: Γ^v and Γ^t . Γ^v is the part of the boundary on which the velocity is prescribed, and Γ^t is that part of the boundary on which the traction is prescribed. For mathematical well-posedness, we have $\Gamma^v \cap \Gamma^t = \emptyset$ and $\Gamma^v \cup \Gamma^t = \partial\Omega$.

The porous media models that will be considered in this paper are the Darcy and Darcy-Brinkman models. Both these models describe the flow of an incompressible fluid through *rigid* porous media. We completely neglect the motion of the porous solid. The Cauchy stress in the Darcy and Darcy-Brinkman models, respectively, take the following form:

$$\mathbf{T}(\mathbf{x}) = -p(\mathbf{x})\mathbf{I} \quad \text{and} \quad (2.2.1a)$$

$$\mathbf{T}(\mathbf{x}) = -p(\mathbf{x})\mathbf{I} + 2\mu\mathbf{D}(\mathbf{x}), \quad (2.2.1b)$$

where \mathbf{I} denotes the second-order identity tensor, and μ is the dynamic coefficient of viscosity. The steady-state governing equations based on the Darcy model can be written as follows:

$$\alpha(\mathbf{x})\mathbf{v}(\mathbf{x}) + \text{grad}[p(\mathbf{x})] = \rho\mathbf{b}(\mathbf{x}) \quad \text{in } \Omega, \quad (2.2.2a)$$

$$\text{div}[\mathbf{v}(\mathbf{x})] = 0 \quad \text{in } \Omega, \quad (2.2.2b)$$

$$\mathbf{v}(\mathbf{x}) \cdot \hat{\mathbf{n}}(\mathbf{x}) = v_n(\mathbf{x}) \quad \text{on } \Gamma^v, \quad \text{and} \quad (2.2.2c)$$

$$p(\mathbf{x}) = p_0(\mathbf{x}) \quad \text{on } \Gamma^t, \quad (2.2.2d)$$

where $\alpha(\mathbf{x})$ is the drag coefficient, ρ is the density of the fluid, $\mathbf{b}(\mathbf{x})$ is the specific body force, $v_n(\mathbf{x})$ is the prescribed normal component of the velocity, and $p_0(\mathbf{x})$ is the prescribed pressure. The steady-state governing equations based on the Darcy-Brinkman model take the following form:

$$\alpha(\mathbf{x})\mathbf{v}(\mathbf{x}) + \text{grad}[p(\mathbf{x})] - \text{div}[2\mu\mathbf{D}] = \rho\mathbf{b}(\mathbf{x}) \quad \text{in } \Omega, \quad (2.2.3a)$$

$$\text{div}[\mathbf{v}(\mathbf{x})] = 0 \quad \text{in } \Omega, \quad (2.2.3b)$$

$$\mathbf{v}(\mathbf{x}) = \mathbf{v}^p(\mathbf{x}) \quad \text{on } \Gamma^v, \quad \text{and} \quad (2.2.3c)$$

$$\mathbf{T}\hat{\mathbf{n}}(\mathbf{x}) = \mathbf{t}^p(\mathbf{x}) \quad \text{on } \Gamma^t, \quad (2.2.3d)$$

where $\mathbf{v}^p(\mathbf{x})$ is the prescribed velocity vector, and $\mathbf{t}^p(\mathbf{x})$ is the prescribed traction. We shall call a vector-field to be *Darcy velocity* if satisfies equations (2.2.2a)–(2.2.2d). We shall call a vector field to be *Darcy-Brinkman velocity* if it satisfies equations (2.2.3a)–(2.2.3d).

Equations (2.2.2a) and (2.2.3a) can be obtained from the balance of linear momentum under the mathematical framework offered by the theory of interacting continua [Nakshatrala and Rajagopal, 2011]. The drag term $\alpha(\mathbf{x})\mathbf{v}(\mathbf{x})$ models the frictional force between the fluid and the porous solid. The term $\text{div}[2\mu\mathbf{D}]$ in the Darcy-Brinkman model arises due to the internal friction between the layers of the fluid. The pressure $p(\mathbf{x})$ is an undetermined multiplier that arises due to the enforcement of the incompressibility constraint given by equations (2.2.2b) and (2.2.3b). The drag coefficient is related to the coefficient of viscosity of the fluid and the permeability $k(\mathbf{x})$ as

$$\alpha(\mathbf{x}) = \frac{\mu}{k(\mathbf{x})}. \quad (2.2.4)$$

In general, it is not possible to obtain analytical solutions to the systems of equations given by either (2.2.2a)–(2.2.2d) or (2.2.3a)–(2.2.3d). Hence, one needs to resort to numerical solutions. *This paper does not concern with developing new numerical formulations to solve the aforementioned mathematical models. The paper instead focuses on deriving mathematical properties with firm mechanics underpinning that the solutions to these mathematical models satisfy. We shall then illustrate how these mathematical properties can serve as robust “a posteriori” criteria to assess the accuracy of numerical solutions.*

2.3 Mathematical properties: Statements and derivations

In the remainder of this paper, we shall refer to a vector field $\tilde{\mathbf{v}} : \Omega \rightarrow \mathbb{R}^{nd}$ as *kinematically admissible* if it satisfies the following conditions:

- (i) $\tilde{\mathbf{v}}(\mathbf{x})$ is solenoidal (i.e., $\text{div}[\tilde{\mathbf{v}}(\mathbf{x})] = 0$ in Ω), and
- (ii) $\tilde{\mathbf{v}}(\mathbf{x})$ satisfies the boundary conditions.

It needs to be emphasized that a kinematically admissible vector field need not satisfy the balance of linear momentum given by equation (2.2.2a) or (2.2.3a). Clearly, the Darcy velocity and the Darcy-Brinkman velocity are kinematically admissible vector fields. For some of the results presented in this paper, we will need the body force to be conservative, which is a common terminology in potential theory [Kellogg, 2010]. The body force $\rho\mathbf{b}(\mathbf{x})$ is said to be conservative if there exists a scalar potential $\psi(\mathbf{x})$ such that $\rho\mathbf{b}(\mathbf{x}) = -\text{grad}[\psi]$. We shall define the dissipation functional as

$$\Phi[\mathbf{v}] := \begin{cases} \int_{\Omega} \alpha(\mathbf{x}) \mathbf{v}(\mathbf{x}) \cdot \mathbf{v}(\mathbf{x}) \, d\Omega & \text{Darcy model} \\ \int_{\Omega} \alpha(\mathbf{x}) \mathbf{v}(\mathbf{x}) \cdot \mathbf{v}(\mathbf{x}) \, d\Omega + \int_{\Omega} 2\mu \mathbf{D}(\mathbf{x}) \cdot \mathbf{D}(\mathbf{x}) \, d\Omega & \text{Darcy-Brinkman model.} \end{cases} \quad (2.3.1)$$

Since $\alpha > 0$ and $\mu > 0$, it is straightforward to check that $\Phi[\mathbf{v}]$ is a norm. In fact, it can be shown that $\Phi[\mathbf{v}]$ under the Darcy model is *equivalent* to the natural norm in $(L^2(\Omega))^{nd}$, where $(L^2(\Omega))^{nd}$ is a space of square integrable vector fields defined from Ω to \mathbb{R}^{nd} . Similarly, it can be shown that $\Phi[\mathbf{v}]$ under the Darcy-Brinkman model is equivalent to the natural norm in $(H^1(\Omega))^{nd}$, which is a Sobolev space. For further details on function spaces and norms, refer to [Evans, 1998].

In this section, we shall present four important mathematical properties that the solutions to Darcy equations and Darcy-Brinkman equations satisfy. These properties

will be referred to as (i) the minimum total mechanical power theorem, (ii) the minimum dissipation theorem, (iii) reciprocal relation, and (iv) maximum principle for vorticity. As a passing comment, we will employ the minimum dissipation theorem to show the uniqueness of solution for Darcy equations and Darcy-Brinkman equations. In the porous media literature, these results have neither been discussed nor utilized to solve problems. More importantly, these results have not been used to assess the accuracy and convergence of numerical solutions of porous media models. For example, it will be shown that the minimum total mechanical power theorem can be utilized to assess the accuracy of the implementation of both Dirichlet and Neumann boundary conditions. On the other hand, the minimum dissipation theorem can be utilized to identify pollution errors in the numerical solution. Herein, we give detailed mathematical proofs for Darcy-Brinkman equations. We however provide comments on the corresponding proofs for Darcy equations.

Theorem 2.3.1 (Minimum total mechanical power theorem). *Let $\mathbf{v}(\mathbf{x})$ be the Darcy-Brinkman velocity vector field. Then, any kinematically admissible vector field $\tilde{\mathbf{v}}(\mathbf{x})$ satisfies the following inequality:*

$$\varepsilon_{\text{TMP}}[\mathbf{v}] \leq \varepsilon_{\text{TMP}}[\tilde{\mathbf{v}}], \quad (2.3.2)$$

where

$$\varepsilon_{\text{TMP}}[\mathbf{z}] := \frac{1}{2}\Phi[\mathbf{z}] - \int_{\Omega} \rho \mathbf{b}(\mathbf{x}) \cdot \mathbf{z}(\mathbf{x}) \, d\Omega - \int_{\Gamma^t} \mathbf{t}^p(\mathbf{x}) \cdot \mathbf{z}(\mathbf{x}) \, d\Gamma. \quad (2.3.3)$$

That is, for given boundary conditions, body force and tractions; the Darcy-Brinkman velocity will have the minimum total mechanical power among all the possible kinematically admissible vector fields.

Proof. Let

$$\delta\mathbf{v}(\mathbf{x}) := \tilde{\mathbf{v}}(\mathbf{x}) - \mathbf{v}(\mathbf{x}) \quad \text{and} \quad (2.3.4a)$$

$$\delta\mathbf{D}(\mathbf{x}) := \tilde{\mathbf{D}}(\mathbf{x}) - \mathbf{D}(\mathbf{x}). \quad (2.3.4b)$$

From the hypothesis of the theorem, $\delta\mathbf{v}(\mathbf{x})$ satisfies the following relations:

$$\delta\mathbf{v}(\mathbf{x}) = \mathbf{0} \quad \forall \mathbf{x} \in \partial\Omega \quad \text{and} \quad (2.3.5a)$$

$$\operatorname{div}[\delta\mathbf{v}] = 0 \quad \forall \mathbf{x} \in \Omega. \quad (2.3.5b)$$

Let us start with the dissipation due to the vector field $\tilde{\mathbf{v}}(\mathbf{x})$:

$$\begin{aligned} \Phi[\tilde{\mathbf{v}}(\mathbf{x})] &:= \int_{\Omega} \alpha(\mathbf{x}) \tilde{\mathbf{v}}(\mathbf{x}) \cdot \tilde{\mathbf{v}}(\mathbf{x}) \, d\Omega + \int_{\Omega} 2\mu \tilde{\mathbf{D}}(\mathbf{x}) \cdot \tilde{\mathbf{D}}(\mathbf{x}) \, d\Omega \\ &= \int_{\Omega} \alpha(\mathbf{x}) (\delta\mathbf{v}(\mathbf{x}) + \mathbf{v}(\mathbf{x})) \cdot (\delta\mathbf{v}(\mathbf{x}) + \mathbf{v}(\mathbf{x})) \, d\Omega \\ &\quad + \int_{\Omega} 2\mu (\delta\mathbf{D}(\mathbf{x}) + \mathbf{D}(\mathbf{x})) \cdot (\delta\mathbf{D}(\mathbf{x}) + \mathbf{D}(\mathbf{x})) \, d\Omega \\ &\geq 2 \int_{\Omega} \alpha(\mathbf{x}) \delta\mathbf{v}(\mathbf{x}) \cdot \mathbf{v}(\mathbf{x}) \, d\Omega + 2 \int_{\Omega} 2\mu \delta\mathbf{D}(\mathbf{x}) \cdot \mathbf{D}(\mathbf{x}) \, d\Omega + \Phi[\mathbf{v}(\mathbf{x})]. \end{aligned} \quad (2.3.6)$$

Using equations (2.2.3a) and (2.2.1b) the first integral in the above equation can be written as

$$\int_{\Omega} \alpha(\mathbf{x}) \delta\mathbf{v}(\mathbf{x}) \cdot \mathbf{v}(\mathbf{x}) \, d\Omega = \int_{\Omega} \delta\mathbf{v}(\mathbf{x}) \cdot (\rho\mathbf{b}(\mathbf{x}) + \operatorname{div}[\mathbf{T}(\mathbf{x})]) \, d\Omega. \quad (2.3.7)$$

The symmetry of $\mathbf{D}(\mathbf{x})$ allows the second integral to be written as

$$\begin{aligned} \int_{\Omega} 2\mu \delta\mathbf{D}(\mathbf{x}) \cdot \mathbf{D}(\mathbf{x}) \, d\Omega &= \int_{\Omega} 2\mu \operatorname{grad}[\delta\mathbf{v}(\mathbf{x})] \cdot \mathbf{D}(\mathbf{x}) \, d\Omega \\ &= \int_{\Omega} \operatorname{grad}[\delta\mathbf{v}(\mathbf{x})] \cdot (\mathbf{T}(\mathbf{x}) + p(\mathbf{x})\mathbf{I}) \, d\Omega \\ &= \int_{\Omega} \operatorname{grad}[\delta\mathbf{v}(\mathbf{x})] \cdot \mathbf{T}(\mathbf{x}) \, d\Omega + \int_{\Omega} \operatorname{div}[\delta\mathbf{v}(\mathbf{x})] \cdot p(\mathbf{x}) \, d\Omega. \end{aligned}$$

Noting that $\operatorname{div}[\delta\mathbf{v}] = 0$ in Ω and by employing Green's identity, we have

$$\begin{aligned} \int_{\Omega} 2\mu\delta\mathbf{D}(\mathbf{x}) \cdot \mathbf{D}(\mathbf{x}) \, d\Omega &= \int_{\Omega} \operatorname{div}[\mathbf{T}^T(\mathbf{x}) \delta\mathbf{v}(\mathbf{x})] \, d\Omega - \int_{\Omega} \delta\mathbf{v}(\mathbf{x}) \cdot \operatorname{div}[\mathbf{T}(\mathbf{x})] \, d\Omega \\ &= \int_{\Gamma^t} \delta\mathbf{v}(\mathbf{x}) \cdot \mathbf{t}^P(\mathbf{x}) \, d\Gamma - \int_{\Omega} \delta\mathbf{v}(\mathbf{x}) \cdot \operatorname{div}[\mathbf{T}(\mathbf{x})] \, d\Omega. \end{aligned} \quad (2.3.8)$$

From equations (2.3.7) and (2.3.8), inequality (2.3.6) can be written as

$$\Phi[\tilde{\mathbf{v}}(\mathbf{x})] \geq \Phi[\mathbf{v}(\mathbf{x})] + 2 \int_{\Omega} \delta\mathbf{v}(\mathbf{x}) \cdot \rho\mathbf{b}(\mathbf{x}) \, d\Omega + 2 \int_{\Gamma^t} \delta\mathbf{v}(\mathbf{x}) \cdot \mathbf{t}^P(\mathbf{x}) \, d\Gamma. \quad (2.3.9)$$

This completes the proof. \square

Remark 2.3.2. *For Darcy equations (2.2.2a)–(2.2.2d), one can state the minimum total mechanical power theorem as follows: For given boundary conditions, and body force; the Darcy velocity, $\mathbf{v}(\mathbf{x})$, has the minimum total mechanical power among all the kinematically admissible vector fields as*

$$\begin{aligned} \frac{1}{2}\Phi[\mathbf{v}] - \int_{\Omega} \mathbf{v}(\mathbf{x}) \cdot \rho\mathbf{b}(\mathbf{x}) \, d\Omega + \int_{\Gamma^t} p_0(\mathbf{x})\mathbf{v}(\mathbf{x}) \cdot \hat{\mathbf{n}}(\mathbf{x}) \, d\Gamma &\leq \frac{1}{2}\Phi[\tilde{\mathbf{v}}] \\ - \int_{\Omega} \tilde{\mathbf{v}}(\mathbf{x}) \cdot \rho\mathbf{b}(\mathbf{x}) \, d\Omega + \int_{\Gamma^t} p_0(\mathbf{x})\tilde{\mathbf{v}}(\mathbf{x}) \cdot \hat{\mathbf{n}}(\mathbf{x}) \, d\Gamma &\quad \forall \tilde{\mathbf{v}}(\mathbf{x}). \end{aligned} \quad (2.3.10)$$

Theorem 2.3.3 (Minimum dissipation inequality). *Let $\mathbf{v}(\mathbf{x})$ be the Darcy-Brinkman velocity vector field, and let $\Gamma^v = \partial\Omega$. Then, any kinematically admissible vector field $\tilde{\mathbf{v}}(\mathbf{x})$ satisfies the following inequality:*

$$\Phi[\mathbf{v}] \leq \Phi[\tilde{\mathbf{v}}]. \quad (2.3.11)$$

That is, for given velocity boundary conditions and conservative body force, the Darcy-Brinkman velocity has the minimum total dissipation due to drag and internal friction of all the possible kinematically admissible vector fields.

Proof. We shall employ the notation introduced in equation (2.3.4). Recall that the

mechanical dissipation under the Darcy-Brinkman model is

$$\Phi[\mathbf{v}] = \int_{\Omega} \alpha \delta \mathbf{v}(\mathbf{x}) \cdot \mathbf{v}(\mathbf{x}) \, d\Omega + \int_{\Omega} 2\mu \delta \mathbf{D}(\mathbf{x}) \cdot \mathbf{D}(\mathbf{x}) \, d\Omega. \quad (2.3.12)$$

Let us start with the difference in total dissipation, and from inequality (2.3.6) we have:

$$\Phi[\tilde{\mathbf{v}}(\mathbf{x})] - \Phi[\mathbf{v}(\mathbf{x})] \geq 2 \int_{\Omega} \alpha \delta \mathbf{v}(\mathbf{x}) \cdot \mathbf{v}(\mathbf{x}) \, d\Omega + 2 \int_{\Omega} 2\mu \delta \mathbf{D}(\mathbf{x}) \cdot \mathbf{D}(\mathbf{x}) \, d\Omega. \quad (2.3.13)$$

Using Green's identity, the first integral can be simplified as

$$\begin{aligned} \int_{\Omega} \alpha \delta \mathbf{v}(\mathbf{x}) \cdot \mathbf{v}(\mathbf{x}) \, d\Omega &= \int_{\Omega} \delta \mathbf{v}(\mathbf{x}) \cdot \text{grad}[\psi(\mathbf{x}) - p(\mathbf{x})] \, d\Omega + \int_{\Omega} \delta \mathbf{v}(\mathbf{x}) \cdot \text{div}[2\mu \mathbf{D}(\mathbf{x})] \, d\Omega \\ &= \int_{\partial\Omega} \delta \mathbf{v}(\mathbf{x}) \cdot \hat{\mathbf{n}}(\mathbf{x}) (\psi(\mathbf{x}) - p(\mathbf{x})) \, d\Gamma \\ &\quad - \int_{\Omega} \text{div}[\delta \mathbf{v}(\mathbf{x})] (\psi(\mathbf{x}) - p(\mathbf{x})) \, d\Omega + \int_{\Omega} \delta \mathbf{v}(\mathbf{x}) \cdot \text{div}[2\mu \mathbf{D}(\mathbf{x})] \, d\Omega. \end{aligned} \quad (2.3.14)$$

Noting the symmetry of $\mathbf{D}(\mathbf{x})$ and using Green's identity, the total dissipation due to internal friction can be simplified as

$$\begin{aligned} \int_{\Omega} 2\mu \delta \mathbf{D}(\mathbf{x}) \cdot \mathbf{D}(\mathbf{x}) \, d\Omega &= \int_{\Omega} 2\mu \text{grad}[\delta \mathbf{v}(\mathbf{x})] \cdot \mathbf{D}(\mathbf{x}) \, d\Omega \\ &= \int_{\partial\Omega} 2\mu \delta \mathbf{v}(\mathbf{x}) \cdot \mathbf{D}(\mathbf{x}) \hat{\mathbf{n}}(\mathbf{x}) \, d\Gamma - \int_{\Omega} \delta \mathbf{v}(\mathbf{x}) \cdot \text{div}[2\mu \mathbf{D}(\mathbf{x})] \, d\Omega. \end{aligned} \quad (2.3.15)$$

From equations (2.3.7)–(2.3.8), the total dissipation due to drag and friction satisfies:

$$\begin{aligned} \Phi[\tilde{\mathbf{v}}(\mathbf{x})] - \Phi[\mathbf{v}(\mathbf{x})] &\geq 2 \int_{\partial\Omega} \delta \mathbf{v}(\mathbf{x}) \cdot \hat{\mathbf{n}}(\mathbf{x}) (\psi(\mathbf{x}) - p(\mathbf{x})) \, d\Gamma \\ &\quad - 2 \int_{\Omega} \text{div}[\delta \mathbf{v}(\mathbf{x})] (\psi(\mathbf{x}) - p(\mathbf{x})) \, d\Omega \\ &\quad + 2 \int_{\partial\Omega} 2\mu \delta \mathbf{v}(\mathbf{x}) \cdot \mathbf{D}(\mathbf{x}) \hat{\mathbf{n}}(\mathbf{x}) \, d\Gamma = 0. \end{aligned} \quad (2.3.16)$$

This completes the proof. \square

We now show that the uniqueness of solution under Darcy-Brinkman equations is a direct consequence of the minimum dissipation inequality.

Theorem 2.3.4 (Uniqueness theorem). *The solution to Darcy-Brinkman equations (2.2.3a)–(2.2.3d) is unique up to an arbitrary constant for the pressure given $\mathbf{b}(\mathbf{x})$, $\mathbf{v}^p(\mathbf{x})$ and $\mathbf{t}^p(\mathbf{x})$.*

Proof. On the contrary assume that $\{\mathbf{v}_1(\mathbf{x}), p_1(\mathbf{x})\}$ and $\{\mathbf{v}_2(\mathbf{x}), p_2(\mathbf{x})\}$ are two solutions to Darcy-Brinkman equations for the prescribed data. Let us consider the following quantity:

$$\begin{aligned} \mathcal{I} &:= \int_{\Omega} \alpha(\mathbf{x}) (\mathbf{v}_1(\mathbf{x}) - \mathbf{v}_2(\mathbf{x})) \cdot (\mathbf{v}_1(\mathbf{x}) - \mathbf{v}_2(\mathbf{x})) \, d\Omega \\ &\quad + \int_{\Omega} 2\mu (\mathbf{D}_1(\mathbf{x}) - \mathbf{D}_2(\mathbf{x})) \cdot (\mathbf{D}_1(\mathbf{x}) - \mathbf{D}_2(\mathbf{x})) \, d\Omega. \end{aligned}$$

Noting that $\operatorname{div}[\mathbf{v}_1] = 0$ and $\operatorname{div}[\mathbf{v}_2] = 0$, the second integral can be simplified as

$$\begin{aligned} &\int_{\Omega} 2\mu (\mathbf{D}_1(\mathbf{x}) - \mathbf{D}_2(\mathbf{x})) \cdot (\mathbf{D}_1(\mathbf{x}) - \mathbf{D}_2(\mathbf{x})) \, d\Omega \\ &= \int_{\Omega} (\mathbf{D}_1(\mathbf{x}) - \mathbf{D}_2(\mathbf{x})) \cdot (\mathbf{T}_1(\mathbf{x}) - \mathbf{T}_2(\mathbf{x})) \, d\Omega \\ &= \int_{\Omega} \operatorname{grad} [\mathbf{v}_1(\mathbf{x}) - \mathbf{v}_2(\mathbf{x})] \cdot (\mathbf{T}_1(\mathbf{x}) - \mathbf{T}_2(\mathbf{x})) \, d\Omega. \end{aligned}$$

In obtaining the above equation, we have used the fact that $\mathbf{T}_1(\mathbf{x})$ and $\mathbf{T}_2(\mathbf{x})$ are symmetric. Using Green's identity, the above equation can be written as

$$\begin{aligned} &\int_{\Omega} 2\mu (\mathbf{D}_1(\mathbf{x}) - \mathbf{D}_2(\mathbf{x})) \cdot (\mathbf{D}_1(\mathbf{x}) - \mathbf{D}_2(\mathbf{x})) \, d\Omega \\ &= \int_{\partial\Omega} (\mathbf{v}_1(\mathbf{x}) - \mathbf{v}_2(\mathbf{x})) \cdot (\mathbf{T}_1(\mathbf{x}) - \mathbf{T}_2(\mathbf{x})) \hat{\mathbf{n}}(\mathbf{x}) \, d\Gamma \\ &\quad - \int_{\Omega} (\mathbf{v}_1(\mathbf{x}) - \mathbf{v}_2(\mathbf{x})) \cdot (\operatorname{div}[\mathbf{T}_1] - \operatorname{div}[\mathbf{T}_2]) \, d\Omega. \end{aligned}$$

Using boundary conditions and the balance of linear momentum, we get

$$\begin{aligned} \int_{\Omega} 2\mu (\mathbf{D}_1(\mathbf{x}) - \mathbf{D}_2(\mathbf{x})) \cdot (\mathbf{D}_1(\mathbf{x}) - \mathbf{D}_2(\mathbf{x})) \, d\Omega \\ = - \int_{\Omega} \alpha(\mathbf{x}) (\mathbf{v}_1(\mathbf{x}) - \mathbf{v}_2(\mathbf{x})) \cdot (\mathbf{v}_1(\mathbf{x}) - \mathbf{v}_2(\mathbf{x})) \, d\Omega. \end{aligned}$$

This implies that $\mathcal{I} = 0$. Since $\alpha(\mathbf{x}) > 0 \, \forall \mathbf{x} \in \Omega$ and $\mu > 0$ in Ω , one can conclude that

$$\mathbf{v}_1(\mathbf{x}) = \mathbf{v}_2(\mathbf{x}) \quad \forall \mathbf{x} \in \Omega \quad \text{and} \quad (2.3.17a)$$

$$\mathbf{D}_1(\mathbf{x}) = \mathbf{D}_2(\mathbf{x}) \quad \forall \mathbf{x} \in \Omega. \quad (2.3.17b)$$

That is, the velocity and symmetric part of velocity vector field are unique. Using the equation for the balance of linear momentum (2.2.3a) and the fact that the velocity vector field is unique, one can obtain the following equation:

$$\text{grad} [p_1(\mathbf{x}) - p_2(\mathbf{x})] = \mathbf{0} \quad \forall \mathbf{x} \in \Omega. \quad (2.3.18)$$

This further implies that

$$p_1(\mathbf{x}) - p_2(\mathbf{x}) = p_0 \quad \forall \mathbf{x} \in \Omega, \quad (2.3.19)$$

where p_0 is an arbitrary constant. This completes the proof. \square

The solutions to Darcy and Darcy-Brinkman equations possess reciprocal relations similar to the famous Betti's reciprocal relation in the theory of linear elasticity [Truesdell and Noll, 2004, Sadd, 2009] and to a classical reciprocal relation in the area of creeping flows [Guazzelli and Morris, 2012]. The Betti's reciprocal relation is often employed to solve a class of problems in linear elasticity, which otherwise may be difficult to solve. Mathematically, the Betti's reciprocal relation is equivalent to

the existence and symmetry of Green's function. We now precisely state a reciprocal relation that the solutions of Darcy-Brinkman equations satisfy, and then provide a mathematical proof.

Theorem 2.3.5 (Reciprocal relation). *Assume that $\mathbf{v}^p(\mathbf{x}) = \mathbf{0}$ on Γ^v . Let $\{\mathbf{v}_1(\mathbf{x}), p_1(\mathbf{x})\}$ and $\{\mathbf{v}_2(\mathbf{x}), p_2(\mathbf{x})\}$ be the solutions of equations (2.2.3a)–(2.2.3d) for the prescribed data $\{\mathbf{b}_1(\mathbf{x}), \mathbf{t}_1^p(\mathbf{x})\}$ and $\{\mathbf{b}_2(\mathbf{x}), \mathbf{t}_2^p(\mathbf{x})\}$, respectively. Then, these fields satisfy the following relation:*

$$\begin{aligned} \int_{\Omega} \rho \mathbf{b}_1(\mathbf{x}) \cdot \mathbf{v}_2(\mathbf{x}) \, d\Omega + \int_{\Gamma^t} \mathbf{t}_1^p(\mathbf{x}) \cdot \mathbf{v}_2(\mathbf{x}) \, d\Gamma &= \int_{\Omega} \rho \mathbf{b}_2(\mathbf{x}) \cdot \mathbf{v}_1(\mathbf{x}) \, d\Omega \\ &+ \int_{\Gamma^t} \mathbf{t}_2^p(\mathbf{x}) \cdot \mathbf{v}_1(\mathbf{x}) \, d\Gamma. \end{aligned} \quad (2.3.20)$$

Proof. Let us start with the left side of equation (2.3.20). Noting that $\mathbf{v}^p(\mathbf{x}) = \mathbf{0}$ on Γ^v and $\Gamma^v \cup \Gamma^t = \partial\Omega$, one can proceed as

$$\begin{aligned} &\int_{\Omega} \rho \mathbf{b}_1(\mathbf{x}) \cdot \mathbf{v}_2(\mathbf{x}) \, d\Omega + \int_{\Gamma^t} \mathbf{t}_1^p(\mathbf{x}) \cdot \mathbf{v}_2(\mathbf{x}) \, d\Gamma \\ &= \int_{\Omega} \rho \mathbf{b}_1(\mathbf{x}) \cdot \mathbf{v}_2(\mathbf{x}) \, d\Omega + \int_{\Gamma^t} (\mathbf{T}_1 \hat{\mathbf{n}}(\mathbf{x})) \cdot \mathbf{v}_2(\mathbf{x}) \, d\Gamma \\ &= \int_{\Omega} \rho \mathbf{b}_1(\mathbf{x}) \cdot \mathbf{v}_2(\mathbf{x}) \, d\Omega + \int_{\partial\Omega} (\mathbf{T}_1 \hat{\mathbf{n}}(\mathbf{x})) \cdot \mathbf{v}_2(\mathbf{x}) \, d\Gamma \\ &= \int_{\Omega} \rho \mathbf{b}_1(\mathbf{x}) \cdot \mathbf{v}_2(\mathbf{x}) \, d\Omega + \int_{\Omega} \operatorname{div} [\mathbf{T}_1^T(\mathbf{x}) \mathbf{v}_2(\mathbf{x})] \, d\Omega \\ &= \int_{\Omega} (\rho \mathbf{b}_1(\mathbf{x}) + \operatorname{div}[\mathbf{T}_1]) \cdot \mathbf{v}_2(\mathbf{x}) \, d\Omega + \int_{\Omega} \mathbf{T}_1(\mathbf{x}) \cdot \operatorname{grad} [\mathbf{v}_2] \, d\Omega \\ &= \int_{\Omega} (\alpha(\mathbf{x}) \mathbf{v}_1(\mathbf{x}) \cdot \mathbf{v}_2(\mathbf{x}) + (-p_1(\mathbf{x}) \mathbf{I} + 2\mu \mathbf{D}_1(\mathbf{x})) \cdot \operatorname{grad} [\mathbf{v}_2]) \, d\Omega \\ &= \int_{\Omega} \alpha(\mathbf{x}) \mathbf{v}_1(\mathbf{x}) \cdot \mathbf{v}_2(\mathbf{x}) \, d\Omega - \int_{\Omega} p_1(\mathbf{x}) \operatorname{div} [\mathbf{v}_2] \, d\Omega \\ &+ \int_{\Omega} 2\mu \mathbf{D}_1(\mathbf{x}) \cdot \mathbf{D}_2(\mathbf{x}) \, d\Omega. \end{aligned}$$

In the above step, we have used the fact that $\mathbf{D}_1(\mathbf{x})$ is a symmetric second-order

tensor. Since $\operatorname{div} [\mathbf{v}_2] = 0$ we have

$$\begin{aligned} \int_{\Omega} \rho \mathbf{b}_1(\mathbf{x}) \cdot \mathbf{v}_2(\mathbf{x}) \, d\Omega + \int_{\Gamma^t} \mathbf{t}_1^p(\mathbf{x}) \cdot \mathbf{v}_2(\mathbf{x}) \, d\Gamma &= \int_{\Omega} \alpha(\mathbf{x}) \mathbf{v}_1(\mathbf{x}) \cdot \mathbf{v}_2(\mathbf{x}) \, d\Omega \\ &+ \int_{\Omega} 2\mu \mathbf{D}_1(\mathbf{x}) \cdot \mathbf{D}_2(\mathbf{x}) \, d\Omega. \end{aligned}$$

Similarly, it can be shown that the right side of equation (2.3.20) is also equal to

$$\int_{\Omega} \alpha(\mathbf{x}) \mathbf{v}_1(\mathbf{x}) \cdot \mathbf{v}_2(\mathbf{x}) \, d\Omega + \int_{\Omega} 2\mu \mathbf{D}_1(\mathbf{x}) \cdot \mathbf{D}_2(\mathbf{x}) \, d\Omega.$$

This completes the proof. \square

The following notation will be used later to verify the reciprocal relation:

$$\varepsilon_{\text{reciprocal}} := \frac{\text{left integral} - \text{right integral}}{\text{left integral}}. \quad (2.3.21)$$

where the left and right integrals are, respectively, defined as

$$\text{left integral} := \int_{\Omega} \rho \mathbf{b}_1(\mathbf{x}) \cdot \mathbf{v}_2(\mathbf{x}) \, d\Omega + \int_{\Gamma^t} \mathbf{t}_1^p(\mathbf{x}) \cdot \mathbf{v}_2(\mathbf{x}) \, d\Gamma \quad \text{and} \quad (2.3.22a)$$

$$\text{right integral} := \int_{\Omega} \rho \mathbf{b}_2(\mathbf{x}) \cdot \mathbf{v}_1(\mathbf{x}) \, d\Omega + \int_{\Gamma^t} \mathbf{t}_2^p(\mathbf{x}) \cdot \mathbf{v}_1(\mathbf{x}) \, d\Gamma. \quad (2.3.22b)$$

Remark 2.3.6. *The corresponding reciprocal relation for Darcy equations can be written as follows: Assume that $v_n(\mathbf{x}) = 0$ on Γ^v . Let $\{\mathbf{v}_1(\mathbf{x}), p_1(\mathbf{x})\}$ and $\{\mathbf{v}_2(\mathbf{x}), p_2(\mathbf{x})\}$ be the solutions of equations (2.2.3a)–(2.2.3d) for the prescribed data $\{\mathbf{b}_1(\mathbf{x}), p_{01}(\mathbf{x})\}$ and $\{\mathbf{b}_2(\mathbf{x}), p_{02}(\mathbf{x})\}$, respectively. Then, these fields satisfy the following relation:*

$$\begin{aligned} \int_{\Omega} \rho \mathbf{b}_1(\mathbf{x}) \cdot \mathbf{v}_2(\mathbf{x}) \, d\Omega - \int_{\Gamma^t} p_{01}(\mathbf{x}) \hat{\mathbf{n}}(\mathbf{x}) \cdot \mathbf{v}_2(\mathbf{x}) \, d\Gamma \\ = \int_{\Omega} \rho \mathbf{b}_2(\mathbf{x}) \cdot \mathbf{v}_1(\mathbf{x}) \, d\Omega - \int_{\Gamma^t} p_{02}(\mathbf{x}) \hat{\mathbf{n}}(\mathbf{x}) \cdot \mathbf{v}_1(\mathbf{x}) \, d\Gamma. \end{aligned} \quad (2.3.23)$$

Remark 2.3.7. *It needs to be emphasized that the reciprocal relation will not directly*

be able to assess the accuracy of the pressure field in the computational domain. The reciprocal relation is ideal for assessing the accuracy of the velocity vector field in the domain and the accuracy of the implementation of prescribed traction boundary conditions. This reciprocal relation will not be able to provide information about the accuracy of the implementation of non-zero velocity boundary conditions.

Next, we discuss in the form of a theorem on the nature of the vorticity under the Darcy and Darcy-Brinkman models. To this end,

$$\boldsymbol{\omega}(\mathbf{x}) \equiv \text{curl}[\mathbf{v}(\mathbf{x})]. \quad (2.3.24)$$

In a Cartesian coordinate system, the components of vorticity take the following form:

$$\omega_x = \frac{\partial v_z}{\partial y} - \frac{\partial v_y}{\partial z}, \quad \omega_y = \frac{\partial v_x}{\partial z} - \frac{\partial v_z}{\partial x}, \quad \omega_z = \frac{\partial v_y}{\partial x} - \frac{\partial v_x}{\partial y}. \quad (2.3.25)$$

It should be emphasized that $\text{curl}[\cdot]$ operator is defined only in \mathbb{R}^3 (i.e., the three-dimensional Euclidean space). However, for two-dimensional problems, one can consider the vorticity as

$$\boldsymbol{\omega}(\mathbf{x}, y) = \omega_z(\mathbf{x}, y)\hat{\mathbf{e}}_z, \quad (2.3.26)$$

where z denotes the axis perpendicular to the two-dimensional plane in which the problem is defined, and $\hat{\mathbf{e}}_z$ is the unit vector along the z -direction.

Theorem 2.3.8 (On the nature of vorticity under Darcy and Darcy-Brinkman models). *Assume that the medium is isotropic and homogeneous (i.e., $\alpha(\mathbf{x})$ is a constant scalar), the body force is a conservative vector field (i.e., $\rho\mathbf{b}(\mathbf{x}) = -\text{grad}[\psi(\mathbf{x})]$), and the response is steady-state. Then the vorticity vanishes under Darcy equations. Under Darcy-Brinkman equations, the vorticity is an eigenvector of the Laplacian with $1/k$ as the eigenvalue. Moreover, the vorticity satisfies a maximum principle in which*

the non-negative maximum and the non-positive minimum occur on the boundary.

Proof. By taking the curl on both sides of the balance of linear momentum under Darcy equations (2.2.2a) we obtain

$$\operatorname{curl}[\alpha \mathbf{v}] = -\operatorname{curl}[\operatorname{grad}[\psi + p]] = \mathbf{0}. \quad (2.3.27)$$

Since α is spatially homogeneous scalar, one can conclude that the vorticity vanishes under the Darcy model.

The incompressibility constraint implies that the balance of linear momentum under the Darcy-Brinkman model can be written as

$$\alpha \mathbf{v}(\mathbf{x}) + \operatorname{grad}[p(\mathbf{x})] - \mu \operatorname{div}[\operatorname{grad}[\mathbf{v}]] = -\operatorname{grad}[\psi]. \quad (2.3.28)$$

By taking curl on both sides of the above equation, we get

$$\Delta \boldsymbol{\omega}(\mathbf{x}) = \frac{1}{k} \boldsymbol{\omega}(\mathbf{x}), \quad (2.3.29)$$

where Δ denotes the Laplacian operator and k is the permeability. The above equation is a *vector* eigenvalue problem in which the vorticity vector is the eigenvector, and $1/k$ is the corresponding eigenvalue. For two-dimensional problems, we have

$$\Delta_{2D} \omega_z(x, y) = \frac{1}{k} \omega_z(x, y), \quad (2.3.30)$$

where Δ_{2D} denotes the two-dimensional Laplacian operator. The above equation is a *scalar* eigenvalue problem in which $\omega_z(x, y)$ is the eigenvector and $1/k$ is the corresponding eigenvalue.

Since $1/k > 0$, this equation is commonly referred to as diffusion with decay, which is a linear self-adjoint elliptic partial differential equation. It is well-known

that such a partial differential equation satisfies a maximum principle [Gilbarg and Trudinger, 2001]. Mathematically, the maximum principle for the vorticity under the Darcy-Brinkman model takes the following form: If $w_z(\mathbf{x}) \in C^2(\Omega) \cap C^0(\bar{\Omega})$, then the non-negative maximum and the non-positive minimum occur on the boundary. That is,

$$\max_{\mathbf{x} \in \bar{\Omega}} [\omega_z(\mathbf{x})] \leq \max \left[0, \max_{\mathbf{x} \in \partial\Omega} \omega_z(\mathbf{x}) \right] \quad \text{and} \quad (2.3.31a)$$

$$\min_{\mathbf{x} \in \bar{\Omega}} [\omega_z(\mathbf{x})] \geq \min \left[0, \min_{\mathbf{x} \in \partial\Omega} \omega_z(\mathbf{x}) \right], \quad (2.3.31b)$$

where $C^2(\Omega)$ denotes the set of twice differentiable functions defined on Ω , and $C^0(\bar{\Omega})$ is the set of functions that are continuous to the boundary. \square

The maximum principle can be utilized to verify the accuracy of numerical solutions by plotting vorticity and checking whether the non-negative maximum and non-positive minimum of the vorticity occur on the boundary. For the Darcy model with isotropic and homogeneous medium properties and conservative body force, it can be shown that the vorticity vanishes (i.e., $\boldsymbol{\omega}(\mathbf{x}) = \mathbf{0}$). However, it should be noted that heterogeneity, pressure-dependent viscosity, or non-conservative body force can introduce vorticity under the Darcy model. All the above results can serve as invaluable tools to assess the performance of a numerical formulation to verify a computer implementation, and to provide metrics for numerical convergence.

2.4 Steady-state numerical results

We shall first non-dimensionalize the governing equations by choosing primary variables that seem appropriate for problems arising in modeling of flows through

porous media. This non-dimensional procedure is different from the standard non-dimensionalization procedure for incompressible Navier-Stokes in the choice of primary variables. In the standard non-dimensionalization of Navier-Stokes equations, one employs characteristic velocity v , characteristic length L and density of the fluid ρ as primary variables. We shall choose L (reference length in the problem), g (acceleration due to gravity) and p_{atm} (atmospheric pressure) as the reference quantities. Using these reference quantities, we define the following non-dimensional quantities:

$$\begin{aligned}\bar{\mathbf{x}} &= \frac{\mathbf{x}}{L}, \quad \bar{\mathbf{v}} = \frac{\mathbf{v}}{\sqrt{gL}}, \quad \bar{\mathbf{v}}^p = \frac{\mathbf{v}^p}{\sqrt{gL}}, \quad \bar{\mathbf{T}} = \frac{\mathbf{T}}{p_{\text{atm}}}, \quad \bar{\mathbf{b}} = \frac{\mathbf{b}}{g}, \quad \bar{p} = \frac{p}{p_{\text{atm}}}, \\ \bar{p}_0 &= \frac{p_0}{p_{\text{atm}}}, \quad \bar{\rho} = \frac{\rho g L}{p_{\text{atm}}}, \quad \bar{\alpha} = \frac{\alpha \sqrt{gL^3}}{p_{\text{atm}}}, \quad \bar{\mu} = \frac{\mu \sqrt{g/L}}{p_{\text{atm}}}, \quad \bar{k} = \frac{k}{L^2},\end{aligned}\tag{2.4.1}$$

where the non-dimensional quantities are denoted by superposed bars. The gradient and divergence operators with respect to $\bar{\mathbf{x}}$ are denoted as $\overline{\text{grad}}[\cdot]$ and $\overline{\text{div}}[\cdot]$, respectively. The scaled domain Ω_{scaled} is defined as follows: A point in space with position vector $\bar{\mathbf{x}} \in \Omega_{\text{scaled}}$ corresponds to the same point with position vector given by $\mathbf{x} = \bar{\mathbf{x}}L \in \Omega$. Similarly, one can define the scaled boundaries: $\partial\Omega_{\text{scaled}}$, Γ_{scaled}^v , and Γ_{scaled}^p . Using the above non-dimensionalization procedure, Darcy-Brinkman equations can be written as

$$\bar{\alpha}(\bar{\mathbf{x}})\bar{\mathbf{v}}(\bar{\mathbf{x}}) + \overline{\text{grad}}[\bar{p}(\bar{\mathbf{x}})] - \overline{\text{div}}[2\bar{\mu}\bar{\mathbf{D}}(\bar{\mathbf{x}})] = \bar{\rho}\bar{\mathbf{b}}(\bar{\mathbf{x}}) \quad \text{in } \Omega_{\text{scaled}},\tag{2.4.2a}$$

$$\overline{\text{div}}[\bar{\mathbf{v}}(\bar{\mathbf{x}})] = 0 \quad \text{in } \Omega_{\text{scaled}},\tag{2.4.2b}$$

$$\bar{\mathbf{v}}(\bar{\mathbf{x}}) = \bar{\mathbf{v}}^p(\bar{\mathbf{x}}) \quad \text{on } \Gamma_{\text{scaled}}^v, \quad \text{and}\tag{2.4.2c}$$

$$\bar{\mathbf{t}}(\bar{\mathbf{x}}) = \bar{\mathbf{t}}^p(\bar{\mathbf{x}}) \quad \text{on } \Gamma_{\text{scaled}}^t.\tag{2.4.2d}$$

Similarly, one could write the corresponding non-dimensional form of Darcy equations. For simplicity, the "over-lines" will be dropped in the remainder of the paper.

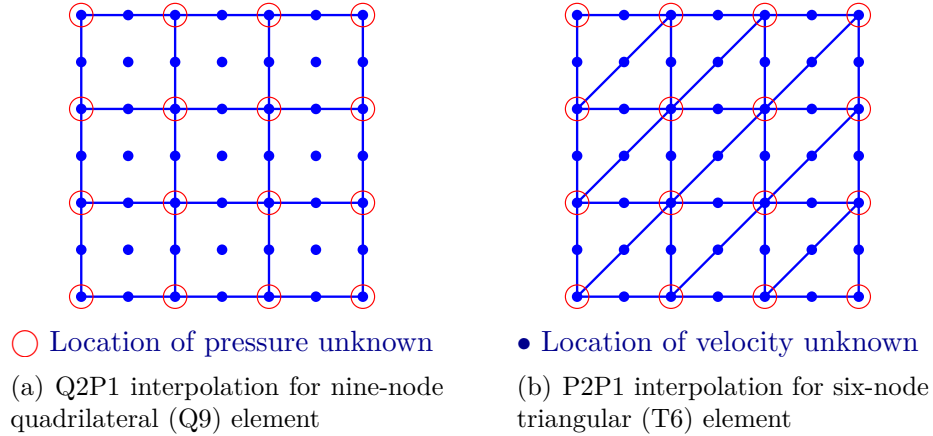


Figure 2.1: This figure shows the typical employed structured finite element. We use Q2P1 and P2P1 mixed interpolations for unknowns (i.e., second-order interpolation for the velocity field, and first-order for the pressure field).

We shall use several flow through porous media problems with different boundary conditions to illustrate that the proposed *a posteriori* techniques can be used as good measures for the accuracy and convergence of numerical results. We have employed P2P1 (which is based on six-node triangle element T6) and Q2P1 (which is based on nine-node quadrilateral element Q9) interpolations available in COMSOL [COMSOL Multiphysics, 2013]. Consistent SUPG stabilization has been employed if the interpolations (i.e., Q2P1 and P2P1) violate the LBB *inf-sup* stability condition [Hughes et al., 1986a, COMSOL Multiphysics, 2013]. Typical structured finite elements utilized in this paper are shown in Figure 2.1. Unless mentioned otherwise, all the elements in a quadrilateral mesh are squares and all the elements in a triangular mesh are right-angled isosceles triangles. In this numerical solution study, we have taken h (the maximum element size) to be equal to the length of the side for square elements, and to the length of the base (or height) for right-angled isosceles triangles.

Table 2.1: Body force problem: Non-dimensional parameters used in the problem.

Parameter	Value
α	1
μ	1 and 0.001
ρ	1
L	1
$\mathbf{b}(\mathbf{x})$	$a[\sin(\pi x), \cos(\pi y)]$

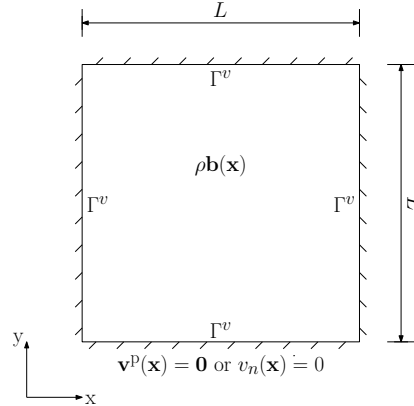


Figure 2.2: Body force problem: The computational domain is a square with $L = 1$. The prescribed conservative body force is $\rho \mathbf{b}(\mathbf{x}) = 10 \times [\sin(\pi x), \cos(\pi y)]$. Homogeneous velocity is enforced on the entire boundary (i.e., $\Gamma^v = \partial\Omega$).

2.4.1 Body force problem

The test problem is pictorially described in Figure 2.2. The non-dimensional parameters used in the numerical simulation are provided in Table 2.1. The conservative body force is taken as $\rho \mathbf{b}(\mathbf{x}) = 10[\sin(\pi x), \cos(\pi y)]$ (i.e., $a = 10$). Velocity boundary condition is prescribed on the entire boundary (i.e., $\Gamma^v = \partial\Omega$). For the Darcy-Brinkman model, we assume $\mathbf{v}^p(\mathbf{x}) = \mathbf{0}$; and for the Darcy model, we assume $v_n(\mathbf{x}) = 0$. Figure 2.3 shows the minimum total mechanical power and the minimum dissipation with mesh refinement. The numerical results for the reciprocal relation with mesh refinement are shown in Figure 2.4. All the numerical results are in accordance with the theoretical predictions for this test problem.

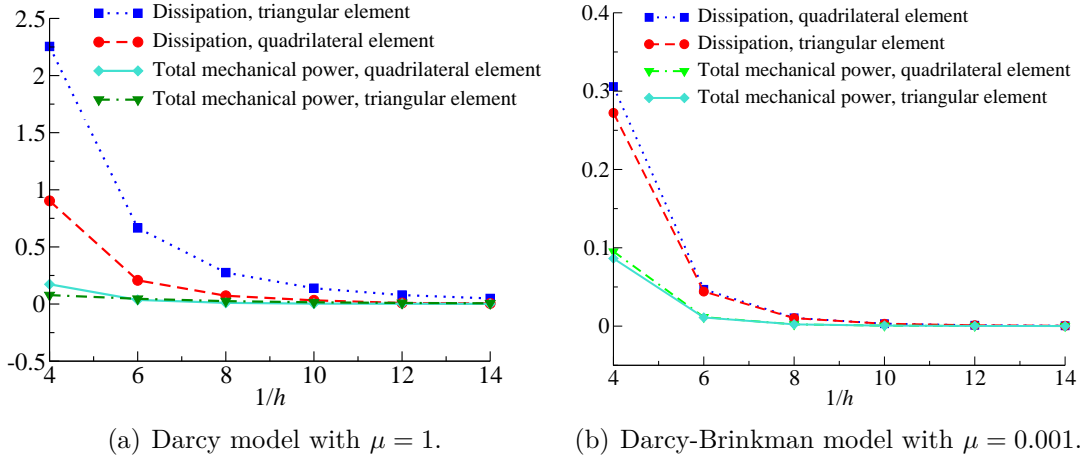


Figure 2.3: Body force problem: This figure shows the variation of dissipation and total mechanical power with mesh refinement under the Darcy and Darcy-Brinkman models using quadrilateral and triangular elements for parameters provided in Table 2.1.

Table 2.2: Lid-driven cavity problem: Non-dimensional parameters used in the problem.

Parameter	Value
α	1
μ	1
ρ	1
L	1

2.4.2 Lid-driven cavity problem

The two-dimensional lid-driven cavity problem is a benchmark study widely used to investigate the accuracy of numerical formulations for various fluid models [Burggraf, 1966, Erturk, 2009]. Figure 2.5 provides a pictorial description of the problem. The domain of the problem is a bi-unit square. Velocity boundary condition is prescribed on the entire boundary (i.e., $\Gamma^v = \partial\Omega$) which implies that the minimum dissipation theorem is also applicable to this problem. It should be noted that lid-driven cavity problem is not compatible with Darcy equations which need only the normal component of the velocity to be prescribed on the boundary. However, the lid-driven cavity problem demands the prescription of the entire velocity vector field on the boundary. We shall therefore employ Darcy-Brinkman model in our numerical

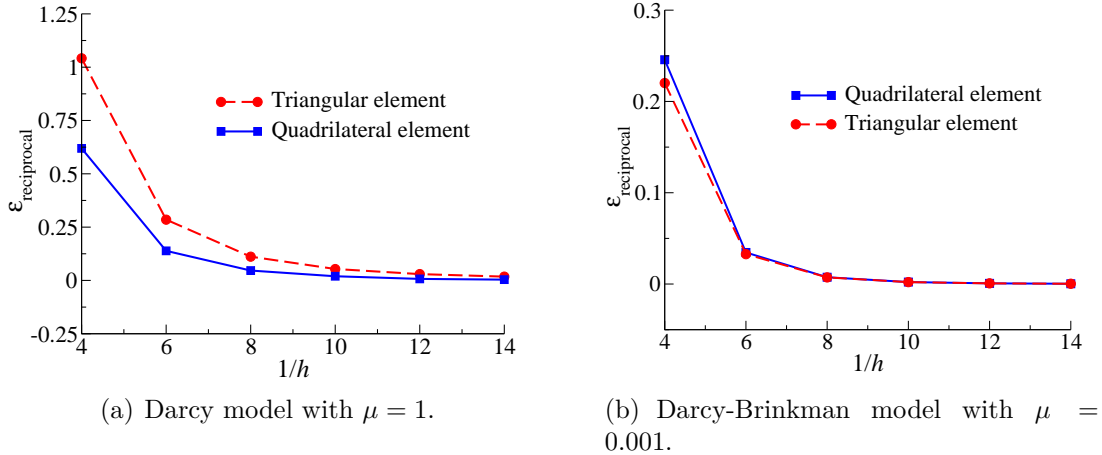


Figure 2.4: Body force problem: This figure shows the variation of $\varepsilon_{\text{reciprocal}}$ with mesh refinement for the Darcy and Darcy-Brinkman models using quadrilateral and triangular elements for parameters provided in Table 2.1.

simulations.

It is crucial to note that the solution to the lid-driven cavity problem has singularities at the top corners which arise due to velocity discontinuity on the boundary [Botella and Peyret, 1998, Batchelor, 2000]. Discontinuities and singularities commonly occur in fluid dynamics, solid mechanics, and structural dynamics and it is a subject of intense research and grave concern in error estimation [Oberkampf et al., 2004]. Some representative works on pollution errors due to singularities and discontinuities are [Babuška and Oh, 1987, Babuška et al., 1995, 1997, Oden et al., 1998, Roache, 1998, Botella and Peyret, 2001]. However, none of these studies utilized the minimum dissipation theorem to detect pollution errors in porous media models.

Herein, we use an adaptive mesh to resolve the singularities in the solution. The non-dimensional parameters used in the lid-driven cavity problem are presented in Table 2.2. Figures 2.6(a) and 2.6(b) show the uniform structured mesh and the adaptive mesh, respectively. For the adaptive mesh, we generate fine grid in the region close to top lid (see Figure 2.6(b)). Figures 2.6(c) and 2.6(d) show variation of the minimum dissipation with mesh refinement for respective grids. Under the adaptive mesh, the dissipation decreased uniformly and converged to a constant value with

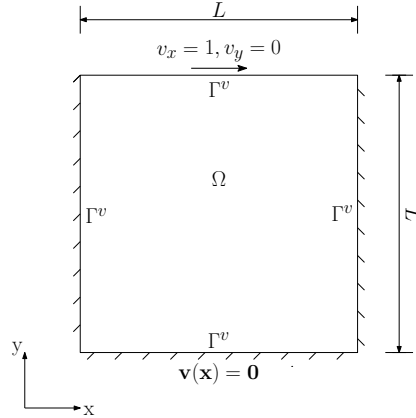
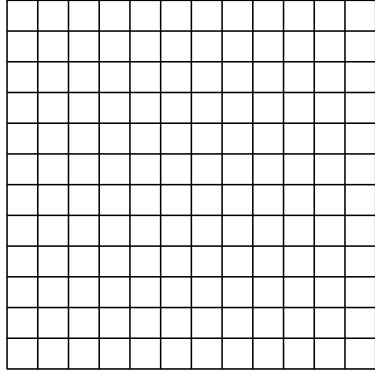


Figure 2.5: Lid-driven cavity problem: The computational domain is a unit square. Velocity is prescribed on the entire boundary (i.e., $\Gamma^v = \partial\Omega$). The prescribed velocity on the top side is $v_x = 1$ and $v_y = 0$ and on the remaining sides is zero.

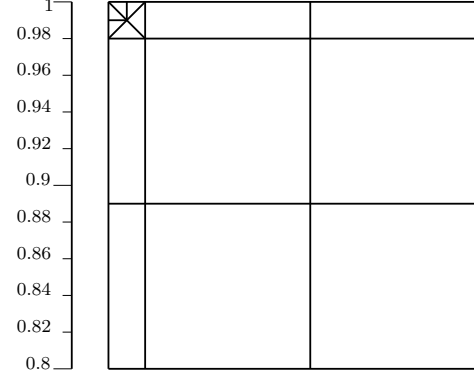
mesh refinement. On the other hand, the dissipation increased monotonically with mesh refinement under the structured mesh. More importantly, due to the presence of singularities and pollution error, the dissipation did not hit a plateau even for very fine meshes (i.e., $1/h \geq 220$). The dissipation reached a plateau relatively quickly under the adaptive mesh (say $1/h = 10$). *This problem clearly illustrates that the minimum dissipation theorem can be used to identify pollution errors in numerical solutions which is one of the main findings of this paper.*

2.4.3 Pipe bend problem

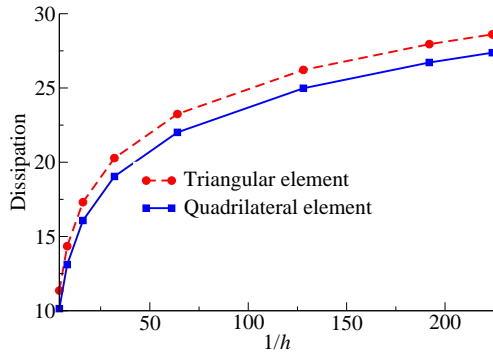
As another application of the proposed techniques, we consider an engineering problem commonly found in the fluid mechanics literature, which is called the pipe bend problem (for example, see References [Borrvall and Petersson, 2003, Hansen et al., 2005, Aage et al., 2008, Pingen et al., 2009, Challis and Guest, 2009, Hassine, 2012]). In the pipe bend problem, the computational domain Ω is a square with $L = 1$.



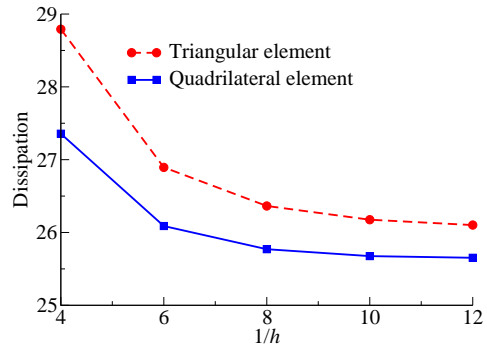
(a) Uniform structured mesh with $1/h = 12$.



(b) Adaptive mesh near the top left corner with $1/h = 12$ elsewhere.



(c) Dissipation vs. h under a hierarchy of uniform structured meshes.



(d) Dissipation vs. h under a hierarchy of adaptive meshes.

Figure 2.6: Lid-driven cavity problem: The top figures show a uniform structured mesh, and an adaptive mesh near the top corners. The bottom figures show the variation of total dissipation with mesh refinement.

2.4.3.1 Velocity boundary condition

The problem is pictorially described in Figure 2.7. An inflow parabolic velocity is enforced on a part of the left boundary and an outflow parabolic velocity on a segment of the bottom. Each parabolic velocity profile has a unit maximum value (i.e., $v_{x_{max}} = 1$ or $v_{y_{max}} = 1$). Elsewhere, the homogeneous velocity is prescribed (i.e., $\mathbf{v}^p(\mathbf{x}) = \mathbf{0}$ for the Darcy-Brinkman model and $v_n(\mathbf{x}) = 0$ for the Darcy model). The velocity boundary condition makes the problem compatible with the total mechanical power and the dissipation theorems. The non-dimensional parameters used

Table 2.3: Pipe bend problem: Non-dimensional parameters of the parabolic velocity boundary condition problem.

Parameter	Value
α	1 and 10
μ	1 and 0.001
ρ	1
$\mathbf{b}(\mathbf{x})$	[1, 1]
L	1

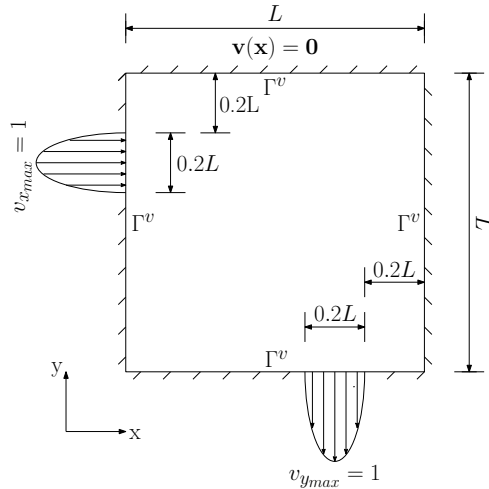


Figure 2.7: Pipe bend problem (velocity boundary condition): A pictorial description of the problem. The computational domain Ω is a unit square. The velocity boundary condition is prescribed on the entire boundary (i.e., $\Gamma^v = \partial\Omega$).

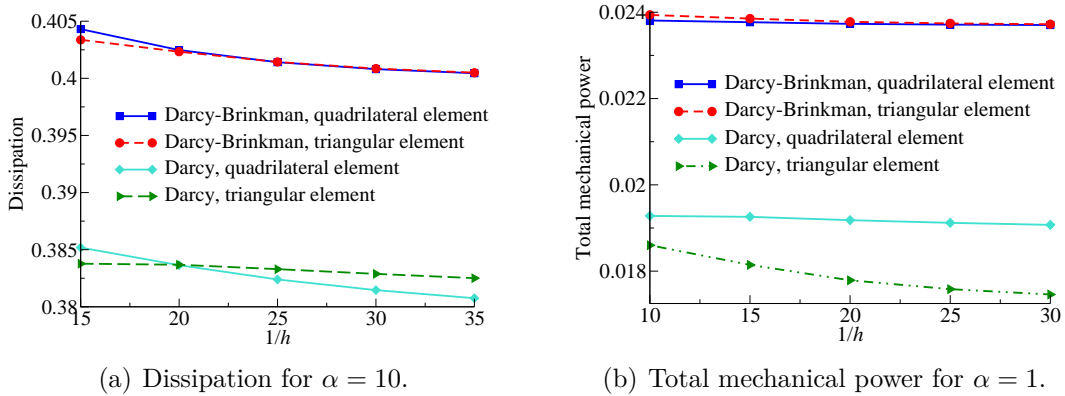


Figure 2.8: Pipe bend problem (velocity boundary condition): The figure shows that the dissipation and total mechanical power decrease uniformly with mesh refinement for the Darcy and Darcy-Brinkman models.

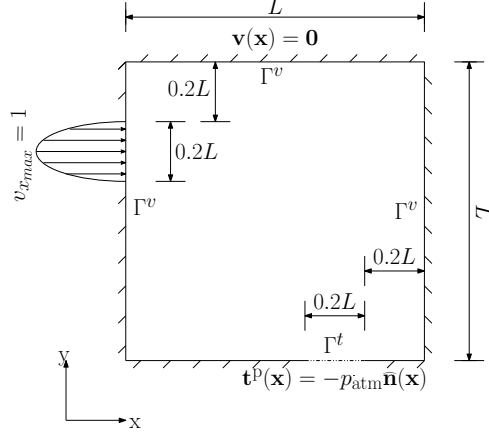


Figure 2.9: Pipe bend problem (velocity-pressure boundary condition): The computational domain Ω is a square with $L = 1$. The traction boundary condition is $\mathbf{t}^p(\mathbf{x}) = -p_{\text{atm}}\hat{\mathbf{n}}(\mathbf{x})$ on Γ^t .

Table 2.4: Pipe bend problem: Non-dimensional parameters of the zero velocity (wall)-pressure boundary conditions.

Parameter	Value
α	1
μ	0.001
ρ	1
p_{inj}	5 and 7.5
p_{atm}	1
L	1

in the problem are presented in Table 2.3. Figure 2.8 shows the variation of minimum total mechanical power and minimum dissipation with mesh refinement for the quadrilateral and triangular elements. The result of the numerical solutions verification are presented in Figure 2.8(a) and 2.8(b) for the minimum dissipation and the total mechanical power, respectively. The numerical error decreases and converges uniformly.

2.4.3.2 Parabolic velocity-pressure boundary condition

A pictorial description of the problem is given by Figure 2.9). The traction is prescribed on a part of the bottom boundary (i.e., $\mathbf{t}^p(\mathbf{x}) = -p_{\text{atm}}\hat{\mathbf{n}}(\mathbf{x})$ on Γ^t). The

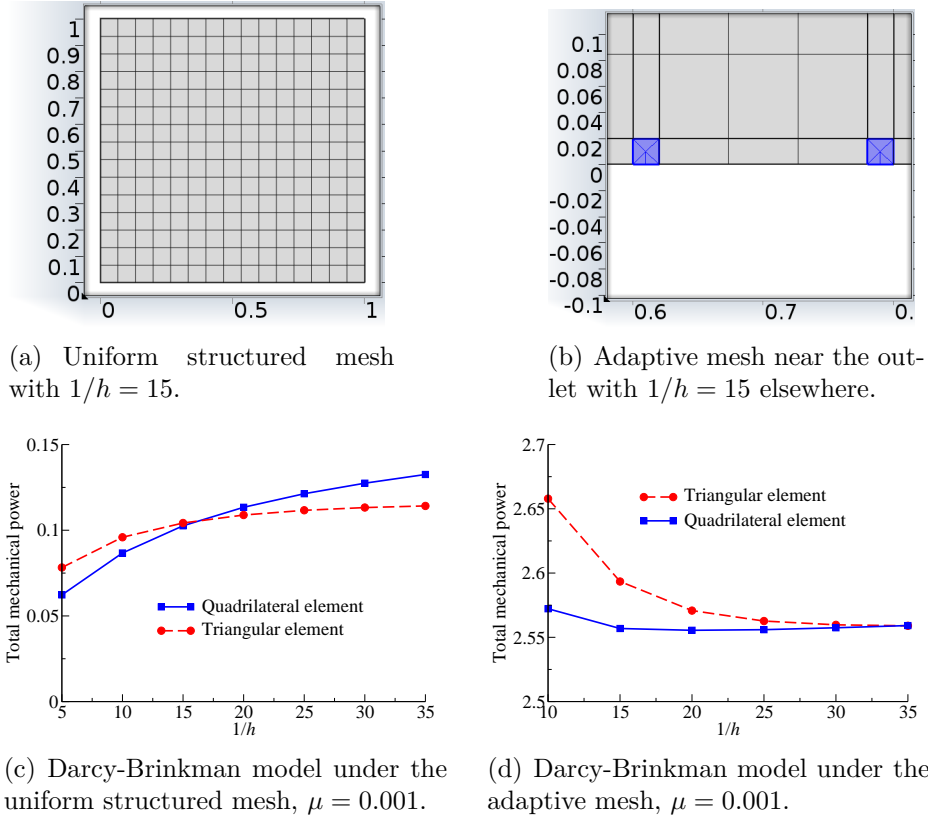


Figure 2.10: Pipe bend problem (velocity-pressure boundary condition): The top figures show the uniform structured mesh and the adaptive mesh near the corners of the outlet. The bottom figures show the variation of the total mechanical power with mesh refinement.

velocity has parabolic profile with unit maximum value (i.e., $v_{x_{max}} = 1$) prescribed on a segment of the left boundary. Elsewhere, the homogeneous velocity is enforced. On account of the traction and parabolic velocity boundary conditions, current problem is not compatible with the minimum dissipation and reciprocal theorems. It is only compatible with the total mechanical power theorem. It should be noted that the solution to the problem has the singularity at near corners of the outlet (i.e., Γ^t). Hence, we again use an adaptive mesh to resolve the pollution in the solution. The non-dimensional parameters using in the problem are provided in Table 2.3. Figure 2.10 depicts the variation of the minimum total mechanical power with mesh refinement for the quadrilateral and triangular elements. The top figures show the uniform structured and adaptive meshes. Under the structured mesh, the total mechanical

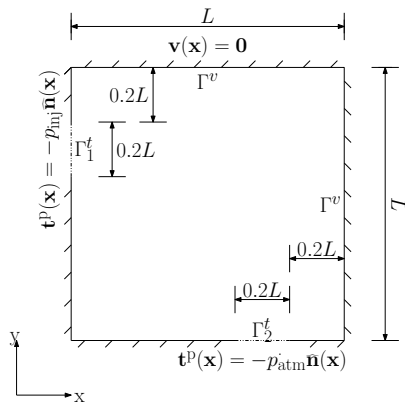
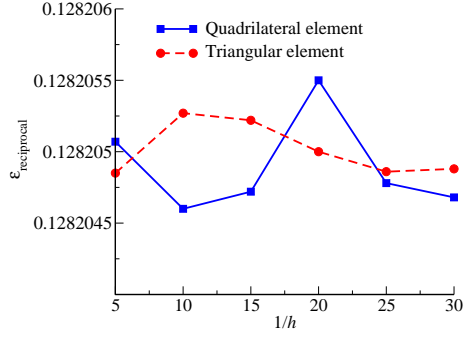


Figure 2.11: Pressure pipe bend problem (pressure-pressure boundary condition): The computational domain Ω is a unit square. The traction is prescribed on a part on the left side and on a part on the bottom side.

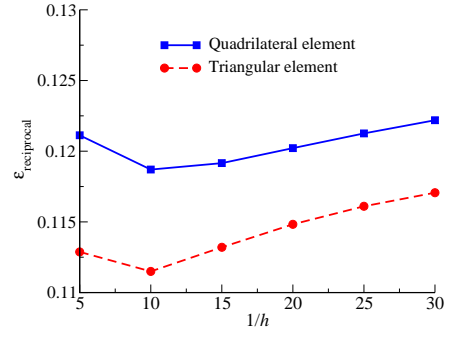
power increased uniformly with mesh refinement due to the polluted area in the computational domain. The error decreased uniformly and converged to a constant value with mesh refinement using the adaptive mesh. So, in addition to error estimation capability, the total mechanical power theorem can be used to identify the pollution errors in the numerical solutions.

2.4.3.3 Velocity-pressure boundary condition

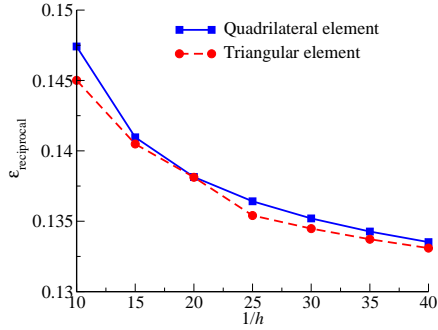
The pictorial description of the problem is shown in Figure 2.11. The traction is prescribed on a segment of the left boundary (i.e., $\mathbf{t}^p(\mathbf{x}) = -p_{inj}\hat{\mathbf{n}}(\mathbf{x})$ on Γ_1^t) and bottom boundary (i.e., $\mathbf{t}^p(\mathbf{x}) = -p_{atm}\hat{\mathbf{n}}(\mathbf{x})$ on Γ_2^t). Elsewhere, the homogeneous velocity is enforced. The non-dimensional parameters used in the problem are presented in Table 2.4. Current problem is compatible for the reciprocal relation, due to the prescription of the traction and homogeneous velocity on the boundary. The variation of the error in the reciprocal relation with mesh refinement using the triangular and quadrilateral elements is shown in Figure 2.12. Due to the singularity near the corners of the outlet (i.e., Γ_2^t) the results for the regular structured mesh is uniform but increasing. However, the error decreases uniformly under the adaptive mesh.



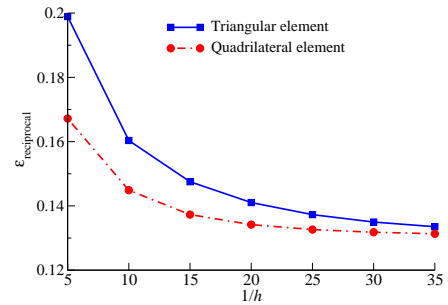
(a) Darcy model under the uniform structured mesh.



(b) Darcy-Brinkman model under the uniform structured mesh.



(c) Darcy model under the adaptive mesh.



(d) Darcy-Brinkman model under the adaptive mesh.

Figure 2.12: Pressure pipe bend problem (pressure-pressure boundary condition): The figure shows the variation of $\varepsilon_{\text{reciprocal}}$ with mesh refinement for the Darcy and Darcy-Brinkman models using quadrilateral and triangular finite elements.

2.4.4 Pressure slab problem

Figure 2.13 provides a pictorial description of the problem. The non-dimensional parameters used in the numerical simulation are provided in Table 2.5. The domain is a $W \times L$ rectangle. The homogeneous velocity boundary condition is enforced on the top and bottom sides of the boundary. The traction is prescribed on the left side (i.e., $\mathbf{t}^p(\mathbf{x}) = -p_{\text{inj}}\hat{\mathbf{n}}(\mathbf{x})$ on Γ_1^t) and on the right side (i.e., $\mathbf{t}^p(\mathbf{x}) = -p_{\text{atm}}\hat{\mathbf{n}}(\mathbf{x})$ on Γ_2^t). We shall use this test problem to assess the accuracy of numerical solutions with respect to the reciprocal relation. Figure 2.14 depicts the variation of the error in the reciprocal relation with mesh refinement for the triangular and quadrilateral grids. The error in the reciprocal relations under Darcy equations is very close to zero for

Table 2.5: Pressure slab problem: Non-dimensional parameters used in the problem.

Parameter	Value
α	1
μ	0.001
ρ	1
p_{inj}	5 and 7.5
p_{atm}	1
L	1
W	0.2

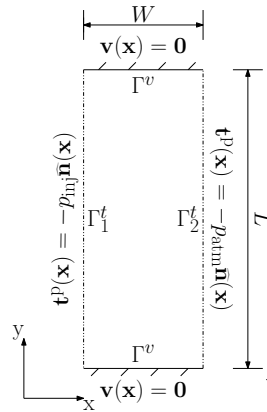


Figure 2.13: Pressure slab problem: The computational domain is a $W \times L$ rectangle. The traction is prescribed on the left side of the boundary and on the right side. Elsewhere, homogeneous velocity is enforced.

all the meshes. The error under Darcy-Brinkman equations decrease uniformly with mesh refinement. All the numerical results are in accordance with the theoretical predictions.

2.4.5 Pressure driven problem

The domain is a square with $L = 1$. A pictorial description of the problem is given in Figure 2.15. The traction is prescribed on the left boundary (i.e., $\mathbf{t}^P(\mathbf{x}) = -p_{\text{inj}} \hat{\mathbf{n}}(\mathbf{x})$ on Γ_1^t) and on the middle of the right boundary (i.e., $\mathbf{t}^P(\mathbf{x}) = -p_{\text{atm}} \hat{\mathbf{n}}(\mathbf{x})$ on Γ_2^t). Elsewhere, homogeneous velocity boundary condition is enforced. Due to the prescription of the traction on a part of the boundary, this problem is incompatible

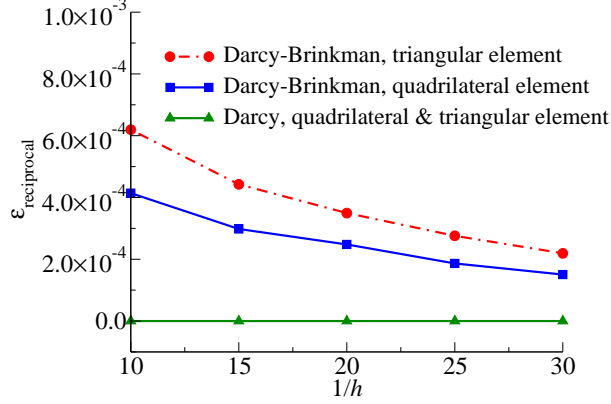


Figure 2.14: Pressure slab problem: The figure shows the variation of $\varepsilon_{\text{reciprocal}}$ with mesh refinement for Darcy and Darcy-Brinkman equations using quadrilateral and triangular grids. The parameters in this problem are provided in Table 2.5.

Table 2.6: Pressure driven problem: Non-dimensional parameters used in the problem.

Parameter	Value
α	1
μ	1 and 0.001
ρ	1
p_{inj}	5 and 7.5
p_{atm}	1
L	1

with the minimum dissipation theorem but is compatible with the reciprocal relation and the total mechanical power theorem. Herein, we present the results for the reciprocal relation. The non-dimensional parameters used in the numerical simulation are provided in Table 2.6. Figure 2.16 show the variation of the error in the reciprocal relation with mesh refinement for triangular and quadrilateral meshes. Since the problem has a singularity near the corners of the outlet (i.e., Γ_2^t), the convergence under uniform structured meshes is slow which improved by employing an adaptive mesh.

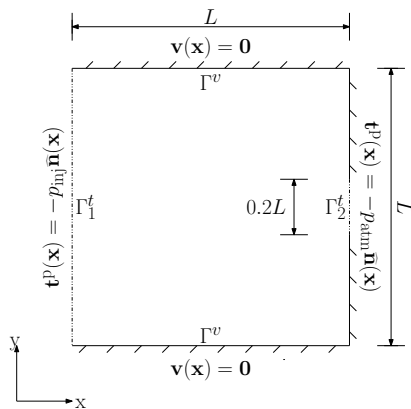


Figure 2.15: Pressure-driven problem: computational domain Ω is a square with $L = 1$. The traction is prescribed on the left side of the boundary and on the middle of right side.

2.4.6 Vorticity results

The maximum principle given by Theorem 2.3.8 can be used to assess the accuracy of numerical solutions to the Darcy-Brinkman equations by checking whether the non-negative maximum and non-positive minimum of the vorticity occur on the boundary. Figure 2.17 shows that the maximum principle is satisfied for various problems under the steady-state Darcy-Brinkman equations.

2.4.7 Synthetic reservoir data: Marmousi dataset

We will now solve an idealized reservoir problem using a popular synthetic dataset – the so-called (smooth) Marmousi dataset [Versteeg and Grau, 1990, Versteeg and Lailly, 1991, Versteeg, 1993, Klimes, 2014, Benamou, 2014]. The dataset provides spatially varying speed of sound on a 384×122 grid. We have assumed that the permeability scales linearly with the values provided by the dataset. This is just an arbitrary choice to generate a heterogeneous dataset for permeability. However, it should be noted that the conclusions that will be drawn here will be valid even if one uses another dataset for the permeability. Figure 2.18 shows the contours of Marmousi dataset.

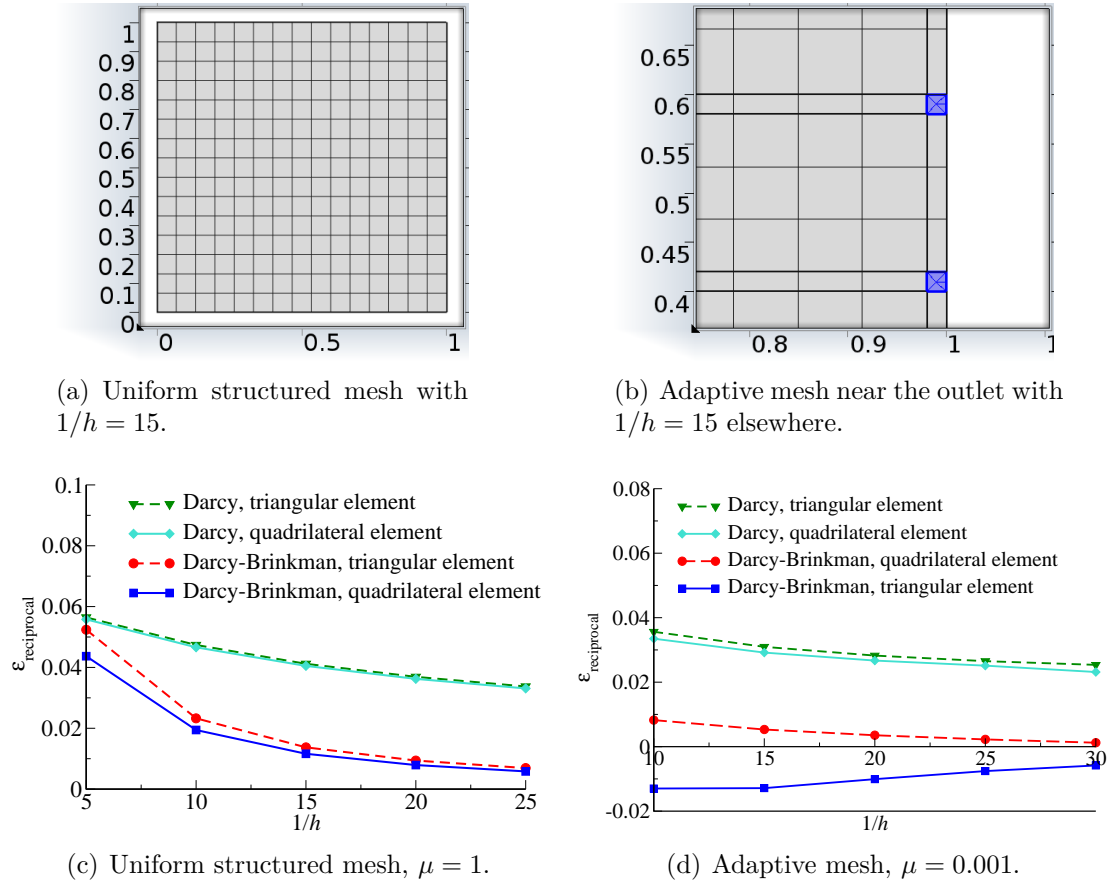
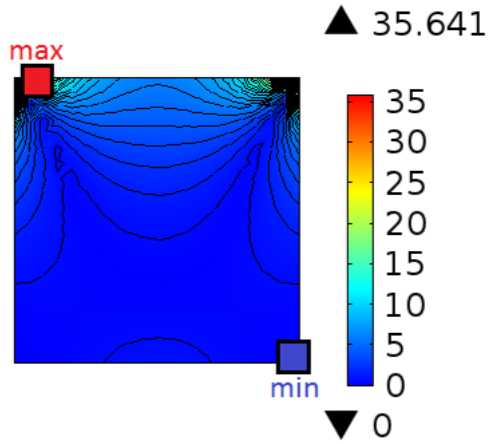
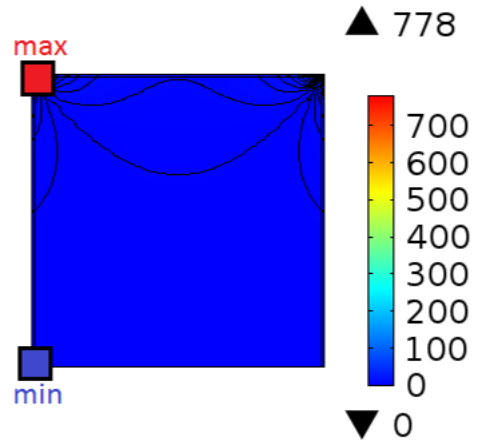


Figure 2.16: Pressure-driven problem: The top figures show the uniform structured mesh and the adaptive mesh near the corners of the outlet (i.e., Γ_2^t). The bottom figures show the variation of $\varepsilon_{\text{reciprocal}}$ with mesh refinement.

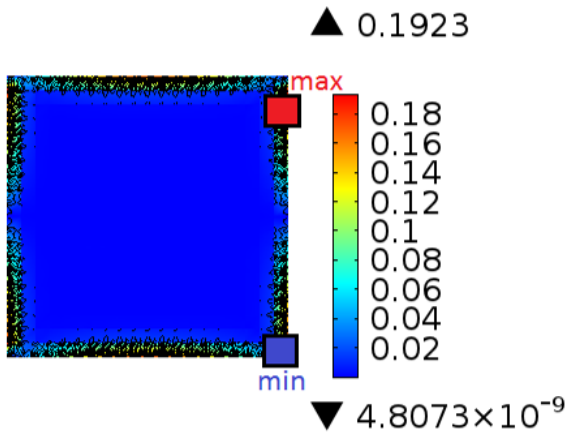
The boundary value problem of the reservoir is pictorially described in Figure 2.19. This computational domain has been employed in some recent works (e.g., [Nakshatrala and Rajagopal, 2011]). All these works have assumed homogeneous medium properties, and did not use a reservoir data like the Marmousi dataset. Moreover, these studies did not address the use of *a posteriori* techniques to assess numerical accuracy which is the main focus of the current paper. The parameters used in this problem are provided in Table 2.7. Figure 2.20 shows that the errors in the reciprocal relation are larger under uniform structured meshes than under adaptive meshes. This is due to the fact that uniform structured meshes suffer from pollution errors due to the singularity near the production well. The variation of



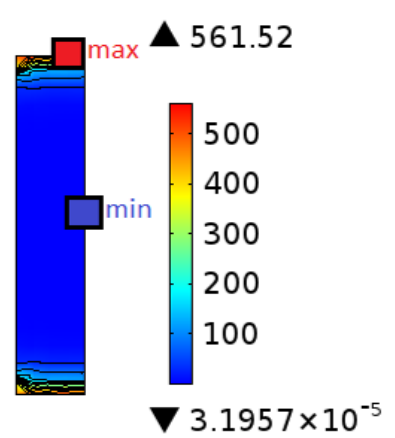
(a) Lid-driven cavity, regular mesh. $\omega_{max} = 35.641$ and $\omega_{min} = 0$.



(b) Lid-driven cavity, adaptive mesh. $\omega_{max} = 778$ and $\omega_{min} = 0$.



(c) Body force problem. $\omega_{max} = 0.1923$ and $\omega_{min} = 4.8073 \times 10^{-9}$.



(d) Slab problem. $\omega_{max} = 561.52$ and $\omega_{min} = 3.1957 \times 10^{-5}$.

Figure 2.17: The figure verifies the maximum principle for the vorticity for various two-dimensional problems under the Darcy-Brinkman model. The numerical results corroborate the theoretical predictions given in Theorem 2.3.8.

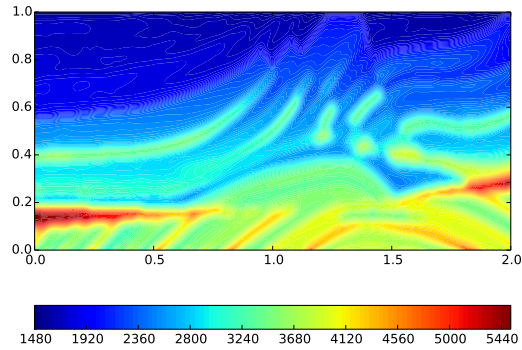


Figure 2.18: Synthetic reservoir problem: This figure shows the contours of (smooth) Marmousi dataset [Benamou, 2014]. It provides values on a 384×122 grid which scaled to our rectangular computational domain of $L = 2$ and $H = 1$.

Table 2.7: Synthetic reservoir problem: Non-dimensional parameters used in the problem.

Parameter	Value
μ	0.001
ρ	1
p_{inj}	5 and 7.5
p_{atm}	1
L	384
H	$384/2$
W	384×0.1
k	Marmousi dataset/ L^2

the error in the reciprocal relation with mesh refinement provides guidelines on how much refinement is required to obtain solution of some desired accuracy especially in those cases where there are no analytical solutions. Figure 2.21 shows the magnitude of the vorticity, and one can see from the figure that the maximum principle for the vorticity is satisfied.

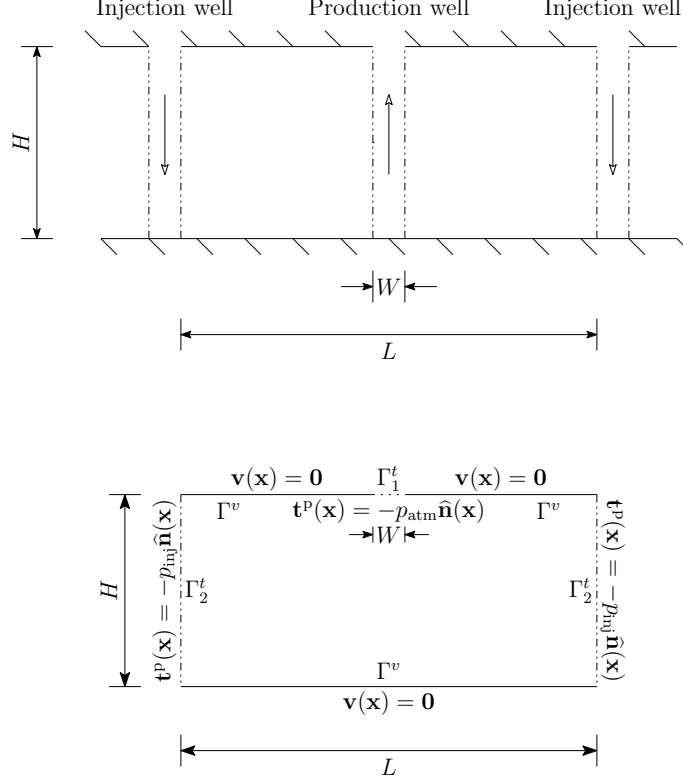


Figure 2.19: Synthetic reservoir problem: The domain of the problem is a rectangle of size $H \times L$. The injection pressure is prescribed on the left and right boundaries and the atmosphere pressure is prescribed on the middle of top side.

2.5 Transient case

2.5.1 Governing equations

Let us denote the time interval of interest by \mathcal{I} , and the time by $t \in \mathcal{I}$. The unsteady governing equations under the Darcy model take the following form:

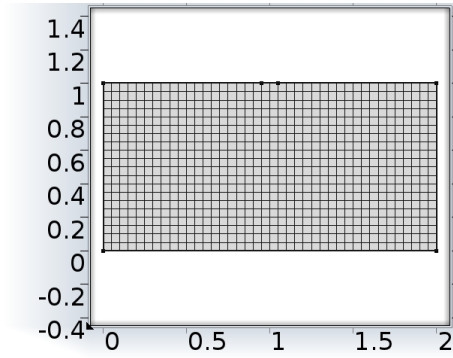
$$\rho \frac{\partial \mathbf{v}}{\partial t} + \alpha \mathbf{v} + \text{grad}[p] = \rho \mathbf{b}(\mathbf{x}, t) \quad \text{in } \Omega \times \mathcal{I}, \quad (2.5.1a)$$

$$\text{div}[\mathbf{v}] = 0 \quad \text{in } \Omega \times \mathcal{I}, \quad (2.5.1b)$$

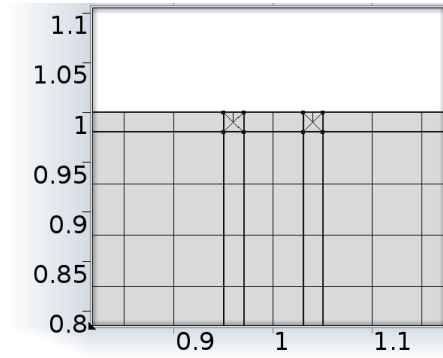
$$\mathbf{v}(\mathbf{x}, t) \cdot \hat{\mathbf{n}}(\mathbf{x}) = v_n(\mathbf{x}, t) \quad \text{on } \Gamma^v \times \mathcal{I}, \quad (2.5.1c)$$

$$p(\mathbf{x}, t) = p_0(\mathbf{x}, t) \quad \text{on } \Gamma^t \times \mathcal{I}, \quad \text{and} \quad (2.5.1d)$$

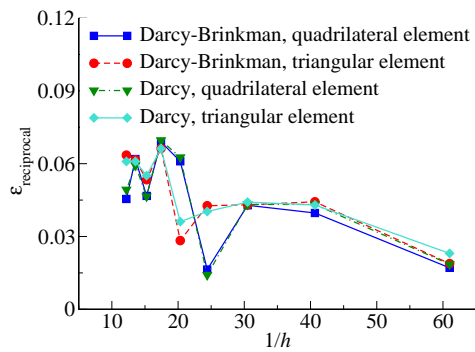
$$\mathbf{v}(\mathbf{x}, t = 0) = \mathbf{v}_0(\mathbf{x}) \quad \text{in } \Omega. \quad (2.5.1e)$$



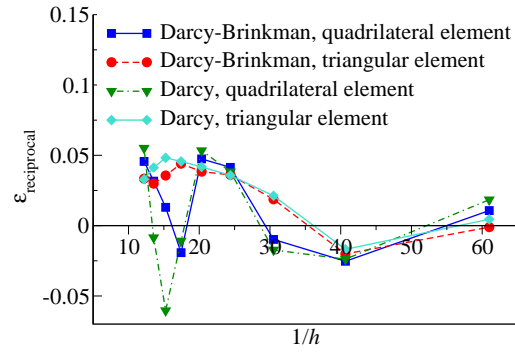
(a) Uniform structured mesh with $1/h = 20$.



(b) Adaptive mesh near the production well with $1/h = 20$ elsewhere.



(c) Variation of $\varepsilon_{\text{reciprocal}}$ under a hierarchy of uniform structured meshes.



(d) Variation of $\varepsilon_{\text{reciprocal}}$ under a hierarchy of adaptive meshes.

Figure 2.20: Synthetic reservoir problem: The figures show the variation of $\varepsilon_{\text{reciprocal}}$ with h for the Darcy and Darcy-Brinkman models using structured and adaptive meshes. The parameters in this problem are provided in Table 2.7.

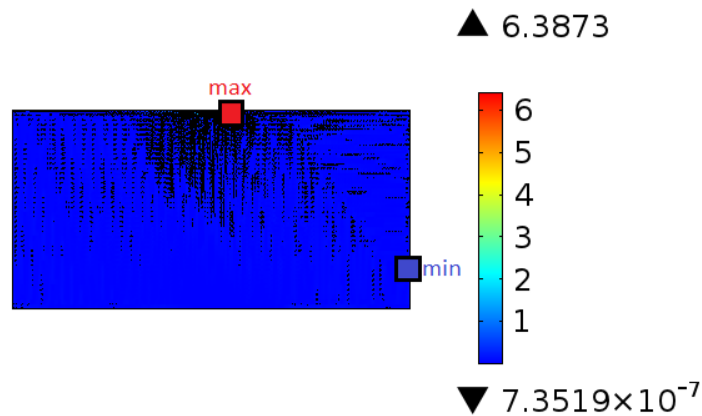


Figure 2.21: Synthetic reservoir problem: The figure shows the magnitude of vorticity for two-dimensional Darcy-Brinkman equations using quadrilateral elements. The parameters used in this problem are provided in Table 2.7.

Of course, the convective term $\text{grad}[\mathbf{v}]\mathbf{v}$ is neglected. We assume that the coefficient of viscosity of the fluid and the permeability of the porous solid to be constants, and hence the drag coefficient is constant. We further assume that the density is homogeneous, and the body force is assumed to be conservative. The unsteady Darcy-Brinkman equations can be written as

$$\rho \frac{\partial \mathbf{v}}{\partial t} + \alpha \mathbf{v} + \text{grad}[p] - \text{div}[2\mu \mathbf{D}] = \rho \mathbf{b}(\mathbf{x}, t) \quad \text{in } \Omega \times \mathcal{I}, \quad (2.5.2a)$$

$$\text{div}[\mathbf{v}] = 0 \quad \text{in } \Omega \times \mathcal{I}, \quad (2.5.2b)$$

$$\mathbf{v}(\mathbf{x}, t) = \mathbf{v}^p(\mathbf{x}, t) \quad \text{on } \Gamma^v \times \mathcal{I}, \quad (2.5.2c)$$

$$\mathbf{T}\hat{\mathbf{n}}(\mathbf{x}) = \mathbf{t}^p(\mathbf{x}, t) \quad \text{on } \Gamma^t \times \mathcal{I}, \text{ and} \quad (2.5.2d)$$

$$\mathbf{v}(\mathbf{x}, t = 0) = \mathbf{v}_0(\mathbf{x}) \quad \text{in } \Omega, \quad (2.5.2e)$$

where $\mathbf{v}^p(\mathbf{x}, t)$ is the prescribed velocity vector, and $\mathbf{t}^p(\mathbf{x}, t)$ is the prescribed traction.

2.5.2 Mathematical properties

Under unsteady Darcy equations, the vorticity satisfies the following equation:

$$\rho \frac{\partial \boldsymbol{\omega}}{\partial t} + \alpha \boldsymbol{\omega} = \mathbf{0}, \quad (2.5.3)$$

which is an ordinary differential equation at each spatial point. The solution takes the following form:

$$\boldsymbol{\omega}(\mathbf{x}, t) = \boldsymbol{\omega}_0(\mathbf{x}) \exp \left[-\frac{\alpha t}{\rho} \right]. \quad (2.5.4)$$

This means that the decay of vorticity should be exponential. One can check whether the numerical solutions exhibit this trend by plotting in log scale the each component of the vorticity with respect to time should, and this should be a straight line with slope $-\alpha/\rho$. If this trend is not satisfied for a given mesh and given time-step, does

Table 2.8: Pressure slab problem: Initial condition used in the problem.

Parameter	Value
p	p_{atm}
$v_x = v_y$	$\sin(\pi x/W) \sin(\pi y/L)$

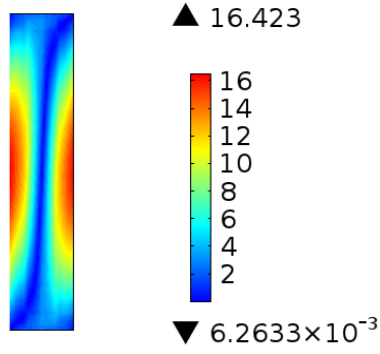
refining the grid spacing and the time-step improve the trend? Of course, one can check whether the vorticity goes to zero for large times. The vorticity under unsteady Darcy-Brinkman equations satisfies the following equation:

$$\rho \frac{\partial \omega}{\partial t} + \alpha \omega - \mu \Delta \omega = \mathbf{0} \quad \text{in } \Omega \times \mathcal{I}, \quad (2.5.5)$$

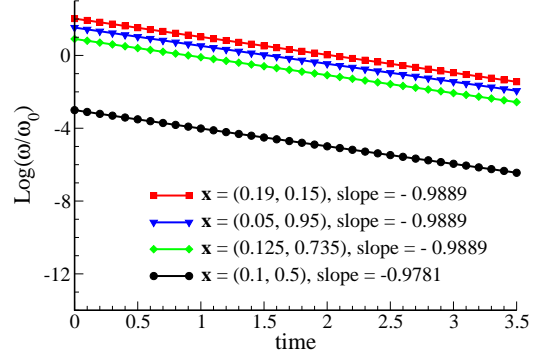
where Δ is the Laplacian operator. The above equation is a homogeneous linear parabolic partial differential equation, which is known to satisfy a maximum principle [Pao, 1993]. This implies that both the maximum and the minimum will occur either in the initial condition or on the boundary. One can check whether numerical solutions satisfy the aforementioned maximum principle. Also, whether refining the grid spacing and time-steps affect the performance of numerical solutions with respect to this metric. One can devise any test problem as long as the following assumptions are met: (i) μ is constant, (ii) permeability is homogeneous, and (iii) the body force is conservative.

2.5.3 Representative numerical results

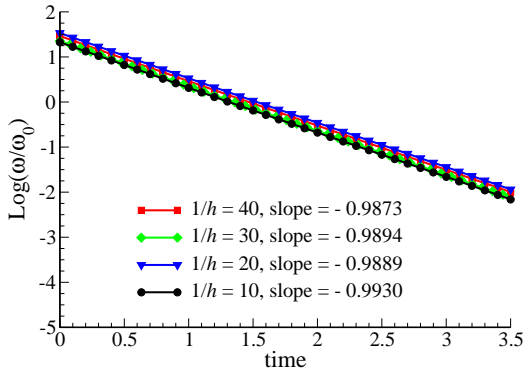
The theoretical results presented in this section are corroborated numerically in Figures 2.22–2.23. The vorticity results for the pressure slab problem under the transient Darcy model are provided in Figures 2.22. (Recall that Figure 2.13 provided a pictorial description of the pressure slab problem.) The non-dimensional parameters used in the numerical simulation are presented in Table 2.5, and the initial condition is provided in Table 2.8. Figure 2.22 shows that $\log(\frac{\omega}{\omega_0})$ is a straight line with slope



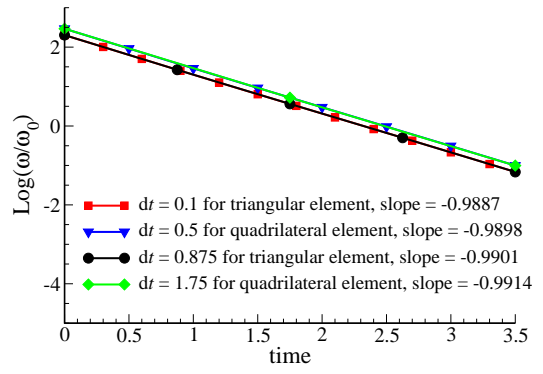
(a) Initial vorticity for quadrilateral element size of $1/h = 20$.



(b) Quadrilateral element size of $1/h = 20$ for $dt = 0.01$.



(c) Mesh refinement for quadrilateral elements, at $x = (0.05, 0.95)$ and $dt = 0.01$.



(d) Time refinement for $1/h = 20$ at $x = (0.15, 0.35)$.

Figure 2.22: Pressure slab problem: The figure verifies the theoretical results for the vorticity under transient Darcy equations. The results show that the slope of $\log(\frac{\omega}{\omega_0})$ for various spatial points in the domain are close to $-\frac{\alpha}{\rho} = -1$.

equal to $\frac{\alpha}{\rho}$ under the mesh and time refinements for various spatial points in the solution of the transient Darcy equations (for the current problem $\frac{\alpha}{\rho} = -1$). Figure 2.23 verifies the maximum principle for vorticity for various test problems under transient Darcy-Brinkman equations. In all the cases, the non-negative maximum and non-positive minimum of the vorticity occur on the boundary, which agree with the mathematical theory presented above.

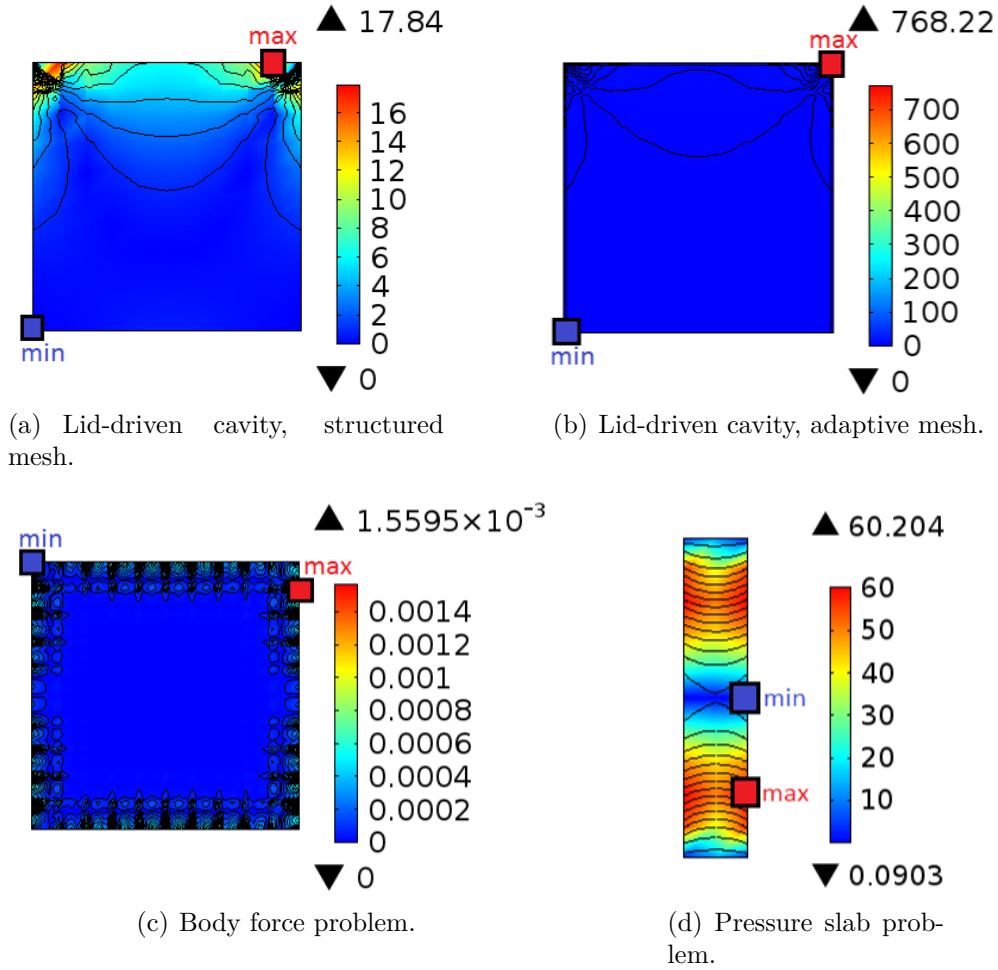


Figure 2.23: The figure verifies the maximum principle for the vorticity under transient Darcy-Brinkman equations for various two-dimensional problems. The numerical results satisfy the maximum principle for all the test problems.

2.6 Concluding remarks

We presented various test problems that can serve as benchmark problems for verifying numerical implementation of solvers for the Darcy and Darcy-Brinkman models. We also presented four important properties (minimum dissipation theorem, minimum total mechanical power, reciprocal relation, and maximum principle for vorticity) that the solutions under the Darcy and the Darcy-Brinkman models satisfy. These properties can be effectively used to assess the accuracy of numerical solutions. An attractive feature is that these properties can be verified for any given problem

(i.e., needed not be one of the benchmark problems), and for any computational domain. For example, if the problem involves prescribing velocity boundary condition on the entire boundary, then one plots the dissipation with respect to mesh refinement.

Some of the main conclusions are:

- (a) If the numerical formulation is converging, the dissipation, total mechanical power, and reciprocal relation should decrease with mesh refinement. If this does not occur, one needs to suspect that there are singularities in the solutions or that the numerical formulation does not perform well with respect to the local mass balance property.
- (b) It has been shown that the minimum dissipation theorem can be utilized to identify pollution errors in numerical solutions. The theorem can also be used to assess whether a given type of mesh will be able to resolve singularities in the solution. This can be assessed by creating a series of hierarchical meshes and plotting the dissipation with respect to characteristic mesh size. A given type of mesh will resolve singularities in the solution and will not be affected by pollution errors if the total dissipation decreases uniformly and reaches a plateau with a hierarchical mesh refinement.
- (c) The non-negative maximum vorticity and the non-positive minimum vorticity under Darcy-Brinkman equations with homogeneous isotropic medium properties should occur on the boundary.

The proposed *a posteriori* techniques can be invaluable additions to the usual repertoire of methods for verification of code – the method of exact solutions (MES) and the method of manufactured solutions (MMS).

Chapter 3

VISCOUS FINGERING AND MIXING FOR DOUBLE DIFFUSION MODEL: EFFECT OF TEMPERATURE AND NUMERICAL STABILIZATION

Reason has always existed, but not always in a reasonable form.

Karl Marx

3.1 Introduction to viscous fingering phenomena

Hydrodynamical instabilities may occur in flows if there is a change in mobility ratios of the fluids. Adverse mobility ratio is commonly related to variation in physical properties such as viscosity or/and density of at least two fluids. Viscous fingering (VF) instability, so-called Saffman-Taylor instability [Saffman and Taylor, 1958], can be observed when the viscosity of fluids alter. Viscosity contrast ratio [Homsy, 1987] and chemical reaction [Hejazi et al., 2010] can influence the viscosity and form the VF. Instability in two miscible fluids, introduces disorder in the flow field and velocity gradient dictates the fingering dynamics and mechanisms. Particularly, the VF occurs in porous media or Hele-Shaw cell, when a high viscous fluid is displaced by a lower

viscous fluid [Saffman and Taylor, 1958]. It is known as classical stable VF [Mishra et al., 2010, 2012]. Due to faster movement of low viscous fluid, any small disturbance or perturbation to the interface of miscible fluids generates finger structures. The perturbation can be induced by heterogeneity in the material properties such as permeability and diffusivity/dispersion or due to non-linearity in the problem parameters like concentration of transports and chemical reactions. When the instability is induced to the interface of the fluids, the less viscous flow penetrates into the more viscous one and grows in the form of fingering. This is a viscosity difference driven mechanism that occurs during diffusive mixing between the miscible fluids [Homsy, 1987].

Immiscible systems are also affected by fingering instabilities. For immiscible fluids, variation of surface tension at the fluids interface can cause the fingering patterns. So, in this case, the instability is governed by the capillary number [Fernandez and Homsy, 2003]. Similarly, instability on the interface of fluids with different densities maybe observed when the fluid with higher density is located on top of the lighter fluid in the gravity field. This has been referred to Rayleigh-Taylor instability [Taylor, 1950, Lewis, 1950] or density fingering [Almarcha et al., 2013]. In this case, the density difference across the interface is the driving mechanism of the instability.

VF and miscible displacement in porous media have been found in wide variety range of industrial, environmental, chemical, and biological applications. Enhanced oil recovery (EOR) and geological carbon-dioxide sequestration [Chen and Meiburg, 1998], combustion [Zik et al., 1998], electrochemical process [de Bruyn, 1995], and aquifers and chromatography [Maes et al., 2010] are some studied examples. The idea of VF phenomena is for [Hill, 1952]. So, the theoretical investigation dates back to more than half-century ago (see [Saffman and Taylor, 1958, Heller, 1966, Raghavan and Marsden, 1971, Saffman, 1986, Riaz and Tchelepi, 2004], and [Hejazi et al.,

2010] and references therein). Numerical simulation has been also utilized to gain insight into the impact of material and physical properties including viscosity, density, permeability, and diffusivity/dispersion [Tan and Homsy, 1988, 1992, Zimmerman and Homsy, 1992a,b, Chen and Meiburg, 1998, Riaz and Tchelepi, 2006]. Moreover, several numerical methods are developed to get deeper qualitative and quantitative understanding of the phenomena (see [Scovazzi et al., 2013] and references therein).

In addition to composition changes, viscosity in fluids can alter due to temperature contrast, which is interpreted as double diffusive (DD) effects. In this case, VF should be studied by considering miscible displacement between fluids in non-isothermal condition [Chan and Liang, 1997, Pritchard, 2004, 2009, Nagatsu et al., 2009, Islam and Azaiez, 2010a,b]. In practical cases like enhanced oil recovery, viscosity changes in displacement between oil and hot water are observed due to coupled thermal and species effects [Sheorey and Muralidhar, 2003]. Moreover, as mentioned before, the classical stable situation for VF is when a low viscous fluid displacing a high viscous one. However, as heat diffuses faster than mass, DD effects can also influence the stability characteristics of VF. It should be noted that the DD effects are not restricted to temperature influences. It may occur due to different solutes or mass components which diffuse at different rates [Mishra et al., 2010]. References [Trevelyan et al., 2011, C-Landeira et al., 2013, Almarcha et al., 2013] studied DD effects in Rayleigh-Taylor instability. Also, investigation of VF and DD effects for incompressible Navier-Stokes flow (not Darcy or porous media flows) is performed by [Mishra et al., 2012].

The rest of this chapter is organized as follows. Section 3.2 presents the governing equations, which are coupled flow, transport, and thermal equations. Section 3.3 reviews finite element method, stabilized formulations, and mathematical properties for numerical simulation. A reduced order model for mixing is presented in Section 3.4. In Section 3.5, we present several qualitative and quantitative numerical results

to illustrate the effect of temperature on VF and mixing. Section 3.6 provides results regarding numerical stabilization. Finally, conclusions are drawn in Section 3.7.

3.2 Governing equations: Coupled flow, transport, and thermal processes

In this section, we present the governing equations to model the dynamics of the VF phenomenon. A mathematical model for VF will be a system of coupled partial differential equations, which are either elliptic or parabolic. Herein, we consider an incompressible single-phase miscible flow with two components. The flow is governed by Darcy equations, which describe the flow of an incompressible fluid in a rigid porous media. We consider temperature effects and include thermal equations, which stem from the balance of energy. The governing equations for transport and thermal subproblems are transient in nature, while the governing equations for the flow subproblem are quasi-static. There is a two-way coupling in the current model. The viscosity of fluid is a nonlinear function of the concentrations c_i and temperature θ . That is, $\mu = \mu(c_i, \theta)$ where μ is viscosity. The transport and thermal equations will in turn involve the velocity of fluid. Due to the complexity of the governing equations, one need to solve them numerically.

Let $\Omega \subset \mathbb{R}^d$ be an open bounded domain, where “ d ” is the number of spatial dimensions. Let $\partial\Omega := \bar{\Omega} - \Omega$ denote the boundary of the domain, where $\bar{\Omega}$ denotes the set closure of Ω . A spatial point is denoted by $\mathbf{x} \in \bar{\Omega}$. The time is denoted by $t \in]0, \mathcal{I}[$, where \mathcal{I} denotes the total time of interest. The gradient and divergence operators with respect to \mathbf{x} are, respectively, denoted by $\text{grad}[\cdot]$ and $\text{div}[\cdot]$. The governing equations for the *flow* subproblem, which is governed by Darcy equations, are written as

$$\mu(c_i, \theta) \mathbf{K}^{-1}(\mathbf{x}) \mathbf{v}(\mathbf{x}, t) + \text{grad}[p(\mathbf{x}, t)] = \rho \mathbf{b}(\mathbf{x}, t) \quad \text{in } \Omega \times]0, \mathcal{I}[, \quad (3.2.1a)$$

$$\frac{\partial \rho}{\partial t} + \text{div}[\rho \mathbf{v}(\mathbf{x}, t)] = \varphi(\mathbf{x}, t) \quad \text{in } \Omega \times]0, \mathcal{I}[, \quad (3.2.1b)$$

$$p(\mathbf{x}, t) = p_0(\mathbf{x}, t) \quad \text{on } \Gamma^p \times]0, \mathcal{I}[, \quad \text{and} \quad (3.2.1c)$$

$$\mathbf{v}(\mathbf{x}, t) \bullet \hat{\mathbf{n}}(\mathbf{x}) = v_n(\mathbf{x}, t) \quad \text{on } \Gamma^v \times]0, \mathcal{I}[, \quad (3.2.1d)$$

where ρ is the density of the fluid, which is assumed to be constant. $\mathbf{v}(\mathbf{x}, t)$ is the velocity vector field. The pressure field is denoted by $p(\mathbf{x}, t)$, and the body force denoted by $\mathbf{b}(\mathbf{x}, t)$. $\mathbf{K}(\mathbf{x})$ is the permeability tensor and, $\varphi(\mathbf{x}, t)$ denotes the mass production. $p_0(\mathbf{x}, t)$ is the prescribed pressure on the boundary, and $v_n(\mathbf{x}, t)$ is the prescribed normal component of the velocity vector field on the boundary. Γ^p and Γ^v are, respectively, the boundaries of the domain on which the pressure and normal component of the velocity are prescribed. It is assumed that the velocity and its gradient are small so that the inertial effects and consequently the convective term can be neglected in the balance of linear momentum.

The *transport* of chemical species is modeled using advection-diffusion-reaction (ADR) equations, which can be written as

$$\frac{\partial c_i}{\partial t} + \text{div}[\mathbf{v}c_i - \mathbf{D}_i(\mathbf{x}) \text{grad}[c_i]] = f_i + r_i(\mathbf{x}, t, c_1, \dots, c_n) \quad \text{in } \Omega \times]0, \mathcal{I}[, \quad (3.2.2a)$$

$$c_i(\mathbf{x}, t) = c_i^p(\mathbf{x}, t) \quad \text{on } \Gamma_i^c \times]0, \mathcal{I}[, \quad (3.2.2b)$$

$$(\mathbf{v}(\mathbf{x}, t)c_i(\mathbf{x}, t) - \mathbf{D}_i(\mathbf{x}) \text{grad}[c_i(\mathbf{x}, t)]) \bullet \hat{\mathbf{n}}(\mathbf{x}) = h_i^p(\mathbf{x}, t) \quad \text{on } \Gamma_i^h \times]0, \mathcal{I}[, \quad \text{and} \quad (3.2.2c)$$

$$c_i(\mathbf{x}, t = 0) = c_i^0(\mathbf{x}) \quad \text{in } \Omega, \quad (3.2.2d)$$

where $c_i(\mathbf{x}, t)$ is the molar concentration of the i -th chemical species ($i = 1, \dots, n$), and $\mathbf{D}_i(\mathbf{x})$ is the corresponding diffusivity tensor. $f_i(\mathbf{x}, t)$ and $r_i(\mathbf{x}, t, c_1, \dots, c_n)$ are, respectively, the non-reactive and reactive components of the volumetric source. $c_i^0(\mathbf{x})$

is the initial condition, $c_i^p(\mathbf{x}, t)$ is the prescribed concentration on the boundary and $h_i^p(\mathbf{x}, t)$ is the prescribed flux on the boundary for the i -th constituent. Γ_i^c and Γ_i^h , respectively, denote the Dirichlet and Neumann parts of the boundaries for the transport subproblem. As we mentioned before, the model contains two components ($n = 2$). Since, our ADR equations are in mass fraction form, we will have $c_1 + c_2 = 1$. So, in the remaining of the paper we only solve the ADR model for the solvent c and one simply can derive the solute value which is $1 - c$.

The governing equations for the *thermal* subproblem can be written as

$$\frac{\partial \theta}{\partial t} + \text{div}[\mathbf{v}(\mathbf{x}, t)\theta(\mathbf{x}, t) - \varkappa(\mathbf{x}) \text{grad}[\theta]] = g + q(\mathbf{x}, t, \theta) \quad \text{in } \Omega \times]0, \mathcal{I}[, \quad (3.2.3a)$$

$$\theta(\mathbf{x}, t) = \theta^p(\mathbf{x}, t) \quad \text{on } \Gamma^\theta \times]0, \mathcal{I}[, \quad (3.2.3b)$$

$$(\mathbf{v}\theta - \varkappa \text{grad}[\theta]) \bullet \hat{\mathbf{n}}(\mathbf{x}) = s^p(\mathbf{x}, t) \quad \text{on } \Gamma^s \times]0, \mathcal{I}[, \quad \text{and} \quad (3.2.3c)$$

$$\theta(\mathbf{x}, t = 0) = \theta^0(\mathbf{x}) \quad \text{in } \Omega, \quad (3.2.3d)$$

where $\theta(\mathbf{x}, t)$ is the temperature and $\varkappa(\mathbf{x})$ is the thermal diffusivity tensor. $g(\mathbf{x}, t)$ and $q(\mathbf{x}, t, \theta)$ are, respectively, the non-thermal and thermal volumetric source. $\theta^0(\mathbf{x})$ is the temperature initial condition. $\theta^p(\mathbf{x}, t)$ and $s^p(\mathbf{x}, t)$ are, respectively, the prescribed temperature and the prescribed heat flux on the boundary. Γ^θ and Γ^s denote, respectively, the Dirichlet and Neumann parts of the boundary for the thermal subproblem.

We assume that the permeability $\mathbf{K}_i(\mathbf{x})$, mass diffusivity $\mathbf{D}_i(\mathbf{x}, t)$, and thermal diffusivity $\varkappa(\mathbf{x}, t)$ tensors to be isotropic, unless mentioned otherwise. Thus, we can write $\mathbf{K} = k\mathbf{I}$, $\mathbf{D} = d_m\mathbf{I}$ and $\varkappa = \kappa_\theta\mathbf{I}$.

3.3 Computational framework: Mixed and stabilized finite element formulations

The simplest model to solve VF numerically is coupled flow and advection-dominated AD equations. The classical formulations for numerical simulation of VF, such as high order finite difference and Fourier spectral methods, for high value of mobility ratio and Péclet number are numerically unstable [Islam and Azaiez, 2007, Jha et al., 2011]. Hence, we resort to finite element method (FEM) to simulate coupled flow-transport-thermal model.

3.3.1 Mixed two-field weak formulation for Darcy equations

The following function spaces will be used for the Darcy model:

$$\mathcal{P} := \left\{ p(\mathbf{x}, t) \in H^1(\Omega) \mid p(\mathbf{x}, t) = p_0(\mathbf{x}, t) \text{ on } \Gamma^p \times]0, \mathcal{I}[\right\}, \quad (3.3.1a)$$

$$\mathcal{Q} := \left\{ q(\mathbf{x}) \in H^1(\Omega) \mid q(\mathbf{x}) = 0 \text{ on } \Gamma^p \right\}, \quad (3.3.1b)$$

$$\mathcal{V} := \left\{ \mathbf{v}(\mathbf{x}, t) \in (L_2(\Omega))^{nd} \mid \operatorname{div}[\mathbf{v}] \in L_2(\Omega), \mathbf{v}(\mathbf{x}, t) \bullet \hat{\mathbf{n}}(\mathbf{x}) = v_n(\mathbf{x}, t) \text{ on } \Gamma^v \times]0, \mathcal{I}[\right\}, \text{ and} \quad (3.3.1c)$$

$$\mathcal{U} := \left\{ \mathbf{u}(\mathbf{x}) \in (L_2(\Omega))^{nd} \mid \operatorname{div}[\mathbf{u}] \in L_2(\Omega), \mathbf{u}(\mathbf{x}) \bullet \hat{\mathbf{n}}(\mathbf{x}) = 0 \text{ on } \Gamma^v \right\}, \quad (3.3.1d)$$

where $H^1(\Omega)$ is a standard Sobolev space [Evans, 1998]. Also, the standard L_2 inner-product for given two fields $a(\mathbf{x}, t)$ and $b(\mathbf{x}, t)$ over a set \mathcal{B} is defined as

$$(a; b)_{\mathcal{B}} = \int_{\mathcal{B}} a(\mathbf{x}) \bullet b(\mathbf{x}) \, d\mathcal{B}. \quad (3.3.2)$$

The subscript on the inner-product will be dropped if $\mathcal{B} = \Omega$. The resulting mixed

weak form for the equations (3.2.1a)–(3.2.1d) can be written as

$$(\mathbf{u}; \mu \mathbf{K}^{-1} \mathbf{v}) - (\operatorname{div}[\mathbf{u}]; p) - (q; \operatorname{div}[\mathbf{v}]) = (\mathbf{u}; \rho \mathbf{b}) + (\mathbf{u} \bullet \hat{\mathbf{n}}; p_0)_{\Gamma^p}. \quad (3.3.3)$$

3.3.2 Stabilized formulations for ADR equations

In standard single-field Galerkin finite element formulation for ADR equations, in order to obtain accurate numerical solutions and avoid spurious node-to-node oscillations, element Péclet number has to be smaller than unity [Gresho and Sani, 2000]. When advection process is predominant and the element Péclet number is greater than unity the steep gradients due to the presence of characteristic layers such as interior and/or boundary layers in the solution may not be resolved by computational grid. One way to come up with this numerical problem and achieve smaller Péclet number for elements is mesh refinement. However, in some cases, employing such a fine mesh make the cases computationally so expensive. Hence, we utilize numerical stabilizers which are alternative methods of Galerkin formulation for advection-dominated problems [Augustin et al., 2011].

Remark 3.3.1. *For completeness and future reference, it should be noted that numerical instabilities or spurious node-to-node oscillations in the solution based on a certain numerical formulation should not be confused with the (physically meaningful) instability behaviors which are induced mathematically or physically. These two are entirely different.*

Herein, we shall utilize Streamline Upwind Petrov-Galerkin (SUPG) formulation [Brooks and Hughes, 1982] and its modifications called SOLD (Spurious Oscillations at Layers Diminishing) [John and Knobloch, 2007], which are common stabilized numerical formulations for ADR model given by equations (3.2.2a)–(3.2.2d). Before we present these stabilized weak formulations, we will introduce the following function

spaces:

$$\mathcal{C}_i^t := \left\{ c_i(\mathbf{x}, t) \in H^1(\Omega) \mid c_i(\mathbf{x}, t) = c_i^p(\mathbf{x}, t) \text{ on } \Gamma_i^c \times]0, \mathcal{I}[\right\} \quad \text{and} \quad (3.3.4a)$$

$$\mathcal{W}_i := \left\{ w_i(\mathbf{x}) \in H^1(\Omega) \mid w_i(\mathbf{x}) = 0 \text{ on } \Gamma_i^c \right\}. \quad (3.3.4b)$$

3.3.2.1 SUPG formulation

Find $c_i(\mathbf{x}, t) \in \mathcal{C}_i^t$ such that

$$\begin{aligned} & (w_i; \frac{\partial c_i}{\partial t}) + (\text{grad}[w_i] \bullet \mathbf{v}; c_i) + (\text{grad}[w_i]; \mathbf{D}(\mathbf{x}, t) \text{grad}[c_i]) \\ & + \sum_{e=1}^{Nele} \left(\tau \mathbf{v} \bullet \text{grad}[w_i]; \frac{\partial c_i}{\partial t} + \text{div} [\mathbf{v} c_i - \mathbf{D}(\mathbf{x}, t) \text{grad}[c_i]] - f_i - r_i \right)_{\Omega_e} \\ & = (w_i; f_i) + (w_i; h_i^p)_{\Gamma_i^h} \quad \forall w_i(\mathbf{x}) \in \mathcal{W}_i, \end{aligned} \quad (3.3.5)$$

where $Nele$ is the total number of mesh elements and $\bar{\Omega} = \bigcup_{e=1}^{Nele} \bar{\Omega}^e$. The superposed bar denotes the set closure. The boundary of Ω^e is denoted as $\partial\Omega^e := \bar{\Omega}^e - \Omega^e$. τ is the stabilization parameter under the SUPG formulation. Herein, we shall use the stabilization parameter proposed by [John and Knobloch, 2007] as

$$\tau(\mathbf{v}) = \frac{h_{\Omega_e}}{2\|\mathbf{v}\|} \xi_0(\mathbb{P}e_h) \quad \text{and} \quad \xi_0(\chi) = \coth(\chi) - \frac{1}{\chi}, \quad (3.3.6)$$

where h_{Ω_e} is the maximum element length, ξ_0 is known as the upwind function, $\mathbb{P}e_h = \frac{h_{\Omega_e} \|\mathbf{v}\|}{2\lambda_{\min}}$ is the local (element) Péclet number, and λ_{\min} denotes the isotropic diffusion (d_m) or minimum eigenvalue of the anisotropic diffusivity.

3.3.2.2 SOLD isotropic artificial diffusion formulation

To diminish the oscillations arising in the solution of SUPG formulation, [Hughes et al., 1986b] proposed a modification to change the upwind direction in SUPG. They

added the following term to the left hand side of equation (3.3.5)

$$\sum_{e=1}^{Nele} \left(\tau_1 \mathbf{v}^{\parallel} \bullet \text{grad}[w_i]; \frac{\partial c_i}{\partial t} + \text{div} [\mathbf{v}c_i - \mathbf{D}(\mathbf{x}, t)\text{grad}[c_i]] - f_i - r_i \right)_{\Omega_e}, \quad (3.3.7)$$

where \mathbf{v}^{\parallel} corresponds to the direction in which oscillations in SUPG solutions are observed [John and Knobloch, 2007]

$$\mathbf{v}^{\parallel} = \begin{cases} \frac{(\mathbf{v} \bullet \text{grad}[c_i])\text{grad}[c_i]}{\|\text{grad}[c_i]\|^2} & \text{for } \text{grad}[c_i] \neq \mathbf{0} \\ \mathbf{0} & \text{for } \text{grad}[c_i] = \mathbf{0}, \end{cases}$$

and the stabilization parameter proposed by [Hughes et al., 1986b] is as

$$\tau_1 = \max\{0, \tau(\mathbf{v}^{\parallel}) - \tau(\mathbf{v})\}.$$

3.3.2.3 *SOLD crosswind artificial diffusion formulation*

An alternative modification for SUPG is proposed by [Johnson et al., 1987], in which they added artificial diffusion in the crosswind direction by considering \mathbf{v}^{\perp} as the projection onto the line or plane orthogonal to \mathbf{v}

$$\mathbf{v}^{\perp} = \begin{cases} \mathbf{I} - \frac{\mathbf{v} \otimes \mathbf{v}}{\|\mathbf{v}\|^2} & \text{for } \mathbf{v} \neq \mathbf{0} \\ \mathbf{0} & \text{for } \mathbf{v} = \mathbf{0}. \end{cases}$$

\mathbf{I} is the identity tensor. This leads to the additional term

$$\sum_{e=1}^{Nele} \left(\tau_2 \mathbf{v}^{\perp} \text{grad}[w_i]; \text{grad}[c_i] \right)_{\Omega_e}, \quad (3.3.8)$$

to the left hand side of equation (3.3.5), where

$$\tau_2 = \max\{0, \|\mathbf{v}\| h_{\Omega_e}^{2/3} - \lambda_{\min}\}.$$

For these stabilized finite element formulations, we shall present the stabilized solution to suppress node-to-node spurious oscillations and to satisfy maximum principle (and non-negative constraint).

It should be noted that for thermal subproblem, because of its advective-diffusive characteristic, we also employ SUPG stabilized formulation (equation (3.3.5)).

3.3.3 Violation of maximum principle and non-negative constraint

The initial boundary value problem given by equations (3.2.2a)–(3.2.2d) are parabolic type partial differential equations. It should be noted that such a model possesses several important mathematical properties including the maximum principle and non-negative constraint [Gilbarg and Trudinger, 2001, Protter and Weinberger, 2012]. These properties have been employed to assess numerical solution verification [Shabouei and Nakshatrala, 2016] and to propose non-negative numerical formulation [Mudunuru and Nakshatrala, 2016]. For example, physical quantities such as concentration and temperature naturally attain non-negative values. It has been shown that many popular numerical methods like finite element, finite volume, finite difference, and lattice Boltzmann violate the non-negative constraint for diffusion-type equations [Brezzi et al., 2005b, Potier, 2005, Liska and Shashkov, 2008, Pal et al., 2016, Nakshatrala et al., 2013, 2016b, Mudunuru et al., 2015, Karimi and Nakshatrala, 2016]. Obtaining physically meaningless solutions can make the solution inappropriate for scientific and engineering applications (See [Mudunuru and Nakshatrala, 2016] and references therein).

Mathematically, the maximum principle for the concentration under ADR model takes the following form: If $c(\mathbf{x}, t) \in C^2(\Omega) \cap C^0(\bar{\Omega})$, then the non-negative maximum and the non-positive minimum concentration at each time step occur on the boundary. That is,

$$\max_{\mathbf{x} \in \bar{\Omega}} [c(\mathbf{x}, t)] \leq \max \left[0, \max_{\mathbf{x} \in \partial\Omega} c(\mathbf{x}, t) \right] \quad \text{and} \quad (3.3.9a)$$

$$\min_{\mathbf{x} \in \bar{\Omega}} [c(\mathbf{x}, t)] \geq \min \left[0, \min_{\mathbf{x} \in \partial\Omega} c(\mathbf{x}, t) \right], \quad (3.3.9b)$$

where $C^2(\Omega)$ denotes the set of twice differentiable functions defined on Ω , and $C^0(\bar{\Omega})$ is the set of functions that are continuous to the boundary.

As mentioned before, herein, concentrations (c_1 and c_2) are in the form of mass fractions and always $c \leq 1$. The maximum principle on the other hand, implies that $c(\mathbf{x}, t) \geq 0$ in the entire domain, which is the non-negativity of the concentration field. So, herein, physical value for concentration is always $0 \leq c \leq 1$.

3.4 A reduced order model for mixing

Mixing enhancement in the absence of inertial effects and the lack of turbulence is limited. Moreover, for flow with low Reynolds numbers which occur in Hele-Shaw cells, porous media, and microfluidic devices, mixing efficiency can be altered by changing Pe , Le , R_c , and R_θ . Herein, we shall propose a reduced order model (ROM) for mixing in the coupled porous media flow, transport, and temperature problem. It should be noted that the proposed ROM in current study has some advantages over other models like which defined in [Jha et al., 2011]. First of all, current model is more general than the previous ones. It is applicable for double diffusion and multi-diffusion problems. Where, the previous models only proposed for single diffusion case. In addition, the model in [Jha et al., 2011] derived after several unnecessary assumptions including homogeneity of the VF process, neglecting the $\cos(\lambda)^2$ in which λ is angle between \mathbf{v} and \mathbf{g}_c at the interface, and taking the mean flow speed as a constant.

In a periodic field, it is easy to show that

$$\frac{d\langle c \rangle}{dt} = 0 \quad \text{and} \quad \frac{d\langle \theta \rangle}{dt} = 0, \quad (3.4.1)$$

in which $\langle \cdot \rangle$ is the spatial averaging operator over the domain volume. For instance, $\langle c \rangle$ is the spatial mean concentration in the domain. For convenience, let us define the following quantities:

$$\mathbf{g}_c := \text{grad}[c] \quad \text{and} \quad \mathbf{g}_\theta := \text{grad}[\theta]. \quad (3.4.2)$$

We shall introduce the following scalar dissipation functions:

$$\varepsilon_c = \frac{1}{\mathbb{P}_e} \langle \|\mathbf{g}_c\|^2 \rangle \quad \text{and} \quad \varepsilon_\theta = \frac{\mathbb{L}e}{\mathbb{P}_e} \langle \|\mathbf{g}_\theta\|^2 \rangle. \quad (3.4.3)$$

The variances of the concentration and temperature fields are, respectively, defined as

$$\sigma_c^2 = \langle c^2 \rangle - \langle c \rangle^2 \quad \text{and} \quad \sigma_\theta^2 = \langle \theta^2 \rangle - \langle \theta \rangle^2. \quad (3.4.4)$$

Using the above notation, one can write the evolution equations for the variances as

$$\frac{d\sigma_c^2}{dt} = -2\varepsilon_c \quad \text{and} \quad (3.4.5)$$

$$\frac{d\sigma_\theta^2}{dt} = -2\varepsilon_\theta. \quad (3.4.6)$$

Let us define the following two scalar functionals:

$$\varepsilon_{\mathbf{v}} := \left\langle \frac{\text{grad}[\mathbf{v}] \cdot \text{grad}[\mathbf{v}]}{\|\mathbf{v}\|^2} \right\rangle \quad \text{and} \quad (3.4.7)$$

$$\varepsilon_{c\theta} := \left\langle \|R_c \mathbf{g}_c + R_\theta \mathbf{g}_\theta\|^2 \right\rangle. \quad (3.4.8)$$

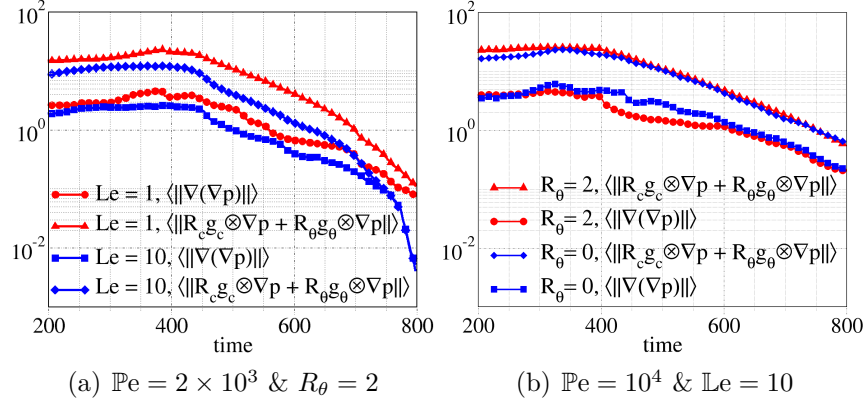


Figure 3.1: Mixing evolution: Time evolution for the equation (3.4.11) using numerical simulation for different Pe , Le , and R_θ . For all we keep $R_c = 2$. For each value of R_θ , the evolution in time for left hand side and right hand side of the equation (3.4.11) is very similar.

The first scalar pertains to the flow and the second scalar captures the combined effects of thermal and transport processes. From Darcy equations, we establish

$$\text{grad}[\mathbf{v}] \sim -\mu^{-1} (R_c \mathbf{g}_c \otimes \text{grad}[p] + R_\theta \mathbf{g}_\theta \otimes \text{grad}[p] + \text{grad}[\text{grad}[p]]). \quad (3.4.9)$$

By taking trace on the both sides of the above equation, and noting that $\text{div}[\mathbf{v}] = 0$, we obtain:

$$\text{trace} [R_c \mathbf{g}_c \otimes \text{grad}[p] + R_\theta \mathbf{g}_\theta \otimes \text{grad}[p]] = -\Delta p. \quad (3.4.10)$$

This motivates us to conjecture that

$$R_c \mathbf{g}_c \otimes \text{grad}[p] + R_\theta \mathbf{g}_\theta \otimes \text{grad}[p] \sim -\text{grad}[\text{grad}[p]], \quad (3.4.11)$$

which has been verified using numerical simulations on the Hele-Shaw problem. These results are provided in Figure 3.1. One can then obtain the following similarity:

$$\text{grad}[\mathbf{v}] \sim -\mu^{-1} (R_c \mathbf{g}_c + R_\theta \mathbf{g}_\theta) \otimes \text{grad}[p] = (R_c \mathbf{g}_c + R_\theta \mathbf{g}_\theta) \otimes \mathbf{v}. \quad (3.4.12)$$

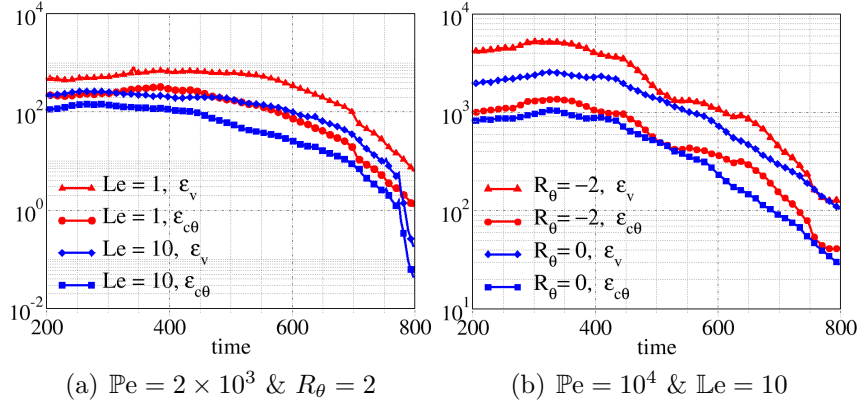


Figure 3.2: Mixing evolution: Evolution of ε_v and $\varepsilon_{c\theta}$ in time using numerical simulation for different Pe , Le , and R_θ . For all we keep $R_c = 2$. For each value of R_θ , the two variables evolve similarly which completely satisfies the equation (3.4.14).

Noting the property of the tensor product, one can obtain

$$\text{grad}[\mathbf{v}] \cdot \text{grad}[\mathbf{v}] \sim \|R_c \mathbf{g}_c + R_\theta \mathbf{g}_\theta\|^2 \|\mathbf{v}\|^2. \quad (3.4.13)$$

Using the definitions introduced in equations (3.4.7)–(3.4.8), one can obtain the similarity between the two scalar functions:

$$\varepsilon_v \sim \varepsilon_{c\theta}. \quad (3.4.14)$$

If the viscosity does not depend on the temperature (i.e., $R_\theta = 0$) then one can obtain the similarity relation given in [Jha et al., 2011] as a special case. That is,

$$\varepsilon_v \sim R_c^2 \text{Pe} \varepsilon_c \quad \text{when } R_\theta = 0. \quad (3.4.15)$$

Note that, there is a difference between the definition of ε_v employed in this paper versus the one defined in [Jha et al., 2011]. One can also obtain

$$\varepsilon_v \sim R_c^2 \text{Pe} \text{Le}^{-1} \varepsilon_\theta \quad \text{when } R_c = 0. \quad (3.4.16)$$

Figure 3.2 shows the evolution of $\varepsilon_{\mathbf{v}}$ and $\varepsilon_{c\theta}$ in time using numerical simulation for $\mathbb{Pe} = 10^4$, $\mathbb{Le} = 10$, and $R_c = 2$. For each value of R_θ , the two variables evolve similarly which completely satisfies the equation (3.4.14). It also conforms the proposed scaling in equation (3.4.8) and in consequence, the scaling in equations (3.4.15) and (3.4.16). In the general case, the scalar functionals, ε_c and ε_θ , are not sufficient to describe the viscous mixing due to the combined effects of temperature and concentration, as temperature and concentration fields are statistically correlated.

3.4.0.1 Concentration and temperature correlation

It should be noted that the concentration and temperature fields are correlated. This should be evident from the fact that the evolutions of both these fields (i.e., equations (3.2.2a) and (3.2.3a)) depends on the velocity \mathbf{v} . To systematically study the behavior of this correlation, we shall introduce the following field, which is a linear combination of temperature and concentration fields as

$$\chi := \sqrt{\mathbb{Pe}} \left(\frac{2\sqrt{\mathbb{Le}}R_c}{\mathbb{Le} + 1} c + \frac{R_\theta}{\sqrt{\mathbb{Le}}} \theta \right). \quad (3.4.17)$$

It is again easy to check that

$$\frac{d\langle\chi\rangle}{dt} = 0. \quad (3.4.18)$$

The evolution of variance of χ satisfies:

$$\frac{d\sigma_\chi^2}{dt} = \frac{d\langle\chi^2\rangle}{dt} = -2\varepsilon_{c\theta} + 2\mathbb{Pe}R_c^2 \left(\frac{\mathbb{Le} - 1}{\mathbb{Le} + 1} \right)^2 \varepsilon_c. \quad (3.4.19)$$

This shows that the evolution of the variance of χ changes its behavior depending on the Péclet number and Lewis number. $\varepsilon_{c\theta}$ is defined in equation (3.4.8). Figure 3.3 shows time evolution for the equation (3.4.19) using numerical simulation for

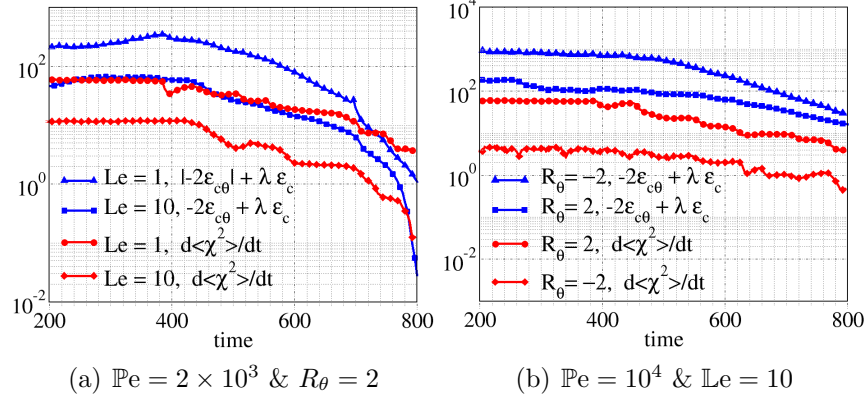


Figure 3.3: Mixing evolution: Time evolution for the equation (3.4.19) using numerical simulation for different $\mathbb{P}e$, $\mathbb{L}e$, and R_θ . For all we keep $R_c = 2$. The scaling expressions $\langle \chi^2 \rangle \sim t^2$ and $-2\varepsilon_{c\theta} + 2\mathbb{P}eR_c^2 \left(\frac{\mathbb{L}e-1}{\mathbb{L}e+1}\right)^2 \varepsilon_c \sim t$ are identified which satisfy the equation (3.4.19). Note that $\lambda = 2\mathbb{P}eR_c^2 \left(\frac{\mathbb{L}e-1}{\mathbb{L}e+1}\right)^2$, in the plot.

different $\mathbb{P}e$, $\mathbb{L}e$, and R_θ for Hele-Shaw problem (non-periodic field). For all cases we keep $R_c = 2$. The scaling expression $\langle \chi^2 \rangle \sim t^2$ is identified for correlation of c and θ .

3.4.0.2 Extension to the Hele-Shaw problem

We shall now show both mathematically and numerically that the above results are valid even for the Hele-Shaw problem even though the fields are not periodic. If nondimensional form of equation (3.2.2a) is multiplied by c we can derive evolution equation for ε_c as

$$\frac{1}{2} \left\langle \frac{\partial c^2}{\partial t} + \text{div} [\mathbf{v}c^2] \right\rangle - \frac{1}{\mathbb{P}e} \left\langle \text{div} [c \text{grad}[c]] - \|\text{grad}[c]\|^2 \right\rangle = 0, \quad (3.4.20)$$

in which

$$\left\langle \text{div} [\mathbf{v}c^2] \right\rangle = \int_{\Gamma_{\text{left}}} c^2 \mathbf{v} \cdot \hat{\mathbf{n}} d\Gamma = -c_{\text{inj}}^2 v_{\text{inj}} \quad \text{and} \quad (3.4.21)$$

$$\left\langle \text{div} [c \text{grad}[c]] \right\rangle = \int_{\Gamma_{\text{left}}} c \text{grad}[c] \cdot \hat{\mathbf{n}} d\Gamma = 0. \quad (3.4.22)$$

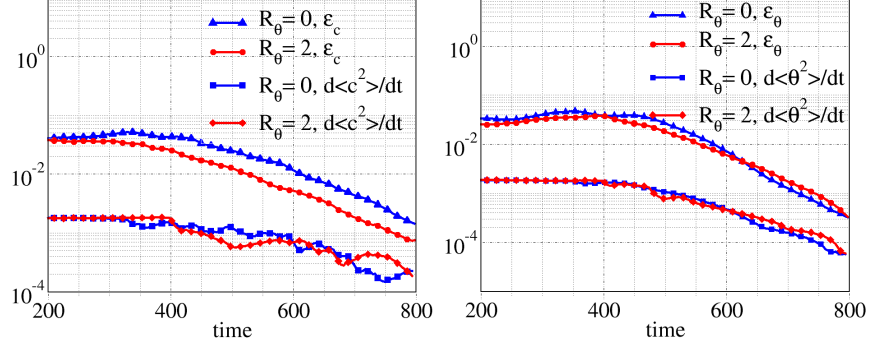


Figure 3.4: Mixing evolution: These figures show mixing parameters $\langle c^2 \rangle$, ε_c , $\langle \theta^2 \rangle$, and ε_θ vs. time for $\mathbb{P}e = 10^4$, $\mathbb{L}e = 10$ and $R_c = 2$. The scaling expression $\langle c^2 \rangle \sim t^2$ and $\langle \theta^2 \rangle \sim t^2$ are found. Moreover, scaling statement $\varepsilon_c \sim t$ and $\varepsilon_\theta \sim t$ are identified which satisfy equations (3.4.24) and (3.4.25).

Hence, we will have the following for equation (3.4.20):

$$\frac{1}{2} \frac{d}{dt} \langle c^2 \rangle - \frac{1}{2} c_{\text{inj}}^2 v_{\text{inj}} + \varepsilon_c = 0. \quad (3.4.23)$$

For the constant value of c_{inj} and v_{inj} , the concentration variance evolution for Hele-Shaw problem becomes

$$\frac{d}{dt} \langle c^2 \rangle \sim -2\varepsilon_c. \quad (3.4.24)$$

Note that, in Hele-Shaw problem, $\langle c \rangle$ is not constant and has a non-zero time evolution value.

Similarly, it is easy to derive temperature evolution for Hele-Shaw cell:

$$\frac{d}{dt} \langle \theta^2 \rangle \sim -2\varepsilon_\theta. \quad (3.4.25)$$

Figure 3.4 shows mixing parameters $\langle c^2 \rangle$, ε_c , $\langle \theta^2 \rangle$, and ε_θ vs. time for $\mathbb{P}e = 10^4$, $\mathbb{L}e = 10$ and $R_c = 2$. The scaling expression $\langle c^2 \rangle \sim t^2$ and $\langle \theta^2 \rangle \sim t^2$ are found. Moreover, scaling statements $\varepsilon_c \sim t$ and $\varepsilon_\theta \sim t$ are identified which satisfy equations (3.4.24) and (3.4.25).

3.5 Effect of temperature on viscous fingering

In this section we shall illustrate the results for coupled flow-transport-temperature system given by equations (3.2.1a)–(3.2.3d). Darcy flow model, equations (3.2.1a)–(3.2.1d), is an elliptic type equation that only needs appropriate Neumann or Dirichlet boundary conditions. Herein, normal velocity is the Neumann (flux) type boundary condition and pressure is the Dirichlet type. However, both boundary and initial conditions have to be forced for transport equations, (3.2.2a)–(3.2.2d), and heat equations, (3.2.3a)–(3.2.3d). In these two equations of parabolic character, concentration and temperature are enforced on the Dirichlet boundary and fluxes on the Neumann boundary. [Zimmerman and Homsy, 1992a] found that the mechanisms in two-dimensional (2-D) simulations of viscous fingering persist to those in three dimensions. They concluded that the 2-D simulations are sufficient to capture essential features of viscous fingering instability. Hence, herein we will solve a 2-D problem in horizontal porous media or Hele-Shaw cell (that is, two parallel plates separated by a thin gap) in which mass production in Darcy equation and volumetric sources in ADR and heat equations are zero. So, ADR equations reduce to AD equations. Study of Hele-Shaw cell can be useful for investigation of VF in micro-channel [Jha et al., 2013]. Pictorial description of the problem including boundary and initial conditions is provided in Figure 3.5. The computational domain is a $L_x \times L_y$ rectangle. On the left boundary the normal velocity v_x (in x -direction), concentration c^p , and temperature θ^p are enforced as the injected inflow. There is a small $w \times L_y$ rectangular region in the left to generate instabilities and to inject $(\mu_1(c, \theta), c, \theta)$. The disturbed fluid (μ_1) flows into the domain which contains the second fluid at rest (μ_2, c^0, θ^0) . The zero fluxes are prescribed on the top and bottom boundaries for the flow model (i.e., $v_n(\mathbf{x}, t) = 0$ on $\Gamma^v \times]0, \mathcal{I}[$), AD equations (i.e., $h^p(\mathbf{x}, t) = 0$ on $\Gamma^h \times]0, \mathcal{I}[$), and heat equations (i.e., $s^p(\mathbf{x}, t) = 0$ on $\Gamma^s \times]0, \mathcal{I}[$). The no flux boundary conditions

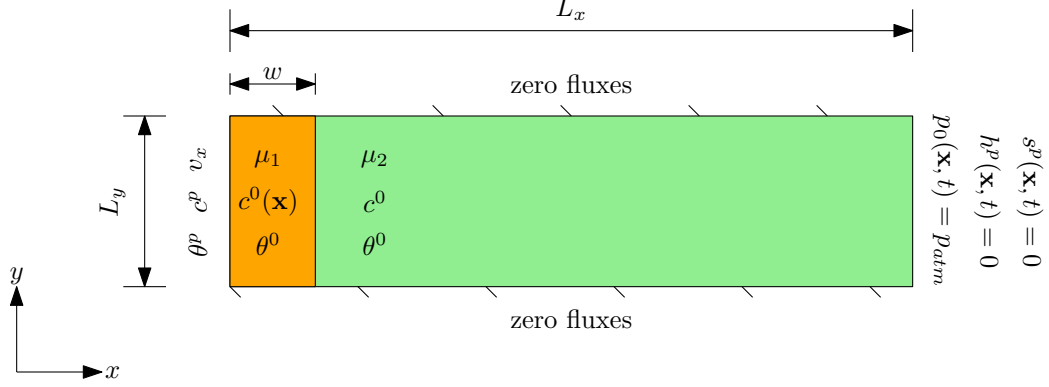


Figure 3.5: Hele-Shaw cell: Pictorial description of the problem including boundary and initial conditions. The computational domain is a $L_x \times L_y$ rectangle. The disturbed fluid $(\mu_1(c, \theta), c, \theta)$ flows into the domain which contains second flow at rest (μ_2, c^0, θ^0) .

are also enforced for AD and heat equations on the right boundary, where the atmosphere pressure is employed for flow model (i.e., $p_0(\mathbf{x}, t) = p_{atm}$ on $\Gamma^p \times]0, \mathcal{I}[$). Initial condition for concentration that distributes instability in the medium is as

$$c(\mathbf{x}, t = 0) = \begin{cases} \alpha \gamma(\mathbf{x}) \exp[-\frac{x^2}{\beta^2}] & \text{for } 0 \leq x \leq w \\ 0 & \text{for } x > w, \end{cases}$$

where the function $\gamma(\mathbf{x})$ represents random function ranging from 0 to 1 and exhibits transverse irregularities in concentration. α is the magnitude of the disturbance and β can be interpreted as the penetration of disturbance from the front. Both α and β have small values relative to unity. The value for w is provided in Tables 3.1.

To complete the coupled model, the viscosity is assumed to depend exponentially on the values of concentration c and temperature θ [Pritchard, 2009, Islam and Azaiez, 2010b, Mishra et al., 2010]:

$$\mu(c, \theta) = \exp [R_c(1 - c) + R_\theta(1 - \theta)], \quad (3.5.1)$$

in which $M = \exp(R_c)$ is mobility ratio in an isothermal miscible displacement and

$M = \frac{\mu_2}{\mu_1}$. R_θ is log-mobility that considers temperature effect in flow. In this section, to investigate impact of temperature we fix $R_c = 2$ and change the thermal log-mobility R_θ in the interval $[-3, 3]$. Moreover, to further study the impact of temperature, we alter Lewis number $\mathbb{L}e$ which is defined as

$$\mathbb{L}e = \frac{\kappa_\theta}{\lambda_{min}}, \quad (3.5.2)$$

where κ_θ is thermal diffusivity and λ_{min} denotes the isotropic diffusion (d_m) or minimum eigenvalue of the anisotropic diffusivity. As diffusion of temperature is faster than diffusion of mass, the Lewis number should be $\mathbb{L}e \geq 1$ [Mishra et al., 2010, Almarcha et al., 2013], so $\mathbb{L}e = 10, 4$ and 1 are used in this work. Very high Péclet number of $\mathbb{P}e = 10^4$ and a moderate value of 2×10^3 , are used herein. The Péclet number is the ratio between the advection and diffusion in transport equation, which is taken as

$$\mathbb{P}e = \frac{L_x \|\mathbf{v}(\mathbf{x}, t)\|}{\lambda_{min}}, \quad (3.5.3)$$

where L_x is the characteristic length and $\|\cdot\|$ is the standard 2-norm. $\|\mathbf{v}\|$ here is simply injection velocity v_x .

Unless otherwise mentioned, all the results are obtained for parameters provided in Table 3.1 in which aspect ratio of the computational domain is $\frac{L_x}{L_y}$. The mesh used for the problem is also 10,000 structured quadrilateral finite (Q4) elements.

3.5.1 A qualitative study

In this part, the time evolution of concentration, temperature, and viscosity in broad range of parameters are presented for better understanding of coupled flow-transport-temperature model in VF. We will discuss the influence of altering Lewis number with the values $\mathbb{L}e = 1, 4$ and 10 , and the thermal log-mobility within the

Table 3.1: Hele-Shaw cell: Parameters used in the problem.

Parameter	Value
$\frac{L_x}{L_y}$	4
w	$0.01L_x$
c^p	1
θ^p	1
θ^0	0.1
p_{atm}	1

wide interval $R_\theta \in [-3, 3]$ for long-time sequences. Moreover, the presented results are for moderate and very high Péclet numbers, that is $\text{Pe} = 2 \times 10^3$ and 10^4 , respectively. These values are chosen for Pe to avoid occurrence of pure diffusion conditions. To the best of our knowledge, there is not a reported research paper for finite element simulation of VF in Hele-Shaw porous media cell for such a high Péclet number. [Moïssis et al., 1988, Coutinho and Alves, 1999, Castro et al., 2001, Riviere and Wheeler, 2002, Dias and Coutinho, 2004, Scovazzi et al., 2013] employed FEM and used $\text{Pe} \leq 2 \times 10^3$. Recently, [Li and Riviere, 2015] utilized a discontinuous Galerkin method in miscible flooding of quarter five-spot problem for very high Péclet number. Also, [Meng and Guo, 2015] proposed a multiple-relaxation-time lattice Boltzmann method for high Péclet numbers in miscible displacement for incompressible Navier-Stokes flow. We use terminologies and mechanisms presented in previous research works including [Tan and Homsy, 1986, 1987, 1988, Zimmerman and Homsy, 1991, Azaiez and Singh, 2002, Islam and Azaiez, 2005] to describe the nonlinear dynamics of VF on formation and development of finger structures, and on interactions of neighboring fingers. By numerical simulations of nonlinear VF, [Tan and Homsy, 1986, 1987, 1988] showed that there are a few dominant finger structures that spread and grow significantly. In consequence, the gradient between the shielded finger and the surrounding becomes steep and the neighboring finger-like patterns grow, too. In addition to shielding, they also characterized mechanism like tip splitting. Then

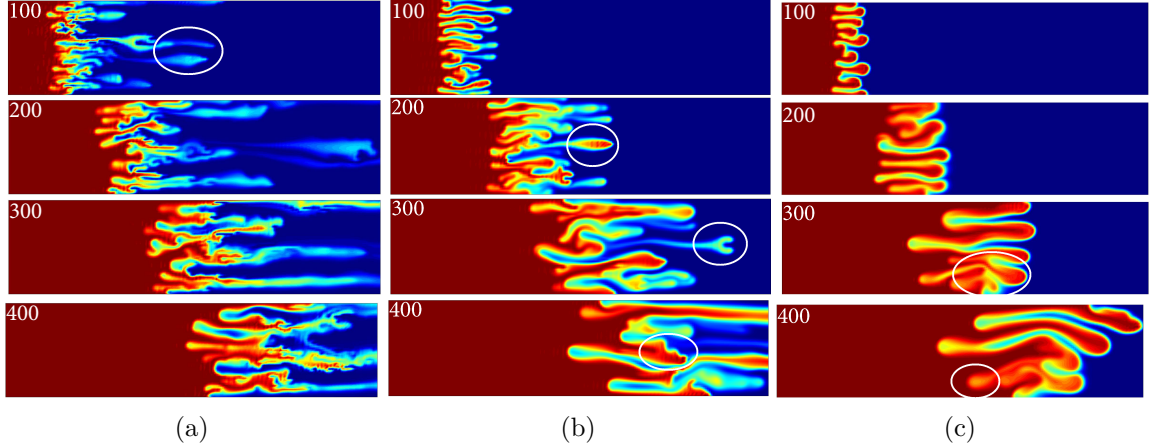


Figure 3.6: Concentration: These figures show concentration profile for $\mathbb{P}e = 10^4$, $\mathbb{L}e = 10$ and $R_c = 2$. Thermal log-mobility is also (a) $R_\theta = -3$, (b) $R_\theta = 0$, and (c) $R_\theta = 3$. The frame numbers indicate the time. Note that $0 \leq c(\mathbf{x}, t) \leq 1$.

they extended the mechanisms in VF instabilities and found new mechanisms like side merging or coalescence and channeling [Zimmerman and Homsy, 1991]. There are some other research papers such as [Azaiez and Singh, 2002, Islam and Azaiez, 2005] in which they developed the previous works and observed new mechanisms.

Figure 3.6 depicts concentration profile for $\mathbb{P}e = 10^4$, $\mathbb{L}e = 10$, $R_c = 2$, and thermal log-mobility $R_\theta = -3, 0$ and 3 . The frame numbers in the top left indicate time. For $R_\theta = -3$ (Figure 3.6(a)) channeling is the dominant mechanism. Side branching is also observed. Moreover, trailing lobe detachment occurs at $t = 200$. Leading lobe detachments that are observed at $t = 100$ in several parts, remain in the domain for a while. It is also produced at next time sequences for $R_\theta = -3$. Tip splitting is identified for $R_\theta = 0$ at frame number $t = 300$ (Figure 3.6(b)). Also, side merging (coalescence) occurs in different parts of the domain. Leading lobe detachment is also identified at $t = 100$ and next time sequences. Alternative side branching which identified by [Islam and Azaiez, 2005] for high log-mobility, is observed at $t = 400$. For both cases ($R_\theta = -3$ and 0) there are clearly shielding mechanism. For $R_\theta = 3$ (Figure 3.6(c)) a coalescence is observed at $t = 300$ and this merging becomes such powerful that starts to change the total pattern of fingers. The

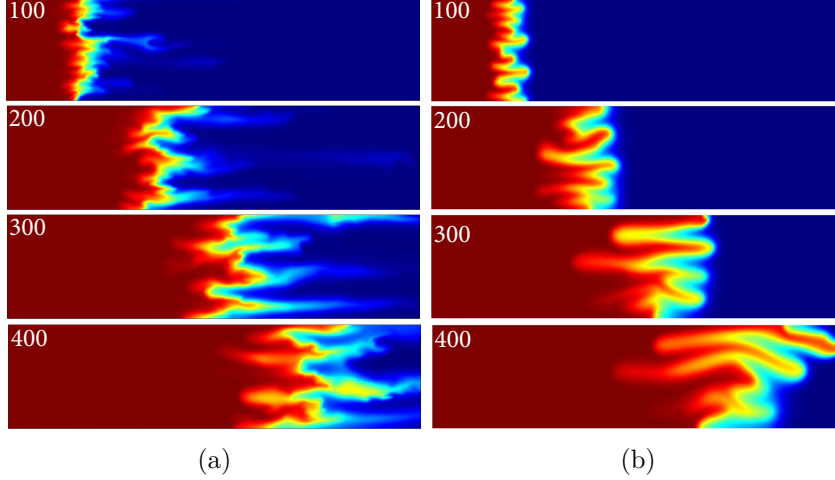


Figure 3.7: Temperature: These figures show temperature $\theta(\mathbf{x}, t)$ for $\mathbb{P}e = 10^4$, $\mathbb{L}e = 10$, and $R_c = 2$. Thermal log-mobility is also (a) $R_\theta = -3$ and (b) $R_\theta = 3$. The frame numbers indicate the time.

trailing lobe detachment is also found at $t = 400$. In terms of the number of initial fingers, by increasing the thermal log-mobility, it decreases. On the other hand, the fingers width decrease from $R_\theta = 3$ to -3 . In addition, if $R_\theta \geq 0$, for $R_\theta = 0$ there are more finger stretching and front advancement compared to $R_\theta = 3$.

Figures 3.7 and 3.8 show temperature and viscosity for $\mathbb{P}e = 10^4$, $\mathbb{L}e = 10$, $R_c = 2$ (exactly the same as Figure 3.6). The temperature in DD can also be interpreted as the specie profile which has 10 times faster diffusion ($\mathbb{L}e = 10$) in this case. Hence, it should be very useful to investigate the treatment of temperature. The temperature profiles are shown for $R_\theta = -3$ and 3. For $R_\theta = -3$ (Figure 3.7(a)) channeling is again dominant. Side branching is also observed. The pattern for $R_\theta = 3$ (Figure 3.7(b)) is almost the same as concentration profile (Figure 3.6(c)) and side merging is identified in frame numbers $t = 200, 300$ and 400. The viscosity is depicted for $R_\theta = 0$ and 3 in Figures 3.8(a) and 3.8(b), respectively. Study of the viscosity is important due to its coupling role in VF and miscible displacement models. In viscosity contours, tip splitting is found for $R_\theta = 0$ at frame number $t = 300$, and side merging and shielding in different parts of the domain. The side merging is the dominant mechanism for

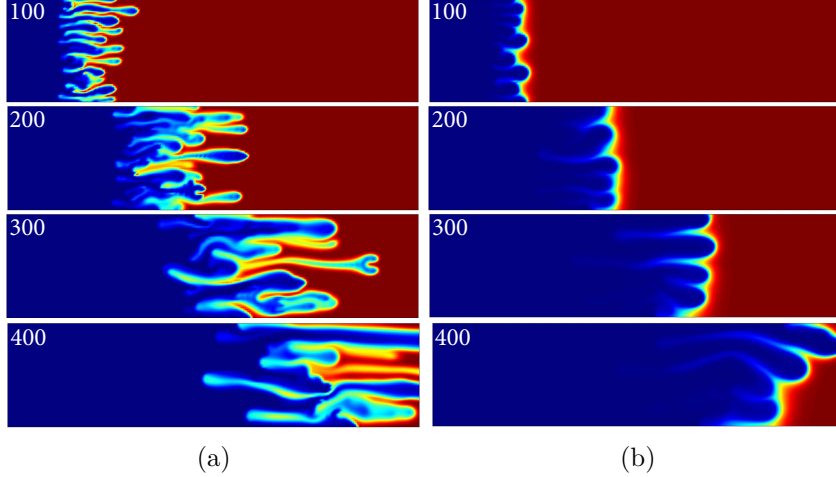


Figure 3.8: Viscosity: These figures show viscosity $\mu_1(c, \theta)$ for $\mathbb{P}e = 10^4$, $\mathbb{L}e = 10$, and $R_c = 2$. Thermal log-mobility is also (a) $R_\theta = 0$ and (b) $R_\theta = 3$. The frame numbers indicate the time.

$R_\theta = 3$ similar to concentration profile in Figure 3.6(c).

The concentration for $\mathbb{P}e = 10^4$, $R_c = 2$, and $R_\theta = 2$ and two different Lewis numbers (i.e., $\mathbb{L}e = 10$ and 4) is shown in Figure 3.9. For $\mathbb{L}e = 10$ which means faster temperature diffusion (Figure 3.9(a)), coalescence begins sooner (at $t = 100$) compared to $\mathbb{L}e = 4$ (Figure 3.9(b)) where at $t = 200$ side merging is found. For $\mathbb{L}e = 10$ at $t = 200$, in addition to side merging, there is a trailing lobe detachment. In both cases, although the number and width of initial fingers are almost the same, the fingers for $\mathbb{L}e = 4$ are more stretching and have more front advancement. Figure 3.10 shows temperature and viscosity for the same parameters in Figure 3.9. The

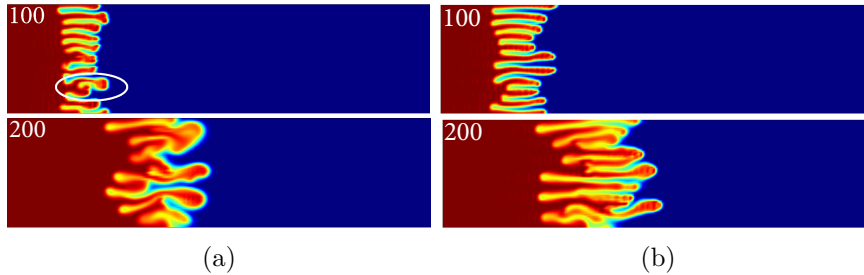


Figure 3.9: Concentration: These figures show concentration $c(\mathbf{x}, t)$ for $\mathbb{P}e = 10^4$, $R_c = 2$, and $R_\theta = 2$. Lewis number is also (a) $\mathbb{L}e = 10$ and (b) $\mathbb{L}e = 4$. The frame numbers indicate the time.

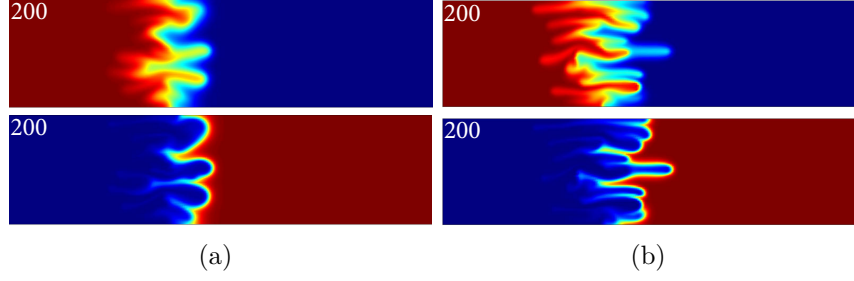


Figure 3.10: Temperature and viscosity: These figures show temperature θ and viscosity μ for $\mathbb{P}e = 10^4$, $R_c = 2$, and $R_\theta = 2$. Lewis number is also (a) $\mathbb{L}e = 10$ and (b) $\mathbb{L}e = 4$. Upper figures depict temperature and lower viscosity profiles.

upper figure depicts temperature and the lower one represents viscosity profiles. The number of initial fingers in temperature and viscosity contours for $\mathbb{L}e = 4$ is higher. However, the fingers width are thicker for $\mathbb{L}e = 10$. Similar to concentration profile for $\mathbb{L}e = 4$ (Figure 3.9(b)), in temperature and viscosity contours there are more finger stretching and front advancement compared to $\mathbb{L}e = 10$.

By decreasing Péclet number to a moderate value, still large numbers of mechanisms are found. Figure 3.11 depicts concentration profile for $\mathbb{P}e = 2 \times 10^3$, $\mathbb{L}e = 10$, $R_c = 2$ and $R_\theta = -3, 0$, and 3 . There are similarities in number and width of initial fingers in current case and high Péclet number ($\mathbb{P}e = 10^4$ in Figure 3.6). Also, finger shielding, stretching and front advancement decrease by increasing the value of R_θ (similar to Figure 3.6). For example, for $R_\theta = -3$ (Figure 3.11(a)) channeling occurs.

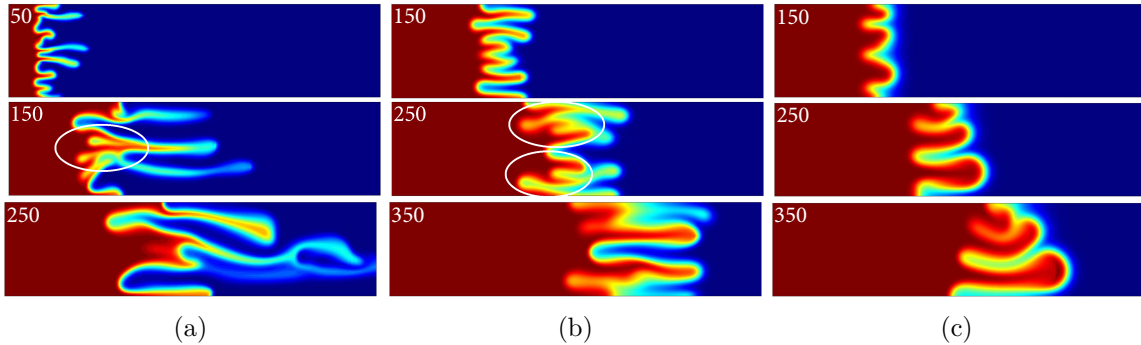


Figure 3.11: Concentration: These figures show concentration $c(\mathbf{x}, t)$ for $\mathbb{P}e = 2 \times 10^3$, $\mathbb{L}e = 10$, and $R_c = 2$. Thermal log-mobility is also (a) $R_\theta = -3$, (b) $R_\theta = 0$, and (c) $R_\theta = 3$. The frame numbers indicate time.

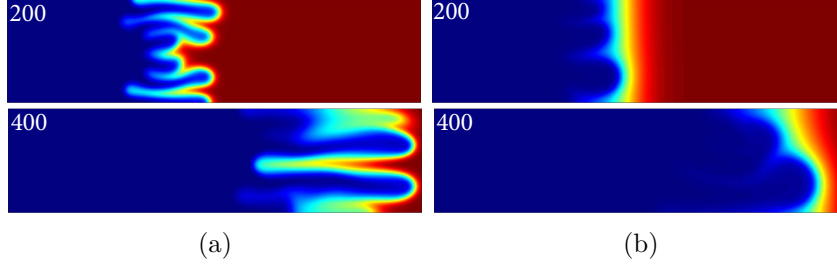


Figure 3.12: Viscosity: These figures show viscosity $\mu_1(c, \theta)$ for $\mathbb{P}e = 2 \times 10^3$, $\mathbb{L}e = 10$, and $R_c = 2$. Thermal log-mobility is also (a) $R_\theta = 0$ and (b) $R_\theta = 3$. The frame numbers indicate time.

Double coalescence as observed by [Islam and Azaiez, 2005] for high log-mobility, are identified for $R_\theta = -3$ and 0 at $t = 150$ and $t = 250$ (Figures 3.11(a) and 3.11(b), respectively). For $R_\theta = 3$, side merging occurs at $t = 350$ (Figure 3.11(c)). Transformation from VF to miscible displacement by altering the thermal log-mobility is clearly shown for viscosity profile in Figure 3.12. In this figure, for $\mathbb{P}e = 2 \times 10^3$, $\mathbb{L}e = 10$, and $R_c = 2$, increasing the thermal log-mobility from $R_\theta = 0$ (Figure 3.12(a)) to $R_\theta = 3$ (Figure 3.12(b)) diminishes the finger-structures.

In Figure 3.13, we can investigate the effect of Péclet and Lewis numbers for $R_c = 2$ and $R_\theta = 2$ in DD situation. It is identified that for $\mathbb{P}e = 10^4$ the initial fingers are formed much more sooner, also with high numbers (Figure 3.13(a)) compared to $\mathbb{P}e = 2 \times 10^3$ (Figure 3.13(b)). For $\mathbb{P}e = 10^4$, side merging is observed at $t \geq 150$, while for $\mathbb{P}e = 2 \times 10^3$ it is identified at $t = 350$. For $\mathbb{P}e = 10^4$, there are also trailing lobe detachment at $t \geq 150$ and leading lobe detachment at $t = 250$ and 350 . There are also identified mechanisms for high log-mobility introduced in [Islam and Azaiez, 2005] for $\mathbb{P}e = 10^4$ such as skewering at $t = 150$ and alternating side branching at $t = 200$. Moreover, by comparing Figures 3.13(b) and 3.13(c), we can investigate influence of Lewis number for a specific Péclet number (here $\mathbb{P}e = 2 \times 10^3$). It can be observed that for $\mathbb{L}e = 1$ (which is the lowest possible Lewis number), as temperature diffuses faster, the fingers not only formed faster, but also advanced faster. There are also trailing lobe detachment and coalescence at $t \geq 200$ in Figure 3.13(c). For

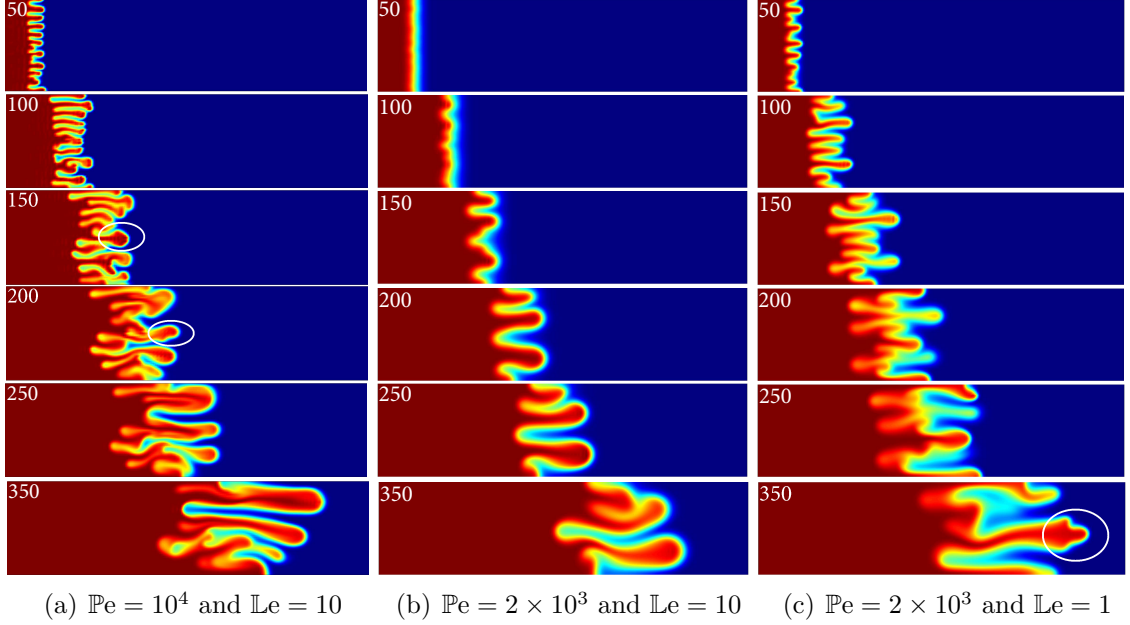


Figure 3.13: Concentration: These figures show concentration $c(\mathbf{x}, t)$ for $R_c = 2$ and $R_\theta = 2$. The frame numbers indicate time. Mechanisms for high log-mobility introduced in [Islam and Azaiez, 2005] such as skewering and alternating side branching are observed.

$\mathbb{L}e = 1$ at $t = 350$ the skewing mechanism is also identified which is not observed for $\mathbb{L}e = 10$ (Figure 3.13(b)).

3.5.2 A quantitative study

In order to monitor effect of temperature in dynamics of VF and miscible displacement, in addition to qualitative observation, a parametric studies are performed. We address mixing time and mixing length quantities to characterize the interplay of mixing and fingering phenomenon. For the following presented results, parameters provided in Table 3.1 are used.

3.5.2.1 Mixing time

First, we study the spatial distribution of concentration as a quantitative analysis. Let us define the *temporal* evolution of transverse concentration for quantity $\bar{\mathcal{C}}$ as

$$\bar{C}(t) = \int_0^{L_y} c(\mathbf{x}, t) dy. \quad (3.5.4)$$

This is a mixing parameter by which we evaluate *mixing time* in VF phenomenon. Mixing time is also defined as

$$t_{\text{mix}} = t\Big|_{\bar{C}=1-\delta} - t\Big|_{\bar{C}=\delta}, \quad (3.5.5)$$

where δ is a small positive number. Time evolution of transverse concentration $\bar{C}(t)$ is plotted in Figure 3.14 for $R_c = 2$ and different thermal log-mobility, Péclet, and Lewis numbers at $L_x/2$. The results show that mixing time is shorter for smaller value of $|R_c - R_\theta|$ and *minimum* mixing time occurs for $R_\theta = 2$. For $R_\theta = -3$, it is observed that the finger channeling retards mixing by increasing mixing time [Jha et al., 2013]. For a specific Lewis number ($Le = 10$, in Figure 3.14(d)), increasing Péclet number increases the mixing time. Also, for a fixed Péclet number ($Pe = 2 \times 10^3$ in Figure 3.14(e)) higher Lewis numbers have longer mixing time.

3.5.2.2 *Mixing length*

References [Norouzi and Shoghi, 2014, Zimmerman and Homsy, 1991] also plotted variation of average transverse concentration $\bar{c}(x)$ vs. longitudinal length which is given as

$$\bar{c}(x) = \frac{1}{n} \sum_{i=1}^n c(x, y_i, t). \quad (3.5.6)$$

Then they used these average quantity to evaluate *mixing length* in VF. Mixing length is evaluated as follows:

$$l_{\text{mix}} = x\Big|_{\bar{c}=\delta} - x\Big|_{\bar{c}=1-\delta}, \quad (3.5.7)$$

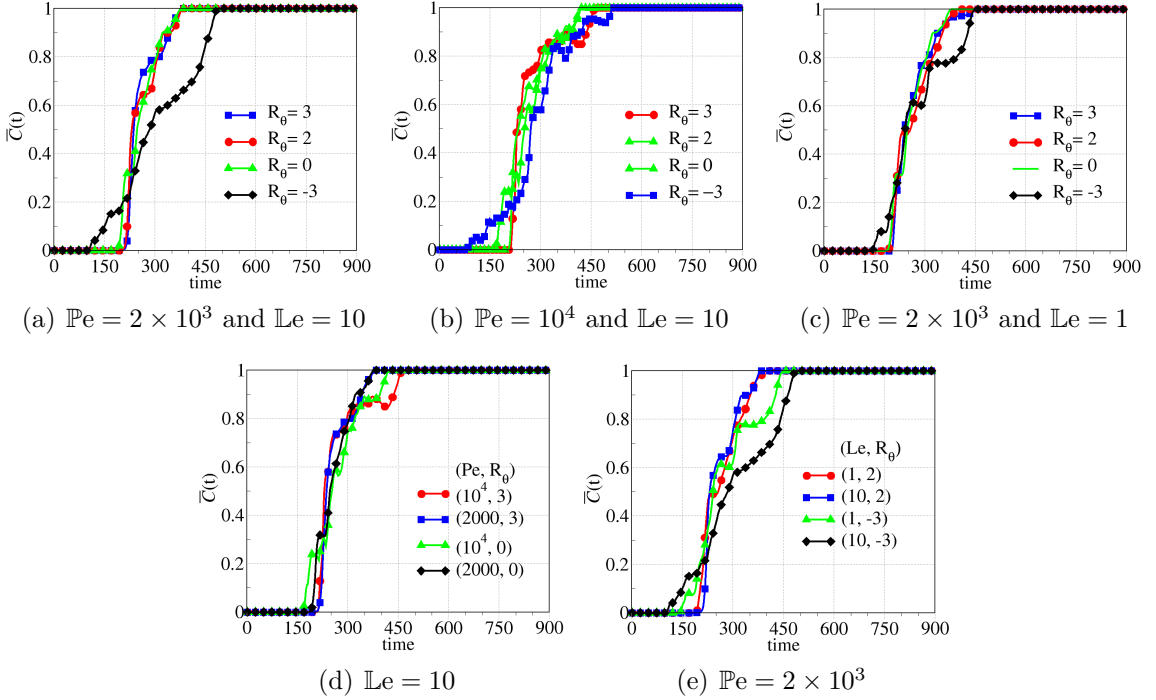


Figure 3.14: Mixing time: These figures show average transverse concentration $\bar{c}(t)$ vs. time $R_c = 2$ at $L_x/2$. Mixing time is shorter for smaller values of $|R_c - R_\theta|$ and *minimum* mixing time occurs for $R_\theta = 2$. For $R_\theta = -3$, it is observed that the tip splitting and finger channeling increase mixing time.

in which δ is again a small positive number. Figure 3.15 shows average transverse concentration $\bar{c}(x)$ vs. x for $R_c = 2$ and various thermal log-mobility, Péclet, and Lewis numbers at $t = 100, 200$, and 300 . The results show that mixing length is also shorter for smaller value of $|R_c - R_\theta|$ and *minimum* mixing length occurs again for $R_\theta = 2$. For $R_\theta = -3$, it is observed that the finger channeling increases mixing length, as well as mixing time. For a fixed Lewis number ($\mathbb{L}e = 10$, in Figure 3.15(e)), increasing Péclet number increases the mixing length. Also, for a specific Péclet number ($\mathbb{P}e = 2 \times 10^3$ in Figure 3.15(f)) lower Lewis numbers have longer mixing length. It should be noted that the mixing length for same set of parameters increases by time evolution. It means, mixing length is longer for $t = 300$ than $t = 200$ and 100 for specific $\mathbb{P}e$, $\mathbb{L}e$, and R_θ .

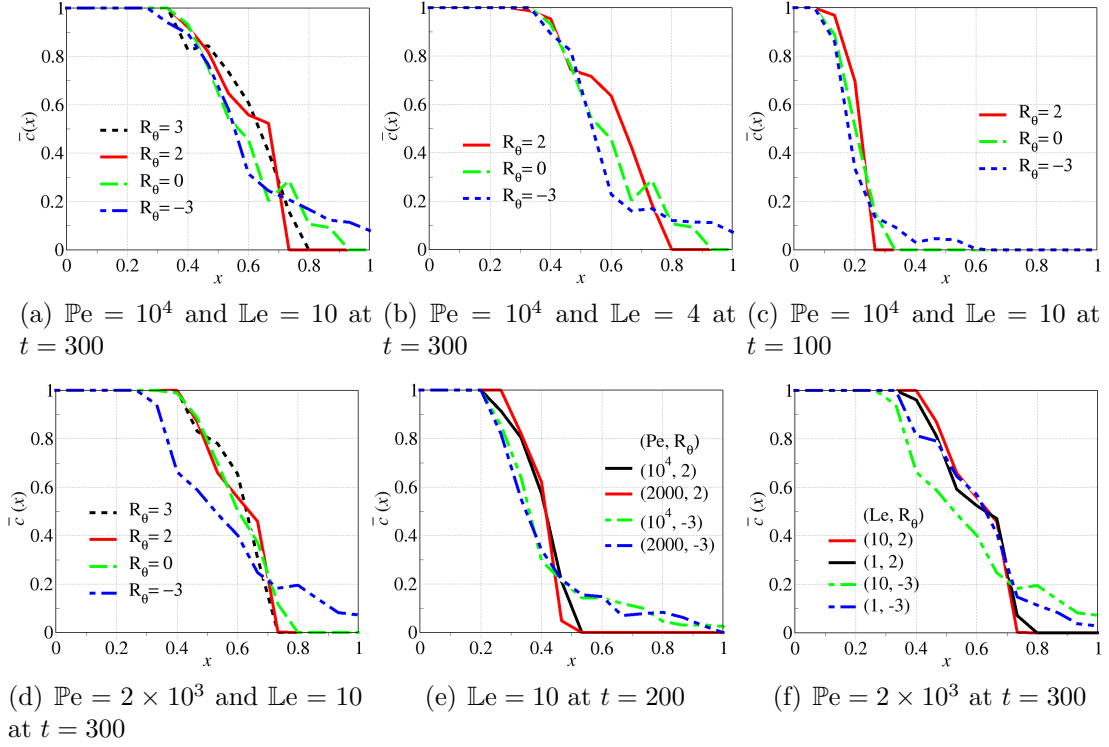


Figure 3.15: Mixing length: These figures show average transverse concentration $\bar{c}(x)$ vs. x for $R_c = 2$. Mixing length is shorter for smaller values of $|R_c - R_\theta|$ and *minimum* mixing length occurs again for $R_\theta = 2$. For $R_\theta = -3$, it is observed that the tip splitting and finger channeling increase mixing length.

3.6 Numerical results: Impact of employing stabilized formulations

To study effects of numerical stabilizers on VF, we will solve quarter five-square problem in porous media. A pictorial description of the initial boundary value problem is shown in Figure 3.16. The reason to choose this problem is that quarter five-square does not need any induced mathematical instabilities such as Hele-Shaw cell to initiate VF instability. Due to chemical reaction that exists in ADR model and DD effects, even in the case of homogeneous and isotropic permeability, VF is expected. The computational domain is a square with length $L = 1$. There are also two small squares with length W in bottom left (Ω^I) and top right (Ω^P) corners. From the injection well of Ω^I , displacing fluid mass (φ^I) is injected into

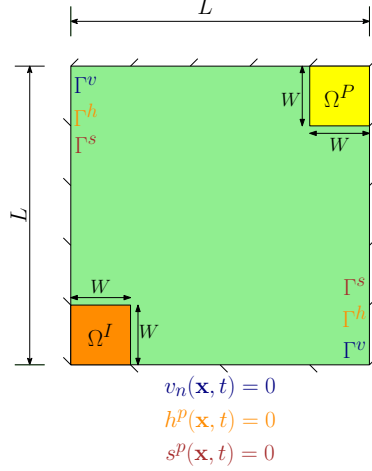


Figure 3.16: Quarter five-square: Pictorial description of the problem including initial and boundary conditions. The computational domain includes a unit square and two small squares with length W as injection and production wells.

Table 3.2: Quarter five-square: Parameters used in the problem.

Parameter	Value
d_m	10^{-7}
$f(\mathbf{x}, t)$	φ^I in Ω^I
$r(\mathbf{x}, t, c)$	$-\varphi^P c$ in Ω^P
$g(\mathbf{x}, t)$	φ^I in Ω^I
$q(\mathbf{x}, t, \theta)$	$-\varphi^P \theta$ in Ω^P

the domain which is already filled by displaced fluid at rest. The top right square (Ω^P) is production well that has mass sink (φ^P). Elsewhere, $\varphi^I = \varphi^P = 0$. Homogeneous velocity is enforced on the entire boundary (i.e., $\Gamma^v \times]0, \mathcal{I}[= \partial\Omega$). That is, $v_n(\mathbf{x}, t) = 0$ for Darcy model. The zero fluxes are also prescribed on the entire boundary for ADR equations (i.e., $h^p(\mathbf{x}, t) = 0$ on $\Gamma^h \times]0, \mathcal{I}[= \partial\Omega$) and heat equations (i.e., $s^p(\mathbf{x}, t) = 0$ on $\Gamma^s \times]0, \mathcal{I}[= \partial\Omega$). As before, the viscosity is assumed to depend exponentially on the concentration and temperature. That is, $\mu = \mu_0 \exp[R_c(1 - c) + R_\theta(1 - \theta)]$.

We have employed 100×100 quadrilateral finite elements to numerically solve the coupled flow, reactive transport, and temperature model in quarter five-square problem. Using parameters provided in Table 3.2, and utilizing SUPG formulation

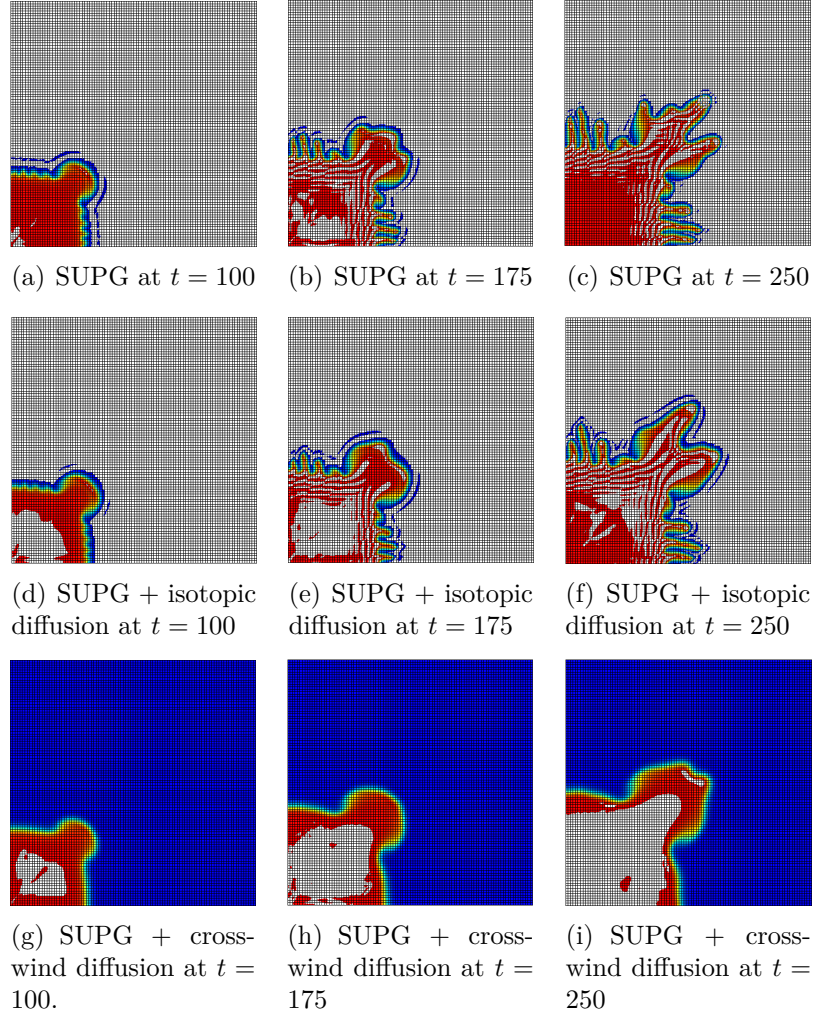


Figure 3.17: Violation of maximum principle: The upper figures are concentrations for SUPG formulation (eq. (3.3.5)). the middle figures are for modified SUPG in which we added isotropic artificial diffusion (eq. (3.3.7)) and bottom figures are for modified SUPG with crosswind artificial diffusion (eq. (3.3.8)).

and its modifications, results shown in Figure 3.17 are obtained. The plots depict concentration $c(\mathbf{x}, t)$ at time $t = 100, 175$ and 250 . The length of W in injection and production well equals to $L/10$. The log-mobility are $R_c = R_\theta = 2$, and the injection source and production sink are $\varphi^I = \varphi^P = 0.1$, respectively. The concentration does not remain in the range of $[0, 1]$, so the numerical results have violated the maximum principle (and in consequence the non-negative constraint). For instance, at $t = 250$ concentration under SUPG formulation is $-2.75 \leq c \leq 6.21$.

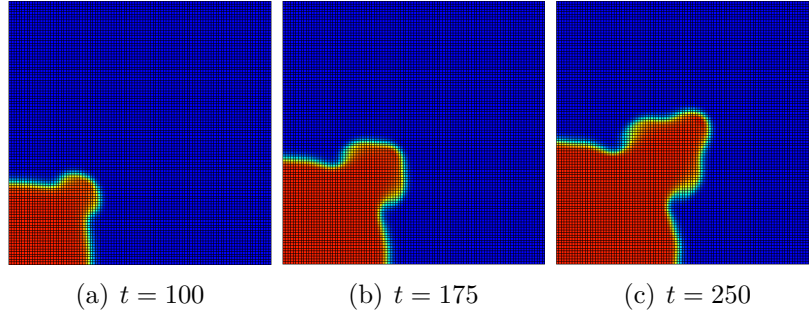


Figure 3.18: Physical instability diminishing: These figures show concentration at different time steps for quarter five-square with modified SUPG stabilized formulation in which we added both isotropic and crosswind artificial diffusion.

To obtain accurate numerical solutions and avoid spurious oscillation, we have employed modified SUPG formulation (SUPG plus both isotropic and crosswind artificial diffusion terms) provided in Section 3.3. Figure 3.18 shows the solution for concentration. The parameters are exactly the same as Figure 3.17. The results clearly show that the stabilized formulations diminish numerical oscillations and satisfy maximum principle (and non-negative constraint) for the concentration which is desired. However, stabilizers suppress hydrodynamic instabilities and we do not observe VF.

Then using $W = L/20$, $\varphi^I = \varphi^P = 0.2$, and again similar parameters provided in Table 3.2, to solve the problem. The results for SUPG stabilized formulations and its modification even for very low values for R_c and R_θ (for instance, $R_c = 1$ and $R_\theta = 0$), violate maximum principle and non-negative constraint.

3.7 Concluding remarks

The effects of temperature in terms of Lewis number ($\mathbb{L}e$), thermal log-mobility ratio (R_θ), and Péclet number ($\mathbb{P}e$) are investigated on VF and miscible displacement. For high value of R_θ , R_c , and $\mathbb{P}e$, the traditional numerical formulation for VF simulation is not stable. So, we resort to finite element formulation to solve such a highly

nonlinear coupled problem. The main contributions of the paper can be summarized as follows:

- (a) By considering effect of temperature (double diffusive effects), mechanisms like double coalescence, skewering, and alternating side branching are identified. These mechanisms are merely observed in single diffusivity case for very high log-mobility [Islam and Azaiez, 2005].
- (b) As $\mathbb{L}e \geq 1$, the results show that for values of $\mathbb{L}e$ close to one, finger patterns are more stretching and channeling. The similar mechanisms happen when one increases the Péclet number or uses negative thermal log-mobility.
- (c) It is found that in presence of temperature (double diffusive instability), $|R_c - R_\theta|$ can interpret mixing in VF phenomenon better than R_θ . Also, minimum mixing time and length observed for $|R_c - R_\theta| \simeq 0$. So, it can be concluded that for $|R_c - R_\theta| \simeq 0$ optimum mixing occurs. It should be noted that the $\mathbb{P}e$ and $\mathbb{L}e$ still have significant influence in VF.
- (d) It is shown that among the mechanisms, finger channeling by retarding the creation of interfacial fluid-fluid area, reduces mixing. On the other hand, tip splitting mechanism, which leads to growth of adjacent fingers and creation of more interface area, enhances mixing.
- (e) To show the impact of flow disorder (velocity gradient) and concentration/temperature gradient in mixing, the scaling parameters χ , $\varepsilon_{c\theta}$ and ε_v are defined for correlation of temperature and concentration, and for flow. Then, by utilizing numerical simulation the scaling expression $\langle \chi^2 \rangle \sim t^2$ and $\varepsilon_v \sim \varepsilon_{c\theta}$ are identified.
- (f) The numerical results violate the *maximum principle* and non-negative constraint for the concentration. Also, the results obviously show that the utilized numerical stabilizers suppress physical instabilities and influence of temperature. Also,

to avoid unphysical values for concentration, it is recommended to utilize non-negative formulation proposed in [Mudunuru and Nakshatrala, 2016] or discontinuous Galerkin method presented in [Li and Riviere, 2015].

Chapter 4

VISCOUS FINGERING IN POROUS MEDIA WITH DOUBLE PERMEABILITY: MODEL, STABILITY, AND NUMERICAL SOLUTION

A theory that explains everything, explains nothing.

Karl Popper

4.1 Introduction and background

Most of the porous media models assume that the pore spaces have the same size with single porosity and permeability. However, in real porous materials, pore size distribution with more than single porosity can be clearly distinguished. Herein, we consider a geo-material with two dominant permeability for micro-scale and macro-scale structures so-called double porosity/permeability. We will assume two pore-network with different permeability in which the micro-structure represents the fracture network and micro-structure is a network for matrix.

Various mathematical models have been proposed for double porosity/permeability problems [Dykhuizen, 1990, Vogel et al., 2000, Balogun et al., 2007, Boutin and Royer,

2015, Amaziane and Pankratov, 2016]. In current study we allow mass transfer between the micro- and macro-network. This assumption is based on mathematical framework recently developed by [Nakshatrala et al., 2016a]. The main features of the proposed model can be summarized as follows: (i) the medium has two different pore-networks; (ii) the governing equations for each network is Darcy (iii) there is a mass transfer between the micro- and macro-structure; (iv) pore-structures are continuum, and the model allows mass and chemical species transports within each pore-network.

Herein, the linear stability analysis and numerical solutions of viscous fingering in porous media is conducted to study the effects of the main parameters on the flow instability in double permeability medium. [Tan and Homsy, 1986] presented a theoretical approach for stability analysis of miscible viscous fingering in porous media under single permeability assumption. They used quasi-steady state approximation (QSSA) and predicted the growth rate of instability. The QSSA is based on the assumption that the growth rate of perturbations is asymptotically faster than the rate of change of the background state. Then, the most dangerous wavelengths at any point in time at which the base state was “frozen” is determined. The QSSA have been widely used for linear stability analysis of miscible viscous fingering in porous media [Tan and Homsy, 1987, Azaiez and Singh, 2002, Pramanik and Mishra, 2013]. For example [Wit and Homsy, 1997] conducted linear stability analysis of viscous fingering in a heterogeneous porous medium with periodic permeability. [Ghesmat and Azaiez, 2008] on the other hand, investigated the effect of anisotropic velocity dependent dispersion on linear stability of viscous fingering in a porous medium. Also, [Hejazi et al., 2010] performed a parametric study in terms of log-mobility ratios and Domkohler number for linear stability of miscible reactive viscous fingering. Recently, [Norouzi and Shoghi, 2014] analyzed linear stability of viscous fingering in porous medium with anisotropic permeability and diffusivity. Moreover, [Pritchard, 2004,

2009, Islam and Azaiez, 2010a] studied linear stability of double diffusive problems in miscible viscous fingering in radial and rectilinear geometries.

To the best of our knowledge, there is not any stability analysis for double porosity/permeability viscous fingering in porous medium. The only study in the literature which can be relevant, is the work done by [Sajjadi and Azaiez, 2013]. In this study, they performed numerical simulation of layered heterogeneous porous media with single porosity assumption in which the values of permeability in layers are scalar and varies between 0.7 to 1.6. Herein, the governing equations are derived for coupled double permeable anisotropic porous media flow and advection-diffusion models. Then, a parametric study for the influence of the anisotropic permeability of micro- and macro-network, log-mobility, and mass transfer between micro- and macro-structure on linear stability of viscous fingering will be conducted. Moreover, by employing finite element formulations, the influence of parameters on the concentration profiles is presented.

The rest of the chapter is organized as follows. The governing equations for coupled flow and transport in porous media with double permeability along with the linearization of the governing equations are presented in Section 4.2. The model problem and its base-state solution are presented in Section 4.3. In Section 4.4 the stability of the base-state solution is systematically analyzed. Moreover, numerical solutions of the governing equations by utilizing finite element formulations is performed. Conclusions for this Chapter are drawn in Section 4.5.

4.2 Governing equations and linearization

In this section, we outline the governing equations for coupled transport and flow in porous media with double permeability. To this end, we denote a spatial point by \mathbf{x} , and the time by t . The gradient and divergence operators with respect to \mathbf{x} are, respectively, denoted by $\text{grad}[\cdot]$ and $\text{div}[\cdot]$. We denote the concentration

of the chemical species by $c(\mathbf{x}, t)$. We assume that the porous medium has two pore-networks, which will be referred to as macro-pore and micro-pore networks. We allow mass transfer across the two pore-networks. For assumptions and mathematical properties of double porosity/permeability models, refer to [Nakshatrala et al., 2016a] and references therein. We denote the permeabilities in the macro-pore and micro-pore networks by \mathbf{K}_M and \mathbf{K}_m , respectively. The discharge velocities in the macro-pore and micro-pore networks are, respectively, denoted by $\mathbf{u}_M(\mathbf{x}, t)$ and $\mathbf{u}_m(\mathbf{x}, t)$. The pressures in these two pore-networks are denoted by $p_M(\mathbf{x}, t)$ and $p_m(\mathbf{x}, t)$.

The fate of the chemical species is governed by the following advection-diffusion equation:

$$\frac{\partial c}{\partial t} + \text{div}[\mathbf{u}c] - \text{div}[D\text{grad}[c]] = f(\mathbf{x}, t), \quad (4.2.1)$$

where \mathbf{u} is the advection velocity, D is the diffusivity coefficient, and $f(\mathbf{x}, t)$ is the volumetric source/sink for the chemical species. The flow of an incompressible fluid in a porous medium with double permeability is governed by the following equations:

$$\mu(c)\mathbf{K}_M^{-1}\mathbf{u}_M + \text{grad}[p_M] = \gamma\mathbf{b}(\mathbf{x}), \quad (4.2.2a)$$

$$\mu(c)\mathbf{K}_m^{-1}\mathbf{u}_m + \text{grad}[p_m] = \gamma\mathbf{b}(\mathbf{x}), \quad (4.2.2b)$$

$$\text{div}[\mathbf{u}_M] = -\frac{\beta}{\mu(c)}(p_M - p_m), \quad \text{and} \quad (4.2.2c)$$

$$\text{div}[\mathbf{u}_m] = +\frac{\beta}{\mu(c)}(p_M - p_m), \quad (4.2.2d)$$

where γ is the true density of the fluid; $\mathbf{b}(\mathbf{x})$ is the specific body force; β is a scalar parameter, which depends on the porous media; and μ is the viscosity of the fluid, which depends on the concentration of the attendant chemical species. We employ the standard expression for the dependence of viscosity on the concentration [Tan

and Homsy, 1986]:

$$\mu = \mu_0 \exp[R_c c], \quad (4.2.3)$$

where μ_0 , which in the context of miscible displacement and viscous fingering, is the viscosity of the displacing fluid, and R_c is the mobility ratio. The advection velocity is the sum of the discharge velocities in the macro-pore and micro-pore networks:

$$\mathbf{u}(\mathbf{x}, t) = \mathbf{u}_M(\mathbf{x}, t) + \mathbf{u}_m(\mathbf{x}, t). \quad (4.2.4)$$

The resulting governing equations are coupled nonlinear equations, and the coupling is two-way. That is, the transport of the chemical species depends on the advection velocity that is obtained from the flow problem, and the flow is affected by the viscosity, which depends on the concentration of the chemical species.

4.2.1 Two-scale expansion and linearization

We linearize the governing equations by employing a two-scale expansion, which provides the corresponding governing equations for the base-state solution and for the perturbed solution. To this end, we decompose the field variables as

$$\mathbf{u}_M(\mathbf{x}, t) = \bar{\mathbf{u}}_M(\mathbf{x}, t) + \varepsilon \tilde{\mathbf{u}}_M(\mathbf{x}, t), \quad (4.2.5)$$

$$\mathbf{u}_m(\mathbf{x}, t) = \bar{\mathbf{u}}_m(\mathbf{x}, t) + \varepsilon \tilde{\mathbf{u}}_m(\mathbf{x}, t), \quad (4.2.6)$$

$$p_M(\mathbf{x}, t) = \bar{p}_M(\mathbf{x}, t) + \varepsilon \tilde{p}_M(\mathbf{x}, t), \quad (4.2.7)$$

$$p_m(\mathbf{x}, t) = \bar{p}_m(\mathbf{x}, t) + \varepsilon \tilde{p}_m(\mathbf{x}, t), \quad \text{and} \quad (4.2.8)$$

$$c(\mathbf{x}, t) = \bar{c}(\mathbf{x}, t) + \varepsilon \tilde{c}(\mathbf{x}, t), \quad (4.2.9)$$

where $\varepsilon \ll \mathcal{O}(1)$ is a small parameter. The decomposition of the concentration field

gives rise to the following decomposition of the viscosity:

$$\mu(c) = \bar{\mu}(c) + \varepsilon \tilde{\mu}(c). \quad (4.2.10)$$

Noting equation (4.2.3), we have

$$\bar{\mu} = \mu_0 \exp[R_c \bar{c}] \quad \text{and} \quad \tilde{\mu} = \mu_0 R_c \tilde{c}. \quad (4.2.11)$$

The governing equations for the base-state solution can be obtained by collecting the terms containing ε^0 :

$$\bar{\mu}(c) \mathbf{K}_M^{-1} \bar{\mathbf{u}}_M + \text{grad}[\bar{p}_M] = \gamma \mathbf{b}(\mathbf{x}), \quad (4.2.12a)$$

$$\bar{\mu}(c) \mathbf{K}_m^{-1} \bar{\mathbf{u}}_m + \text{grad}[\bar{p}_m] = \gamma \mathbf{b}(\mathbf{x}), \quad (4.2.12b)$$

$$\text{div}[\bar{\mathbf{u}}_M] = -\frac{\beta}{\bar{\mu}} (\bar{p}_M - \bar{p}_m), \quad (4.2.12c)$$

$$\text{div}[\bar{\mathbf{u}}_m] = +\frac{\beta}{\bar{\mu}} (\bar{p}_M - \bar{p}_m), \quad \text{and} \quad (4.2.12d)$$

$$\frac{\partial \bar{c}}{\partial t} + (\bar{\mathbf{u}}_M + \bar{\mathbf{u}}_m) \cdot \text{grad}[\bar{c}] - \text{div}[D \text{grad}[\bar{c}]] = 0. \quad (4.2.12e)$$

The governing equations for the perturbations can be obtained by collecting the terms containing ε^1 :

$$\tilde{\mu}(c) \mathbf{K}_M^{-1} \tilde{\mathbf{u}}_M + \bar{\mu}(c) \mathbf{K}_M^{-1} \tilde{\mathbf{u}}_M + \text{grad}[\tilde{p}_M] = \mathbf{0}, \quad (4.2.13a)$$

$$\tilde{\mu}(c) \mathbf{K}_m^{-1} \tilde{\mathbf{u}}_m + \bar{\mu}(c) \mathbf{K}_m^{-1} \tilde{\mathbf{u}}_m + \text{grad}[\tilde{p}_m] = \mathbf{0}, \quad (4.2.13b)$$

$$\text{div}[\tilde{\mathbf{u}}_M] + R_c \tilde{c} \text{div}[\bar{\mathbf{u}}_M] = -\frac{\beta}{\tilde{\mu}} (\tilde{p}_M - \tilde{p}_m), \quad (4.2.13c)$$

$$\text{div}[\tilde{\mathbf{u}}_m] + R_c \tilde{c} \text{div}[\bar{\mathbf{u}}_m] = +\frac{\beta}{\tilde{\mu}} (\tilde{p}_M - \tilde{p}_m), \quad \text{and} \quad (4.2.13d)$$

$$\frac{\partial \tilde{c}}{\partial t} + (\bar{\mathbf{u}}_M + \bar{\mathbf{u}}_m) \cdot \text{grad}[\tilde{c}] + (\tilde{\mathbf{u}}_M + \tilde{\mathbf{u}}_m) \cdot \text{grad}[\bar{c}] - \text{div}[D \text{grad}[\tilde{c}]] = 0. \quad (4.2.13e)$$

4.3 Model problem: Rectilinear flow

4.3.1 Problem description

Study of [Zimmerman and Homsy, 1992a] identified that the mechanisms in two-dimensional simulations of viscous fingering persist to those in three dimensions. They concluded that the two-dimensional simulations are sufficient to capture essential features of viscous fingering instability. Therefore, we consider the domain to be an infinite two-dimensional porous media with dual permeability. Without loss of generality, we assume that the domain to be x - y plane. The unit vectors along the x and y directions are denoted by $\hat{\mathbf{i}}$ and $\hat{\mathbf{j}}$, respectively. The permeability tensors in macro- and micro-pore networks are, respectively, taken as

$$\mathbf{K}_M = \begin{pmatrix} K_1 & 0 \\ 0 & K_2 \end{pmatrix} \quad \text{and} \quad \mathbf{K}_m = \begin{pmatrix} k_1 & 0 \\ 0 & k_2 \end{pmatrix}, \quad (4.3.1)$$

where K_1 , K_2 , k_1 and k_2 are all positive constants. We shall denote the velocities in the macro- and micro-pore networks as

$$\mathbf{u}_M = V_x \hat{\mathbf{i}} + V_y \hat{\mathbf{j}} \quad \text{and} \quad \mathbf{u}_m = v_x \hat{\mathbf{i}} + v_y \hat{\mathbf{j}}. \quad (4.3.2)$$

The initial conditions for the flow in the porous media is taken as

$$V_x(x, y, t = 0) = \frac{K_1}{K_1 + k_1}, \quad V_y(x, y, t = 0) = 0, \quad \text{and} \quad (4.3.3)$$

$$v_x(x, y, t = 0) = \frac{k_1}{K_1 + k_1}, \quad v_y(x, y, t = 0) = 0. \quad (4.3.4)$$

The initial concentration is taken as

$$c(x, y, t = 0) = H(x), \quad (4.3.5)$$

where $H(x)$ is the Heaviside function. The model problem is pictorially described in Figure 4.1.

4.3.2 Non-dimensionalization

We shall take D [L^2T^{-1}] and U [LT^{-1}] as the reference quantities. The length scale will then be D/U , and the time scale will be D/U^2 . It is convenient to move the coordinate system with velocity

$$\mathbf{v}_{\text{ref}} = U\hat{\mathbf{i}} = \hat{\mathbf{i}}. \quad (4.3.6)$$

Under the transformed coordinate system, the initial conditions for the flow in the porous media become

$$V_x(x, y, t = 0) = \frac{-k_1}{K_1 + k_1}, \quad V_y(x, y, t = 0) = 0, \quad \text{and} \quad (4.3.7)$$

$$v_x(x, y, t = 0) = \frac{-K_1}{K_1 + k_1}, \quad v_y(x, y, t = 0) = 0. \quad (4.3.8)$$

Under the new transformed coordinate system, the governing equations are:

$$K_1 \frac{\partial p_M}{\partial x} = -\mu V_x - \mu, \quad (4.3.9a)$$

$$K_2 \frac{\partial p_M}{\partial y} = -\mu V_y, \quad (4.3.9b)$$

$$k_1 \frac{\partial p_m}{\partial x} = -\mu v_x - \mu, \quad (4.3.9c)$$

$$k_2 \frac{\partial p_m}{\partial y} = -\mu v_y, \quad (4.3.9d)$$

$$\mu \left(\frac{\partial V_x}{\partial y} + \frac{\partial V_y}{\partial x} \right) = \mu \left(\frac{\partial V_x}{\partial x} + \frac{\partial V_y}{\partial y} \right) = -\beta(p_M - p_m), \quad (4.3.9e)$$

$$\mu \left(\frac{\partial v_x}{\partial y} + \frac{\partial v_y}{\partial x} \right) = \mu \left(\frac{\partial v_x}{\partial x} + \frac{\partial v_y}{\partial y} \right) = +\beta(p_M - p_m), \quad \text{and} \quad (4.3.9f)$$

$$\frac{\partial c}{\partial t} + (V_x + v_x + 1) \frac{\partial c}{\partial x} + (V_y + v_y) \frac{\partial c}{\partial y} = \frac{\partial^2 c}{\partial x^2} + \frac{\partial^2 c}{\partial y^2}. \quad (4.3.9g)$$

We decompose the solution for the model problem as a sum of the base-state solution and a perturbation, which take the following mathematical form:

$$V_x(x, y, t) = \bar{V}_x(x, t) + \varepsilon \tilde{V}_x(x, y, t), \quad (4.3.10a)$$

$$V_y(x, y, t) = \bar{V}_y(x, t) + \varepsilon \tilde{V}_y(x, y, t), \quad (4.3.10b)$$

$$v_x(x, y, t) = \bar{v}_x(x, t) + \varepsilon \tilde{v}_x(x, y, t), \quad (4.3.10c)$$

$$v_y(x, y, t) = \bar{v}_y(x, t) + \varepsilon \tilde{v}_y(x, y, t), \quad (4.3.10d)$$

$$p_M(x, y, t) = \bar{p}_M(x, t) + \varepsilon \tilde{p}_M(x, y, t), \quad (4.3.10e)$$

$$p_m(x, y, t) = \bar{p}_m(x, t) + \varepsilon \tilde{p}_m(x, y, t), \quad (4.3.10f)$$

$$c(x, y, t) = \bar{c}(x, t) + \varepsilon \tilde{c}(x, y, t), \quad \text{and} \quad (4.3.10g)$$

$$\mu(x, y, t) = \bar{\mu}(x, t) + \varepsilon \tilde{\mu}(x, y, t). \quad (4.3.10h)$$

4.3.3 Base-state solution

The base-state solution for the model problem can be written as follows:

$$\bar{V}_x(x, t) = \frac{-k_1}{K_1 + k_1}, \quad \bar{V}_y(x, t) = 0, \quad (4.3.11a)$$

$$\bar{v}_x(x, t) = \frac{-K_1}{K_1 + k_1}, \quad \bar{v}_y(x, t) = 0, \quad (4.3.11b)$$

$$\bar{c}(x, t) = \frac{c_0}{\sqrt{4\pi t}} \int_{-\infty}^0 \exp\left[-\frac{(x - \zeta)^2}{4t}\right] d\zeta, \quad \text{and} \quad (4.3.11c)$$

$$\bar{p}_M(x, t) = \bar{p}_m(x, t) = -\frac{1}{K_1 + k_1} \int \bar{\mu}(\bar{c}) dx + \text{integration constant}. \quad (4.3.11d)$$

We now assess the stability of this base-state solution with respect to perturbations.

4.4 Stability analysis

The evolution of the perturbations are governed by the following equations:

$$K_1 \frac{\partial \tilde{p}_M}{\partial x} = -\bar{\mu} \tilde{V}_x - \tilde{\mu} \bar{V}_x - \tilde{\mu}, \quad (4.4.1a)$$

$$K_2 \frac{\partial \tilde{p}_M}{\partial y} = -\bar{\mu} \tilde{V}_y, \quad (4.4.1b)$$

$$k_1 \frac{\partial \tilde{p}_m}{\partial x} = -\bar{\mu} \tilde{v}_x - \tilde{\mu} \bar{v}_x - \tilde{\mu}, \quad (4.4.1c)$$

$$k_2 \frac{\partial \tilde{p}_m}{\partial y} = -\bar{\mu} \tilde{v}_y, \quad (4.4.1d)$$

$$\frac{\partial \tilde{v}_x}{\partial x} + \frac{\partial \tilde{v}_y}{\partial y} + \frac{\partial \tilde{V}_x}{\partial x} + \frac{\partial \tilde{V}_y}{\partial y} = 0, \quad \text{and} \quad (4.4.1e)$$

$$\frac{\partial \tilde{c}}{\partial t} + (\tilde{V}_x + \tilde{v}_x) \frac{\partial \tilde{c}}{\partial x} = \frac{\partial^2 \tilde{c}}{\partial x^2} + \frac{\partial^2 \tilde{c}}{\partial y^2}. \quad (4.4.1f)$$

The concentration and the velocity components (V_x , V_y , v_x and v_y) are bounded as $\|\mathbf{x}\| \rightarrow \infty$. However, the pressures, p_M and p_m , can be *un*bounded as $\|\mathbf{x}\| \rightarrow \infty$, which should be evident from equations (4.4.1a)–(4.4.1d). To handle the boundedness of the pressures, we will obtain a reduced set of equations by eliminating the pressures, which will then be employed in the stability analysis. The reduced set of equations can be written as

$$\frac{\partial \bar{\mu}}{\partial x} \left(\frac{\partial \tilde{V}_x}{\partial x} + \frac{\partial \tilde{v}_x}{\partial x} \right) + \bar{\mu} \left(\frac{\partial^2 \tilde{V}_x}{\partial x^2} + \frac{\partial^2 \tilde{v}_x}{\partial x^2} \right) + \left(\frac{K_2 + k_2}{K_1 + k_1} \right) \frac{\partial^2 \tilde{\mu}}{\partial y^2} + \bar{\mu} \left(\frac{K_2}{K_1} \frac{\partial^2 \tilde{V}_x}{\partial y^2} + \frac{k_2}{k_1} \frac{\partial^2 \tilde{v}_x}{\partial y^2} \right) = 0, \quad (4.4.2a)$$

$$\begin{aligned} \frac{\partial \bar{\mu}}{\partial x} \left(\frac{\partial \tilde{V}_x}{\partial x} - \frac{\partial \tilde{v}_x}{\partial x} \right) + \bar{\mu} \left(\frac{\partial^2 \tilde{V}_x}{\partial x^2} - \frac{\partial^2 \tilde{v}_x}{\partial x^2} \right) + \left(\frac{K_2 - k_2}{K_1 + k_1} \right) \frac{\partial^2 \tilde{\mu}}{\partial y^2} + \bar{\mu} \left(\frac{K_2}{K_1} \frac{\partial^2 \tilde{V}_x}{\partial y^2} - \frac{k_2}{k_1} \frac{\partial^2 \tilde{v}_x}{\partial y^2} \right) \\ = 2\beta \bar{\mu} \left(K_1^{-1} \tilde{V}_x - k_1^{-1} \tilde{v}_x \right), \quad \text{and} \end{aligned} \quad (4.4.2b)$$

$$\frac{\partial \tilde{c}}{\partial t} + (\tilde{V}_x + \tilde{v}_x) \frac{\partial \tilde{c}}{\partial x} = \frac{\partial^2 \tilde{c}}{\partial x^2} + \frac{\partial^2 \tilde{c}}{\partial y^2}. \quad (4.4.2c)$$

In order to perform the (linear) stability analysis, we decompose the perturbations into Fourier modes:

$$\left(\tilde{V}_x, \tilde{v}_x, \tilde{c}\right) = (\psi_M(x), \psi_m(x), \phi(x)) \exp[i\omega y + \sigma(t_0)t]. \quad (4.4.3)$$

By substituting equation (4.4.3) into equations (4.4.2a)–(4.4.2c), we obtain the following equations:

$$\left[\frac{d^2}{dx^2} + \frac{1}{\bar{\mu}} \frac{d\bar{\mu}}{dx} \frac{d}{dx} \right] (\psi_M + \psi_m) - \left(\frac{K_2 + k_2}{K_1 + k_1} \right) R\omega^2 \phi - \omega^2 \left(\frac{K_2}{K_1} \psi_M + \frac{k_2}{k_1} \psi_m \right) = 0, \quad (4.4.4a)$$

$$\begin{aligned} & \left[\frac{d^2}{dx^2} + \frac{1}{\bar{\mu}} \frac{d\bar{\mu}}{dx} \frac{d}{dx} \right] (\psi_M - \psi_m) - \left(\frac{K_2 - k_2}{K_1 + k_1} \right) R\omega^2 \phi - \omega^2 \left(\frac{K_2}{K_1} \psi_M - \frac{k_2}{k_1} \psi_m \right) \\ & = 2\beta \left(\frac{\psi_M}{K_1} - \frac{\psi_m}{k_1} \right), \quad \text{and} \end{aligned} \quad (4.4.4b)$$

$$\frac{d^2 \phi}{dx^2} - (\omega^2 + \sigma(t_0)) \phi = \frac{\partial \bar{c}}{\partial x} (\psi_M + \psi_m). \quad (4.4.4c)$$

The above equations can be rearranged to obtain the following convenient form:

$$\left[\frac{d^2}{dx^2} + \frac{1}{\bar{\mu}} \frac{d\bar{\mu}}{dx} \frac{d}{dx} - \frac{\omega^2 K_2 + \beta}{K_1} \right] \psi_M = \left(\frac{K_2}{K_1 + k_1} \right) R\omega^2 \phi - \beta \frac{\psi_m}{k_1}, \quad (4.4.5a)$$

$$\left[\frac{d^2}{dx^2} + \frac{1}{\bar{\mu}} \frac{d\bar{\mu}}{dx} \frac{d}{dx} - \frac{\omega^2 k_2 + \beta}{k_1} \right] \psi_m = \left(\frac{k_2}{K_1 + k_1} \right) R\omega^2 \phi - \beta \frac{\psi_M}{K_1}, \quad \text{and} \quad (4.4.5b)$$

$$\left[\frac{d^2}{dx^2} - \omega^2 - \sigma(t_0) \right] \phi = \frac{\partial \bar{c}}{\partial x} (\psi_M + \psi_m). \quad (4.4.5c)$$

It is important to note that $\beta \geq 0$.

4.4.1 Special case: Isotropic double permeability ($K_1 = K_2 = K$ and $k_1 = k_2 = k$)

For this case, the governing equations can be written as:

$$\left[\frac{d^2}{dx^2} + \frac{1}{\bar{\mu}} \frac{d\bar{\mu}}{dx} \frac{d}{dx} - \left(\omega^2 + \frac{K+k}{Kk} \beta \right) \right] \left(\frac{\psi_M}{K} - \frac{\psi_m}{k} \right) = 0, \quad (4.4.6a)$$

$$\left[\frac{d^2}{dx^2} + \frac{1}{\bar{\mu}} \frac{d\bar{\mu}}{dx} \frac{d}{dx} - \omega^2 \right] (\psi_M + \psi_m) = R\omega^2 \phi, \quad \text{and} \quad (4.4.6b)$$

$$\left[\frac{d^2}{dx^2} - \omega^2 - \sigma(t_0) \right] \phi = \frac{\partial \bar{c}}{\partial x} (\psi_M + \psi_m). \quad (4.4.6c)$$

From the equations, one can conclude that there are no additional instability modes than what are present under the Darcy model. Specifically, β does not appear in the dispersion relation, and hence β will not have any effect on the instability at least in the context of linear stability analysis.

4.4.2 Special case: Isotropic single permeability ($K_1 = K_2 = k_1 = k_2 = k$)

The governing equations in this case reduces to:

$$\left(\frac{d^2}{dx^2} + \frac{1}{\bar{\mu}} \frac{d\bar{\mu}}{dx} \frac{d}{dx} - \frac{\omega^2 k + 2\beta}{k} \right) (\psi_M - \psi_m) = 0, \quad (4.4.7a)$$

$$\left(\frac{d^2}{dx^2} + \frac{1}{\bar{\mu}} \frac{d\bar{\mu}}{dx} \frac{d}{dx} - \omega^2 \right) (\psi_M + \psi_m) = R\omega^2 \phi, \quad \text{and} \quad (4.4.7b)$$

$$\left(\frac{d^2}{dx^2} - \omega^2 - \sigma(t_0) \right) \phi = \frac{\partial \bar{c}}{\partial x} (\psi_M + \psi_m). \quad (4.4.7c)$$

4.4.3 Initial growth rate

We now assess the initial growth of the perturbations under quasi-steady-state approximation. For convenience, we shall denote:

$$\sigma_0 = \sigma(t_0 = 0). \quad (4.4.8)$$

At $t = 0$, the following relations hold:

$$\bar{c}(x) = H(x), \quad \frac{d\bar{c}}{dx} = \delta(x), \quad \text{and} \quad \frac{1}{\bar{\mu}} \frac{d\bar{\mu}}{dx} = R_c \delta(x), \quad (4.4.9)$$

where $\delta(x)$ is the Dirac-delta distribution (i.e., a generalized function) [Lighthill, 1958]. The continuity conditions along $x = 0$ at $t = 0$ are:

$$\psi_M(0^+) = \psi_M(0^-), \quad \left[\bar{\mu} \frac{d\psi_M}{dx} \right]_{0^-}^{0^+} = 0, \quad (4.4.10a)$$

$$\psi_m(0^+) = \psi_m(0^-), \quad \left[\bar{\mu} \frac{d\psi_m}{dx} \right]_{0^-}^{0^+} = 0, \quad (4.4.10b)$$

$$\phi(0^+) = \phi(0^-), \quad \text{and} \quad \left[\frac{d\phi}{dx} \right]_{0^-}^{0^+} = \psi_M(0) + \psi_m(0). \quad (4.4.10c)$$

The solution for $\phi(x)$ can be written as

$$\phi(x) = A_1^- \exp[+\sqrt{\omega^2 + \sigma_0}x] \quad \text{for } x < 0 \quad \text{and} \quad (4.4.11a)$$

$$\phi(x) = A_1^+ \exp[-\sqrt{\omega^2 + \sigma_0}x] \quad \text{for } x > 0. \quad (4.4.11b)$$

The continuity conditions imply that:

$$A_1^- = A_1^+ = -\frac{\psi_M(0) + \psi_m(0)}{2\sqrt{\omega^2 + \sigma_0}}. \quad (4.4.12)$$

To solve for ψ_M , first substitute ψ_m from equation (4.4.5b) into equation (4.4.5a):

$$\begin{aligned} & \left(\frac{d^2}{dx^2} - \frac{\omega^2 K_2 + \beta}{K_1} \right) \left(\frac{d^2}{dx^2} - \frac{\omega^2 k_2 + \beta}{k_1} \right) \psi_M = R \left(\frac{\omega^2 K_2 + \beta}{K_1} (\bar{V}_x + 1) - \frac{\beta}{k_1} (\bar{v}_x + 1) \right) \\ & \left(\frac{d^2}{dx^2} - \frac{\omega^2 k_2 + \beta}{k_1} \right) \phi - \frac{\beta}{k_1} \left\{ R \left(\frac{\omega^2 k_2 + \beta}{k_1} (\bar{v}_x + 1) - \frac{\beta}{K_1} (\bar{V}_x + 1) \right) \phi - \frac{\beta}{K_1} \psi_M \right\}. \end{aligned} \quad (4.4.13)$$

By more simplification, it becomes:

$$\left\{ \frac{d^4}{dx^4} - \left(\frac{\omega^2 K_2 + \beta}{K_1} + \frac{\omega^2 k_2 + \beta}{k_1} \right) \frac{d^2}{dx^2} + \frac{\omega^4 K_2 k_2 + \omega^2 \beta (K_2 + k_2)}{K_1 k_1} \right\} \psi_M = B_\phi \phi, \quad (4.4.14)$$

in which

$$\begin{aligned} \frac{B_\phi}{R} = & \left(\frac{\omega^2 K_2 + \beta}{K_1} (\bar{V}_x + 1) - \frac{\beta}{k_1} (\bar{v}_x + 1) \right) \left(\frac{d^2}{dx^2} - \frac{\omega^2 k_2 + \beta}{k_1} \right) \\ & - \frac{\beta}{k_1} \left(\frac{\omega^2 k_2 + \beta}{k_1} (\bar{v}_x + 1) - \frac{\beta}{K_1} (\bar{V}_x + 1) \right). \end{aligned}$$

The complementary solution for ψ_M in homogeneous form of equation (4.4.14) (i.e., for $B_\phi = 0$) is as

$$(\psi_M)_c = A_2^- \exp[+\sqrt{\nu_1}x] + A_3^- \exp[+\sqrt{\nu_2}x] \quad \text{for } x < 0 \quad \text{and} \quad (4.4.15a)$$

$$(\psi_M)_c = A_2^+ \exp[-\sqrt{\nu_1}x] + A_3^+ \exp[-\sqrt{\nu_2}x] \quad \text{for } x > 0, \quad (4.4.15b)$$

where

$$2 \nu_{1,2} = \frac{\omega^2 K_2 + \beta}{K_1} + \frac{\omega^2 k_2 + \beta}{k_1} \pm \sqrt{\left(\frac{\omega^2 K_2 + \beta}{K_1} - \frac{\omega^2 k_2 + \beta}{k_1} \right)^2 + \frac{4\beta^2}{K_1 k_1}}. \quad (4.4.16)$$

Because of the exponential form of ϕ , the particular solution of ψ_M in the equation (4.4.14) can be written as

$$(\psi_M)_p = B \phi, \quad (4.4.17)$$

in which $B = \frac{A_\phi}{A_\psi}$, where

$$\begin{aligned}\frac{A_\phi}{R} &= \left(\frac{\omega^2 K_2 + \beta}{K_1} (\bar{V}_x + 1) - \frac{\beta}{k_1} (\bar{v}_x + 1) \right) \left(\omega^2 + \sigma_0 - \frac{\omega^2 k_2 + \beta}{k_1} \right) \\ &\quad - \frac{\beta}{k_1} \left(\frac{\omega^2 k_2 + \beta}{k_1} (\bar{v}_x + 1) - \frac{\beta}{K_1} (\bar{V}_x + 1) \right) \quad \text{and} \\ A_\psi &= (\omega^2 + \sigma_0)^2 - \left(\frac{\omega^2 K_2 + \beta}{K_1} + \frac{\omega^2 k_2 + \beta}{k_1} \right) (\omega^2 + \sigma_0) + \frac{\omega^4 K_2 k_2 + \omega^2 \beta (K_2 + k_2)}{K_1 k_1}.\end{aligned}$$

So, $\psi_M = (\psi_M)_c + (\psi_M)_p$ and it is as

$$\psi_M = \begin{cases} BA_1^- \exp[+\sqrt{\omega^2 + \sigma_0}x] + A_2^- \exp[+\sqrt{\nu_1}x] + A_3^- \exp[+\sqrt{\nu_2}x] & \text{for } x < 0 \\ BA_1^+ \exp[-\sqrt{\omega^2 + \sigma_0}x] + A_2^+ \exp[-\sqrt{\nu_1}x] + A_3^+ \exp[-\sqrt{\nu_2}x] & \text{for } x > 0. \end{cases} \quad (4.4.19)$$

The solution for ψ_m is straightforward by using equation (4.4.5a):

$$\frac{\beta}{k_1} \psi_m = \begin{cases} (C_\phi + BC_1 - B(\omega^2 + \sigma_0)) A_1^- \exp[\sqrt{\omega^2 + \sigma_0}x] + (C_1 - \nu_1) A_2^- \exp[+\sqrt{\nu_1}x] \\ \quad + (C_1 - \nu_2) A_3^- \exp[+\sqrt{\nu_2}x] & \text{for } x < 0 \\ (C_\phi + BC_1 - B(\omega^2 + \sigma_0)) A_1^+ \exp[-\sqrt{\omega^2 + \sigma_0}x] + (C_1 - \nu_1) A_2^+ \exp[-\sqrt{\nu_1}x] \\ \quad + (C_1 - \nu_2) A_3^+ \exp[-\sqrt{\nu_2}x] & \text{for } x > 0, \end{cases}$$

where

$$C_\phi = R \left(\frac{\omega^2 K_2 + \beta}{K_1} (\bar{V}_x + 1) - \frac{\beta}{k_1} (\bar{v}_x + 1) \right) \quad \text{and} \quad (4.4.20)$$

$$C_1 = \frac{\omega^2 K_2 + \beta}{K_1}. \quad (4.4.21)$$

The continuity conditions for ψ_M can be written as

$$A_2^- + A_3^- = A_2^+ + A_3^+ \quad \text{and} \quad (4.4.22)$$

$$B\sqrt{\omega^2 + \sigma_0}(\bar{\mu}^- + \bar{\mu}^+)A_1^- + \sqrt{\nu_1}(\bar{\mu}^- A_2^- + \bar{\mu}^+ A_2^+) + \sqrt{\nu_2}(\bar{\mu}^- A_3^- + \bar{\mu}^+ A_3^+) = 0. \quad (4.4.23)$$

The continuity conditions on ψ_m can be written as

$$\nu_1 A_2^- + \nu_2 A_3^- = \nu_1 A_2^+ + \nu_2 A_3^+ \quad \text{and} \quad (4.4.24)$$

$$\begin{aligned} & \sqrt{\omega^2 + \sigma_0} (C_\phi + BC_1 - B(\omega^2 + \sigma_0)) (\bar{\mu}^- + \bar{\mu}^+) A_1^- + \sqrt{\nu_1} (C_1 - \nu_1) (\bar{\mu}^- A_2^- + \bar{\mu}^+ A_2^+) \\ & + \sqrt{\nu_2} (C_1 - \nu_2) (\bar{\mu}^- A_3^- + \bar{\mu}^+ A_3^+) = 0. \end{aligned} \quad (4.4.25)$$

Equations (4.4.22) and (4.4.24) imply that:

$$A_2^- = A_2^+ \quad \text{and} \quad A_3^- = A_3^+. \quad (4.4.26)$$

Equations (4.4.23), (4.4.25) and (4.4.12) then reduce to:

$$B\sqrt{\omega^2 + \sigma_0}A_1^- + \sqrt{\nu_1}A_2^- + \sqrt{\nu_2}A_3^- = 0, \quad (4.4.27)$$

$$\begin{aligned} & \sqrt{\omega^2 + \sigma_0} (C_\phi + BC_1 - B(\omega^2 + \sigma_0)) A_1^- + \sqrt{\nu_1} (C_1 - \nu_1) A_2^- + \sqrt{\nu_2} (C_1 - \nu_2) A_3^- \\ & = 0, \quad \text{and} \end{aligned} \quad (4.4.28)$$

$$\begin{aligned} & \left(B + 2\sqrt{\omega^2 + \sigma_0} + \frac{k_1}{\beta} (C_\phi + BC_1 - B(\omega^2 + \sigma_0)) \right) A_1^- + \left(1 + \frac{k_1}{\beta} (C_1 - \nu_1) \right) A_2^- \\ & + \left(1 + \frac{k_1}{\beta} (C_1 - \nu_2) \right) A_3^- = 0. \end{aligned} \quad (4.4.29)$$

Simplifies the most recent equations to the following form:

$$\begin{bmatrix} B\sqrt{\omega^2 + \sigma_0} & \sqrt{\nu_1} & \sqrt{\nu_2} \\ \sqrt{\omega^2 + \sigma_0}(C_\phi + BC_1 - B(\omega^2 + \sigma_0)) & \sqrt{\nu_1}(C_1 - \nu_1) & \sqrt{\nu_2}(C_1 - \nu_2) \\ B + 2\sqrt{\omega^2 + \sigma_0} + \frac{k_1(C_\phi + BC_1 - B(\omega^2 + \sigma_0))}{\beta} & 1 + \frac{k_1(C_1 - \nu_1)}{\beta} & 1 + \frac{k_1(C_1 - \nu_2)}{\beta} \end{bmatrix} \begin{bmatrix} A_1^- \\ A_2^- \\ A_3^- \end{bmatrix} = \begin{bmatrix} 0 \\ 0 \\ 0 \end{bmatrix}. \quad (4.4.30)$$

For a non-trivial solution, the determinant of the coefficient matrix should be zero.

This gives rise to a nonlinear equation in terms of σ_0 and ω .

4.4.3.1 Special case: Isotropic single permeability

One can obtain the case of isotropic single permeability by taking $K_1 = K_2 = k_1 = k_2 = 1$. Under this case, the coefficients become:

$$\nu_1 = \omega^2, \nu_2 = \omega^2 + 2\beta, C_1 = \omega^2 + \beta, C_\phi = \frac{R\omega^2}{2}, B = \frac{R\omega^2}{2\sigma_0}, \quad (4.4.31)$$

and the system of equations (4.4.30) become:

$$\begin{bmatrix} 0 & 0 & \sqrt{\nu_2} \\ B\sqrt{\omega^2 + \sigma_0} & \omega & 0 \\ B + \sqrt{\omega^2 + \sigma_0} & 1 & 0 \end{bmatrix} \begin{bmatrix} A_1^- \\ A_2^- \\ A_3^- \end{bmatrix} = \begin{bmatrix} 0 \\ 0 \\ 0 \end{bmatrix}. \quad (4.4.32)$$

A non-trivial solution for the concentration in equation (4.4.32) reduces to

$$\begin{vmatrix} \frac{R\omega^2}{2\sigma_0}\sqrt{\omega^2 + \sigma_0} & \omega \\ \frac{R\omega^2}{2\sigma_0} + \sqrt{\omega^2 + \sigma_0} & 1 \end{vmatrix} = 0, \quad (4.4.33)$$

which yields

$$\sigma_0^2 - (R\omega - \omega^2)\sigma_0 + \frac{R^2\omega^2}{4} - R\omega^3 = 0. \quad (4.4.34)$$

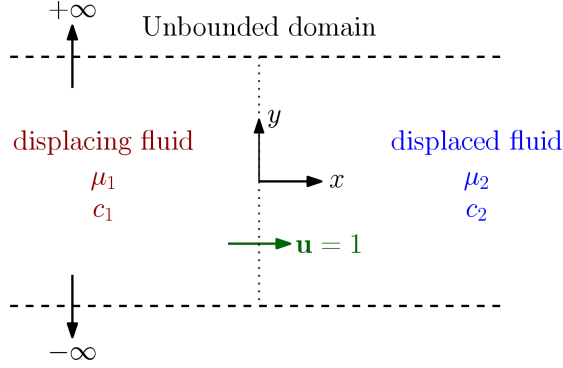


Figure 4.1: Double permeability: Pictorial description of the problem for stability analysis in which the domain is unbounded. The displacing fluid ($\mu_1(c)$ and c_1) flows into the domain which contains displacing fluid (μ_2, c_2).

The solutions take the following form:

$$\sigma_0 = \frac{\omega}{2} \left(R - \omega \pm \sqrt{\omega(\omega + 2R)} \right), \quad (4.4.35)$$

which is the classical dispersion equation for miscible viscous fingering for Darcy equations obtained by [Tan and Homsy, 1986]. An interesting fact to note is that β does not appear in equation (4.4.35), which implies that β does not influence stability under the isotropic single permeability case.

4.4.4 Parametric study for linear stability

In this part, a parametric study for the linear stability is conducted. To do so, we will solve system of equations (4.4.30) to determine the growth rate of associated wavenumbers and plot dispersion curve for ω vs σ_0 . The pictorial description of the rectilinear domain is shown in figure 4.1. First, the effect of double permeability on the stability of viscous fingering by changing K_2 is studied. Then, influence of mass transfer between micro- and macro-network (β) on the stability of system is investigated. Finally, effect of log-mobility (R) on the stability is discussed.

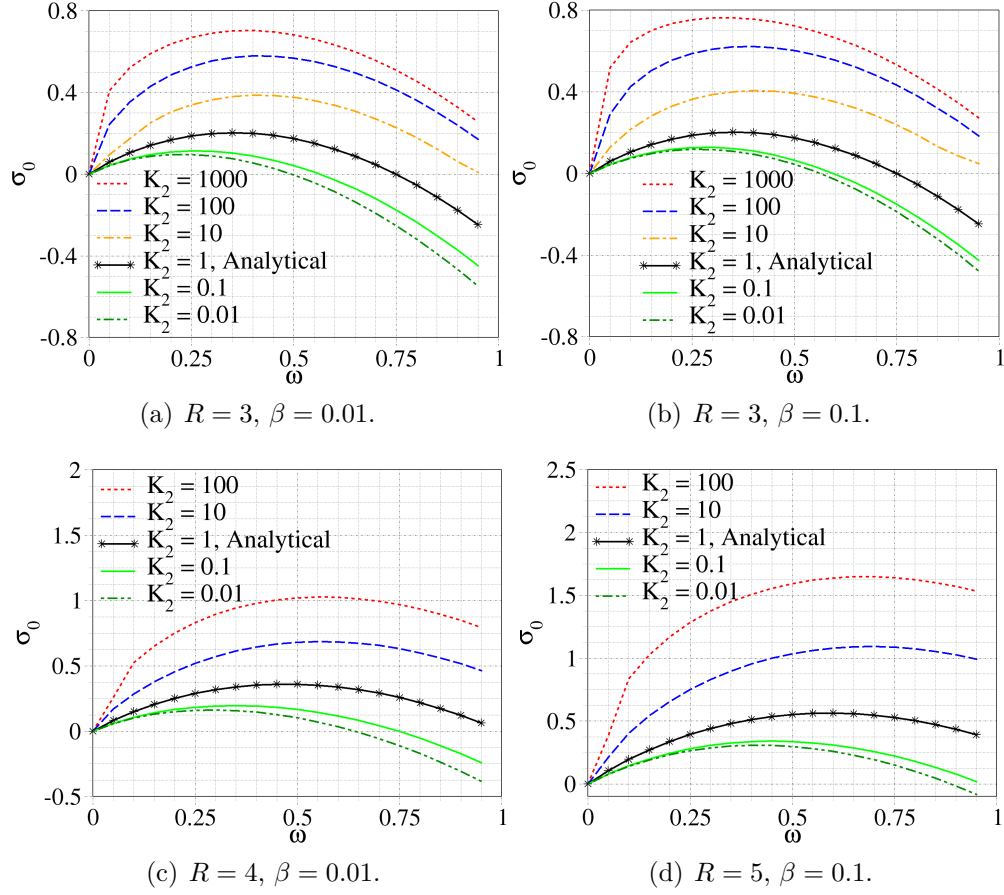


Figure 4.2: Effect of K_2 : The figures show the effect of K_2 on dispersion curve for $\beta = 0.001$ and 0.01 , $K_1 = k_1 = k_2 = 1$, and $R = 3, 4$, and 5 .

4.4.4.1 Effects of K_2

To determine whether the double permeability system is less or more unstable than its equivalent single permeability, the effect of K_2 on the stability of the system at $t_0 = 0$ is necessary. Figure 4.2 shows the effects of K_2 on the dispersion curve at $t_0 = 0$ for various values of β and R . In all cases, for $K_2 = 1$ the results of numerical experiment are right fitted to those from equation (4.4.35) which conform that β does not affect under isotropic single permeability assumption. Instability characteristics for $R = 3, 4$, and 5 when $\beta = 0.01$ and 0.1 show that by increasing K_2 flow becomes more unstable. Figure 4.2 also shows that for $K_2 \leq k_1$, the system is unstable. It means the K_2 in double permeability models is a key parameters and

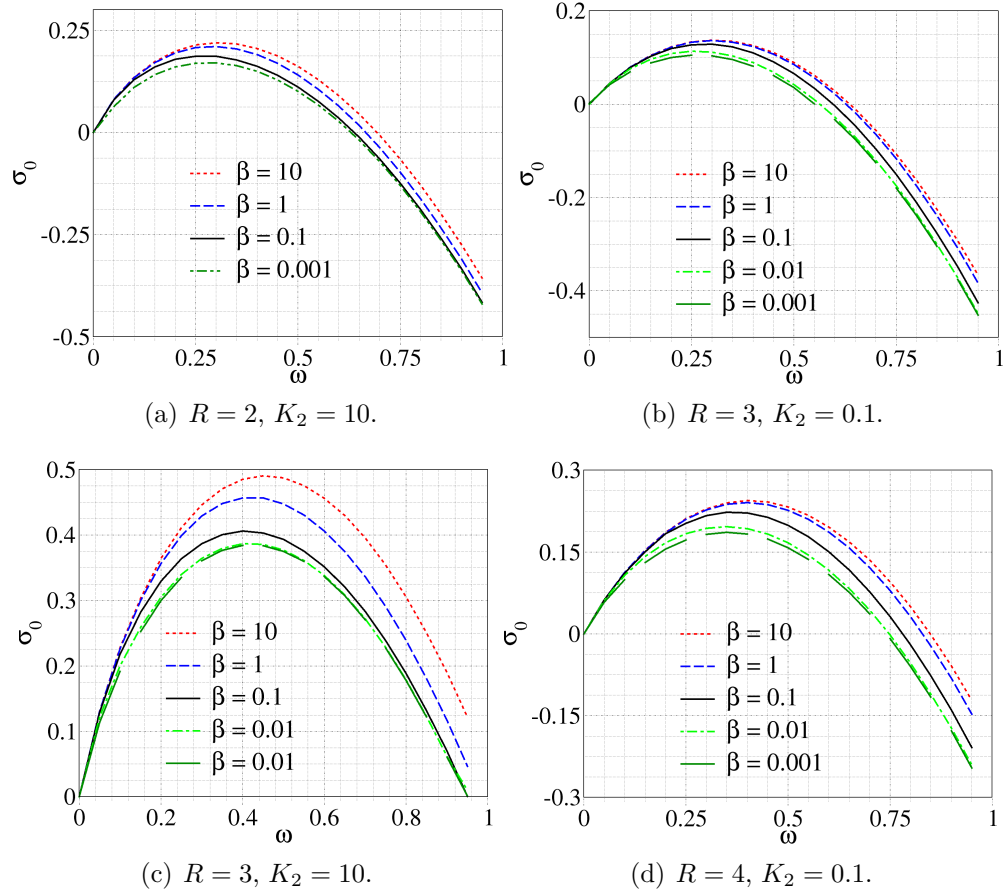


Figure 4.3: Effect of β : The plots show the effect of β on dispersion curve for $K_1 = k_1 = k_2 = 1$, $R = 2, 3$, and 4 , and $K_2 = 0.1$ and 10 .

play an important role in stability of the system.

4.4.4.2 Effects of β

The proposed model for the dual porosity/permeability, allowed mass transfer across micro- and macro-structure. So, in the governing equations, we considered β within the balance of mass equation for both micro- and macro-network which is not a case under single permeability assumption. Figure 4.3 illustrates influence of β on the stability of system at $t_0 = 0$. Herein, an increase of β has a destabilizing effect on the system. Also, for larger values of R and K_2 system is more unstable.

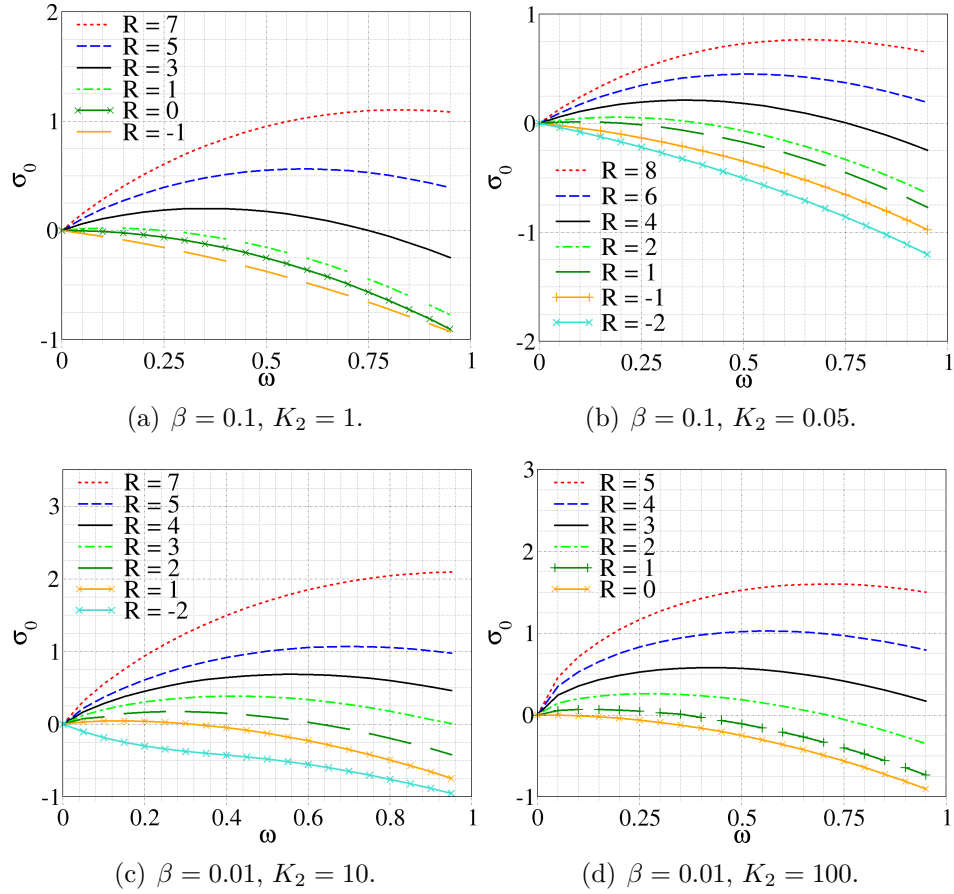


Figure 4.4: Effect of R : The figures show the effect of R on dispersion curve for $\beta = 0.1$ and 0.01 , $K_1 = k_1 = k_2 = 1$, and different K_2 .

4.4.4.3 Effects of R

The log-mobility is a key parameter for observing viscous fingering and miscible displacement in porous medium. It clearly can change the stability conditions for the viscous fingering in a dual porosity/permeability domain. The effect of R are depicted in Figure 4.4. In this case, also by decreasing R the flow becomes less unstable which occurs for single permeability and Darcy models. The significant finding under double permeability assumption is that the flow is fully stabilized for $R < 0$ and further decrease of R (i.e., -1 and -2) maintain a stable system.

4.4.5 Concentration profiles

In this part, we shall illustrate the qualitative results by employing finite element formulations for coupled double permeability porous media flow and transport system given by equations (4.2.1) and (4.2.2a)–(4.2.2d). Pictorial description of the Hele-Shaw problem including boundary and initial conditions is provided in Figure 4.5. The computational domain is a $L_x \times L_y$ rectangle. On the left boundary the normal velocity v_{xM} (in x -direction for macro-network) and concentration c^p are enforced as the injected inflow. Zero velocity (i.e., $v_{xm} = 0$) for micro-network is prescribed on the left boundary. There is a small $w \times L_y$ rectangular region in the left to generate instabilities as initial condition for concentration as

$$c(\mathbf{x}, t = 0) = \begin{cases} \alpha \gamma(\mathbf{x}) \exp[-\frac{x^2}{\zeta^2}] & \text{for } 0 \leq x \leq w \\ 0 & \text{for } x > w, \end{cases}$$

where the function $\gamma(\mathbf{x})$ represents random function ranging from 0 to 1 and exhibits transverse irregularities in concentration. α is the magnitude of the disturbance and ζ can be interpreted as the penetration of disturbance from the front. Both α and ζ have small values relative to unity. The zero fluxes are prescribed on the top and bottom boundaries for the flow in both micro- and macro-structure. The no flux boundary condition is also enforced for AD equations on the right boundary, where the atmosphere pressure is employed for flow in macro-network and zero velocity (i.e., $v_{xm} = 0$) for micro-network.

Now, the time evolution of concentration in broad range of parameters are presented for better understanding of viscous fingering instability in double permeability porous media. We will discuss the effect of K_2 , R , and β on the stability of the system to conform the obtained results for linear stability analysis.

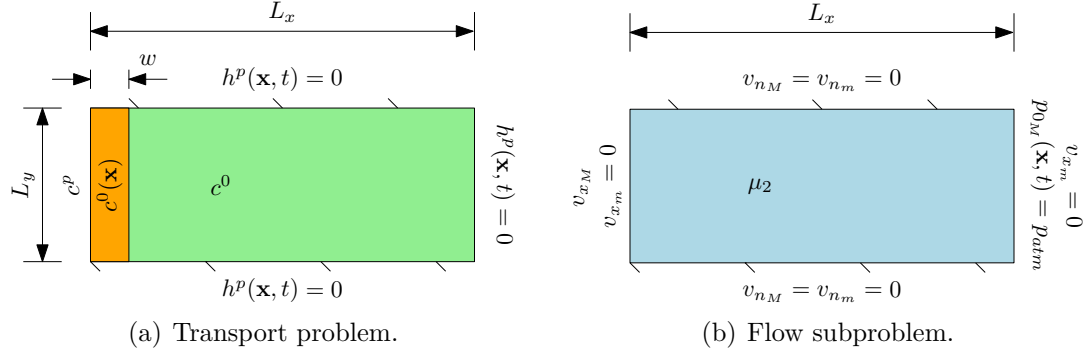


Figure 4.5: Hele-Shaw cell - double permeability: Pictorial description of the problem including boundary and initial conditions. The computational domain is a $L_x \times L_y$ rectangle. The disturbed fluid ($\mu_1(c)$ and c) flows into the domain which contains second flow at rest (μ_2, c^0).

4.4.5.1 Effects of K_2

It has been shown that K_2 has significant effects on the stability of system in linear stability analysis section. Figure 4.6 shows the influence of K_2 on the concentration profiles at different times. We keep β and R to have possible small values of 0.001 and $R = 1.5$, respectively, to investigate the effect of K_2 on the stability of system. Similar to linear stability analysis, by increasing the values of K_2 , the system becomes more unstable.

4.4.5.2 Effects of β

One of the key parameters in double permeability porous media models is mass transfer (β) between micro- and macro-network which is not exist in single permeability models. Increasing the value of β also destabilize the system. Figure 4.7 shows that the concentration profile for $\beta = 10$ is more unstable than the system for $\beta = 0.001$. These numerical simulations performed for $K_2 = 10$ and $R = 4$.

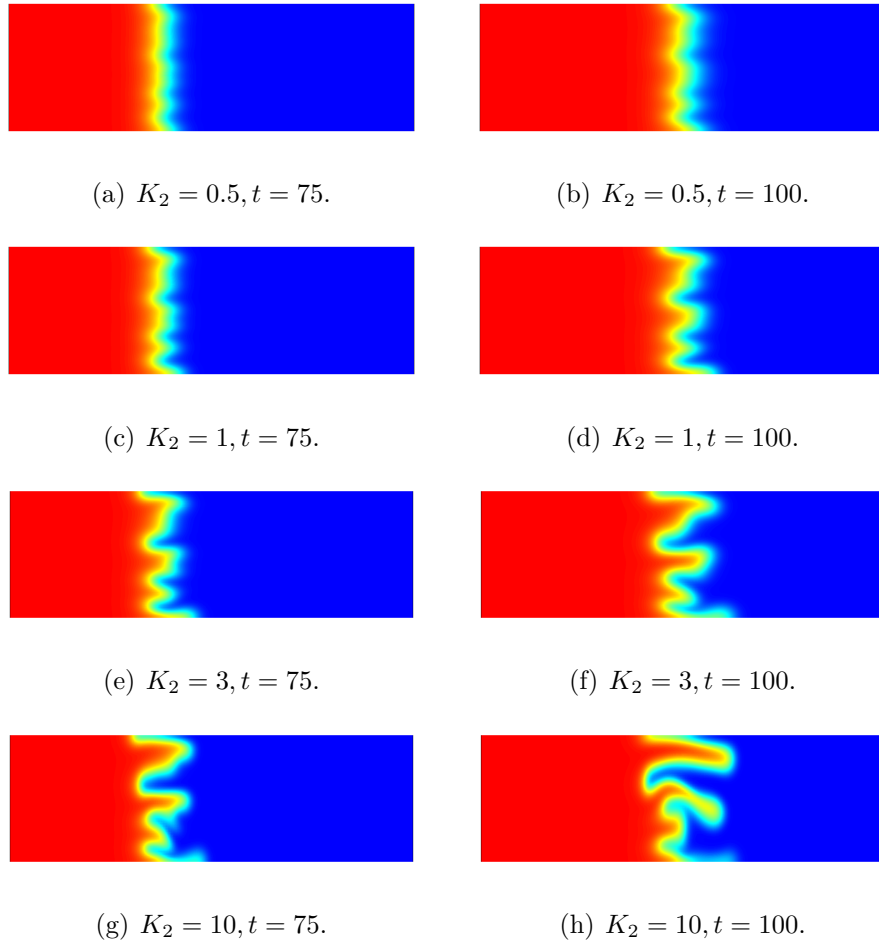


Figure 4.6: Effect of K_2 : The figures show the effect of K_2 on concentration profiles for $\beta = 0.001$, $K_1 = k_1 = k_2 = 1$, and $R = 1.5$. Increasing the values of K_2 destabilize the system.

4.4.5.3 Effects of R

Increasing the values of log-mobility R in both single and double permeability systems have destabilize effects. Figure 4.8 conform the results obtained by linear stability analysis in which larger the values of R make the system less stable. In Figure 4.8 the concentration profiles for $R = 2$ is obviously more stable than the profiles for $R = 4$. Moreover, the linear stability analysis reveals that the system for $R \leq 0$ is stable which is shown for $R = -0.1$. The presented results in this figure is for $K_2 = 2$ and $\beta = 0.001$.

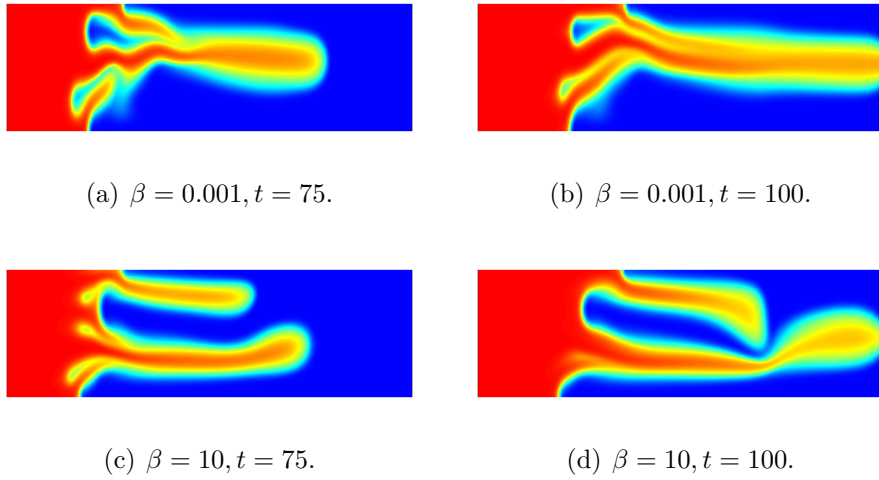


Figure 4.7: Effect of β : The figures show the effect of β on concentration profiles for $R = 4$, $K_1 = k_1 = k_2 = 1$, and $K_2 = 10$. Increasing the values of β also destabilize the system.

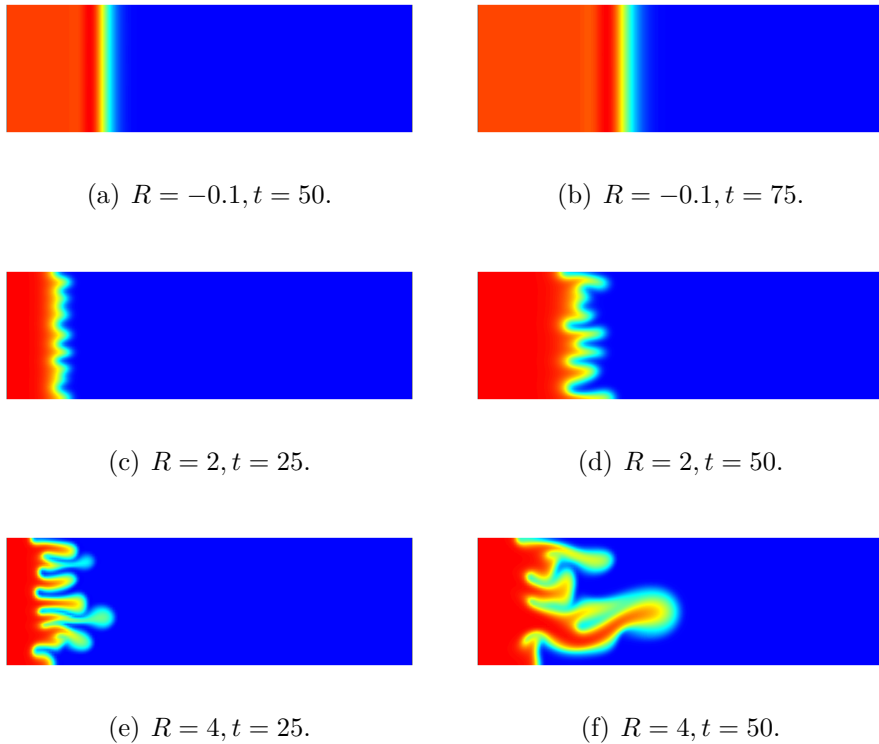


Figure 4.8: Effect of R : The figures show the effect of R on concentration profiles for $\beta = 0.001$, $K_1 = k_1 = k_2 = 1$, and $K_2 = 2$. In this case also, by increasing the values of R the system becomes less stable.

4.5 Concluding remarks

A linear stability analysis and numerical simulations for coupled porous media flow with double permeability and advection-diffusion equations were conducted. The permeability of porous medium is anisotropic for both micro- and macro-network and there is a mass transfer across them. The characterized stability curves were presented for growth rates σ_0 and associated wave numbers ω . Also, from results of numerical solutions, the concentration profiles are shown to study viscous fingering instabilities. We investigated the effects of parameters such as anisotropic double permeability, mass transfer, and log-mobility which play important roles on the stability of viscous fingering. By plotting the dispersion curves and concentration contours, we shown that:

- (a) Larger values for K_2 component of macro-structure permeability make the flow more unstable. In addition, by decreasing the value of K_2 to reach the value of micro-pore permeability (k_1) and even less than that (i.e., $K_2 \leq k_1$), the system is still unstable, but further decreasing makes it stable.
- (b) In the case of $K_1 = K_2 = k_1 = k_2$, the system reduce to isotropic single permeability model and there are no additional instability modes than the model under Darcy equation.
- (c) Increasing mass transfer (β) between micro- and macro-network has a destabilizing effect which is not the case in single permeability (Darcy) model.
- (d) We also shown that for lager value of K_2 and R , the system is more sensitive to β . So, under this condition, by increasing the value of β system becomes more unstable.
- (e) Decreasing the log-mobility R in the system makes the flow more stable which also occurs under the single permeability assumption.

- (f) An interesting result in the case of double permeability is that for $R < 0$ the system is always stable and changing the values of β and K_2 can not destabilize the system.

Chapter 5

CONCLUSION AND FUTURE RESEARCH DIRECTIONS

Nullius in verba.

(no man's word is final)

Motto of the Royal Society of London

We studied numerical and theoretical aspects of the problems from porous media models with applications on coupled multi-physics problems including viscous fingering, miscible displacement, and mixing. We addressed the issues in verification of the numerical solutions for Darcy and Darcy-Brinkman models by proposing a series of new mechanics-based techniques. In addition to numerical solutions verification, the developed methodology is used to identify numerical pollution and check the performance of adaptive mesh. These properties can be effectively used to assess the accuracy of numerical solutions. If the numerical formulation is not converging, one needs to suspect that there are singularities in the solutions or that the numerical formulation does not perform well with respect to the local mass balance property. Another challenging multi-process phenomena in the porous media problems that have been investigated theoretically and numerically, are viscous fingering and miscible displacement. We shown that the double diffusion and double permeability have

significant effects on the dynamics and stability of the coupled porous media flow, transport, and temperature. We also shown that the proposed theoretical reduced order model in current study, is able to comprehensively predict mixing enhancement, mixing time and length. Moreover, we studied the effects of popular numerical stabilized formulations such as SUPG and SOLD and shown that these stabilizers may not resolve the non-negativity in the concentration fields. In addition, the finite element stabilized formulations may suppress the physical viscous fingering instabilities. Also, by developing a linear stability analysis framework for porous media in double permeability, we shown that the mass transfer between micro- and macro-network has significant effects on stability of the double permeability problem, which is not the case in single permeability models. Moreover, the influence of permeability and log-mobility on the stability of the problem were investigated. In addition, by utilizing finite element solutions, the effects of the aforementioned parameters on the stability of flow were performed. We shown that the influence of parameters on concentration profiles were similar to the results of linear stability analysis.

Based on the contributions and developments in current study, the following extensions and research directions are suggested:

1. Extension of solution verification to other numerical methods: The mechanics-based techniques can also be utilized for solution verification of finite volume, finite difference, lattice Boltzmann methods and so forth. Herein, we employed our novel theory for finite element formulations.
2. Verification of other physical models: One can extend this approach to other physical problems such as double porosity/permeability porous media, Stokes or Naveir-Stokes flows, deformation problems, and etc. In current study, our aim was to develop and introduce this new verification methodology, so it employed for problems from flow through porous media.

3. Viscous fingering under modified Darcy model: Disorder in the flow (gradient of velocity) and in the concentration/temperature fields play an important role in hydrodynamic instabilities. On the other hand, the Darcy model neglects the gradient of velocity. An extension to Darcy-Brinkman or Darcy-Forchheimer equations could have better understanding of the instability.
4. Extension to anisotropic diffusivity: Further developments could be in considering more realistic material properties for advection-diffusion problem by using velocity dependent diffusion and anisotropic diffusivity which are an important factors in subsurface hydrology and geological problems.
5. Employment of non-negative formulations: It is possible to employ other forms of finite element formulations to satisfy maximum principle and consequently non-negative constraint for the advection-diffusion equation. This can be done by using proposed methodology in [Mudunuru and Nakshatrala, 2016].

Bibliography

- Aage, N., Poulsen, T. H., Hansen, A. G., and Sigmund, O. (2008). “Topology optimization of large scale Stokes flow problems.” *Structural and Multidisciplinary Optimization*, 35, 175–180.
- Ainsworth, M. and Oden, J. T. (1997). “A posteriori error estimation in finite element analysis.” *Computer Methods in Applied Mechanics and Engineering*, 142, 1–88.
- Almarcha, C., Trevelyan, P. M. J., Grosfils, P., and Wit, A. D. (2013). “Thermal effects on the diffusive layer convection instability of an exothermic acid-base reaction front.” *Physical Review E*, 88, 033009.
- Amaziane, B. and Pankratov, L. (2016). “Homogenization of a model for water–gas flow through double-porosity media.” *Mathematical Methods in the Applied Sciences*, 39, 425–451.
- Arbogast, T., Wheeler, M. F., and Yotov, I. (1997). “Mixed finite elements for elliptic problems with tensor coefficients as cell-centered finite differences.” *SIAM Journal on Numerical Analysis*, 34, 828–852.
- Augustin, M., Caiazzo, A., Fiebach, A., Fuhrmann, J., John, V., Linke, A., and Umla, R. (2011). “An assessment of discretizations for convection-dominated convection–diffusion equations.” *Computer Methods in Applied Mechanics and Engineering*, 200, 3395–3409.
- Azaiez, J. and Singh, B. (2002). “Stability of miscible displacements of shear thinning fluids in a Hele-Shaw cell.” *Physics of Fluids*, 14, 1557–1571.
- Babuška, I., Ihlenburg, F., Strouboulis, T., and Gangaraj, S. K. (1997). “A posteriori error estimation for finite element solutions of Helmholtz equation-Part II:

- Estimation of the pollution error.” *International Journal for Numerical Methods in Engineering*, 40, 3883–3900.
- Babuška, I. and Oden, J. T. (2004). “Verification and validation in computational engineering and science: basic concepts.” *Computer Methods in Applied Mechanics and Engineering*, 193, 4057–4066.
- Babuška, I. and Oh, H.-S. (1987). “Pollution problem of the p - and h - p versions of the finite element method.” *Communications in Applied Numerical Methods*, 3, 553–561.
- Babuška, I. and Strouboulis, T. (2001). *The Finite Element Method and its Reliability*. Oxford University Press, Oxford.
- Babuška, I., Strouboulis, T., Upadhyay, C. S., and Gangaraj, S. K. (1995). “A *posteriori* estimation and adaptive control of the pollution error in the h -version of the finite element method.” *International Journal for Numerical Methods in Engineering*, 38, 4207–4235.
- Bacri, J.-C., Rakotomalala, N., Salin, D., and Woumeni, R. (1992). “Miscible viscous fingering: Experiments versus continuum approach.” *Physics of Fluids*, 4, 1611–1619.
- Balogun, A. S., Kazemi, H., Ozkan, E., Al-Kobaisi, M., and Ramirez, B. A. (2007). “Verification and proper use of water-oil transfer function for dual-porosity and dual-permeability reservoirs.” *SPE Middle East Oil and Gas Show and Conference*, Society of Petroleum Engineers.
- Batchelor, G. K. (2000). *An Introduction to Fluid Dynamics*. Cambridge University Press, New York.

- Becker, R. and Rannacher, R. (2001). “An optimal control approach to *a posteriori* error estimation in finite element methods.” *Acta Numerica*, 10, 1–102.
- Benamou, J.-D. (2014). “Computation of MULTI-VALUED TRAVELTIMES in the Marmousi model, <<http://www.caam.rice.edu/benamou/testproblem.html>>.
- Blottner, F. G. (1990). “Accurate Navier-Stokes results for the hypersonic flow over a spherical nosetip.” *Journal Spacecraft and Rockets*, 27, 113–122.
- Borrvall, T. and Petersson, J. (2003). “Topology optimization of fluids in Stokes flow.” *International Journal for Numerical Methods in Fluids*, 41, 77–107.
- Botella, O. and Peyret, R. (1998). “Benchmark spectral results on the lid-driven cavity flow.” *Computers and Fluids*, 27, 421–433.
- Botella, O. and Peyret, R. (2001). “Computing singular solutions of the Navier-Stokes equations with the Chebyshev-collocation method.” *International Journal for Numerical Methods in Fluids*, 36, 125–163.
- Boutin, C. and Royer, P. (2015). “On models of double porosity poroelastic media.” *Geophysical Journal International*, 203, 1694–1725.
- Bowen, R. M. (1976). “Theory of mixtures.” *Continuum Physics*, A. C. Eringen, ed., Vol. III, Academic Press, New York.
- Brezzi, F. and Fortin, M. (1991). *Mixed and Hybrid Finite Element Methods, volume 15 of Springer series in computational mathematics*. Springer-Verlag, New York.
- Brezzi, F., Hughes, T. J. R., Marini, L. D., and Masud, A. (2005a). “Mixed discontinuous Galerkin method for Darcy flow.” *SIAM Journal on Scientific Computing*, 22, 119–145.

- Brezzi, F., Lipnikov, K., and Shashkov, M. (2005b). “Convergence of the mimetic finite difference method for diffusion problems on polyhedral meshes.” *SIAM Journal on Numerical Analysis*, 43, 1872–1896.
- Brinkman, H. C. (1947a). “A calculation of the viscous force exerted by a flowing fluid on a dense swarm of particles.” *Applied Scientific Research*, A1, 27–34.
- Brinkman, H. C. (1947b). “On the permeability of the media consisting of closely packed porous particles.” *Applied Scientific Research*, A1, 81–86.
- Brooks, A. N. and Hughes, T. J. R. (1982). “Streamline-upwind/Petrov-Galerkin methods for convection dominated flows with emphasis on the incompressible Navier-Stokes equations.” *Computer Methods in Applied Mechanics and Engineering*, 32, 199–259.
- Burggraf, O. R. (1966). “Analytical and numerical studies of the structure of steady separated flows.” *Journal of Fluid Mechanics*, 24, 113–151.
- Burman, E. and Hansbo, P. (2007). “A unified stabilized method for Stokes’ and Darcy’s equations.” *Journal of Computational and Applied Mathematics*, 198, 35–51.
- C-Landeira, J., Trevelyan, P. M. J., Almarcha, C., and Wit, A. D. (2013). “Mixed-mode instability of a miscible interface due to coupling between Rayleigh-Taylor and double-diffusive convective modes.” *Physics of Fluids*, 25, 024107.
- Castro, R. G. S., Malta, S. M. C., Loula, A. F. D., and Landau, L. (2001). “Numerical analysis of space-time finite element formulations for miscible displacements.” *Computational Geosciences*, 5, 301–330.
- Challis, V. J. and Guest, J. K. (2009). “Level set topology optimization of fluids

- in Stokes flow.” *International Journal for Numerical Methods in Engineering*, 79, 1284–1308.
- Chan, C. K. and Liang, N. Y. (1997). “Observations of surfactant driven instability in a Hele-Shaw cell.” *Physical Review Letters*, 79, 4381.
- Chavent, G., Cohen, G., and Jaffre, J. (1984). “Discontinuous upwinding and mixed finite element for two-phase flows in reservoir simulation.” *Computer Methods in Applied Mechanics and Engineering*, 47, 93–118.
- Chen, C.-Y. and Meiburg, E. (1998). “Miscible porous media displacements in the quarter five-spot configuration. Part 2. Effect of heterogeneities.” *Journal of Fluid Mechanics*, 371, 269–299.
- COMSOL Multiphysics (2013). *User’s Guide, Version 4.3b*. COMSOL, Inc., Burlington, Massachusetts, www.comsol.com.
- Coutinho, A. L. G. A. and Alves, J. L. D. (1999). “Finite element simulation of nonlinear viscous fingering in miscible displacements with anisotropic dispersion and nonmonotonic viscosity profiles.” *Computational Mechanics*, 23, 108–116.
- Darcy, H. (1856). *Les Fontaines Publiques de la Ville de Dijon*. Victor Dalmont, Paris.
- de Boer, R. (2000). *Theory of Porous Media: Highlights in the Historical Development and Current State*. Springer-Verlag, New York.
- de Bruyn, J. R. (1995). “Fingering instability of gravity currents in thin-layer electrochemical deposition.” *Physical Review Letters*, 74, 4843.
- Dias, C. M. and Coutinho, A. L. G. A. (2004). “Stabilized finite element methods with reduced integration techniques for miscible displacements in porous media.” *International journal for numerical methods in engineering*, 59, 475–492.

- Durlofsky, L. J. (1994). “Accuracy of mixed and control volume finite element approximations to Darcy velocity and related quantities.” *Water Resources Research*, 30, 965–973.
- Dykhuizen, R. C. (1990). “A new coupling term for dual-porosity models.” *Water Resources Research*, 26, 351–356.
- Erturk, E. (2009). “Discussions on driven cavity flow.” *International Journal for Numerical Methods in Fluids*, 60, 275–294.
- Evans, L. C. (1998). *Partial Differential Equations*. American Mathematical Society, Providence, Rhode Island.
- Ewing, R. E. and Heinemann, R. F. (1984). “Mixed finite element approximation of phase velocities in compositional reservoir simulation.” *Computer Methods in Applied Mechanics and Engineering*, 47, 161–175.
- Fernandez, J. and Homsy, G. M. (2003). “Viscous fingering with chemical reaction: effect of *in-situ* production of surfactants.” *Journal of Fluid Mechanics*, 480, 267–281.
- Ghesmat, K. and Azaiez, J. (2008). “Viscous fingering instability in porous media: effect of anisotropic velocity-dependent dispersion tensor.” *Transport in Porous Media*, 73, 297–318.
- Gilbarg, D. and Trudinger, N. S. (2001). *Elliptic Partial Differential Equations of Second Order*. Springer, New York.
- Gresho, P. M. and Sani, R. L. (2000). *Incompressible Flow and the Finite Element Method: Advection-Diffusion*, Vol. 1. John Wiley & Sons, Inc., Chichester, UK.
- Guazzelli, E. and Morris, J. F. (2012). *A Physical Introduction to Suspension Dynamics*. Cambridge University Press, Cambridge.

- Hansen, A. G., Sigmund, O., and Haber, R. B. (2005). “Topology optimization of channel flow problems.” *Structural and Multidisciplinary Optimization*, 30, 181–192.
- Hassine, M. (2012). “Topology Optimization of Fluid Mechanics Problems.” *Advanced Methods for Practical Applications in Fluid Mechanics*, S. A. Jones, ed., InTech, 209–230.
- Hejazi, S. H., Trevelyan, P. M. J., Azaiez, J., and Wit, A. D. (2010). “Viscous fingering of a miscible reactive $A + B \rightarrow C$ interface: A linear stability analysis.” *Journal of Fluid Mechanics*, 652, 501–528.
- Heller, J. P. (1966). “Onset of instability patterns between miscible fluids in porous media.” *Journal of Applied Physics*, 37, 1566–1579.
- Hill, S. (1952). “Channeling in packed columns.” *Chemical Engineering Science*, 1, 247–253.
- Homsy, G. M. (1987). “Viscous fingering in porous media.” *Annual Review of Fluid Mechanics*, 19, 271–311.
- Hornung, U. (1996). *Homogenization and Porous Media*. Springer-Verlag, New York.
- Hughes, T. J. R., Franca, L., and Balestra, M. (1986a). “A new finite element formulation for computational fluid dynamics: V. Circumventing the Babuska-Brezzi condition: A stable Petrov-Galerkin formulation of the Stokes problem accommodating equal-order interpolations.” *Computer Methods in Applied Mechanics and Engineering*, 59, 85–99.
- Hughes, T. J. R., Mallet, M., and Akira, M. (1986b). “A new finite element formulation for computational fluid dynamics: II. Beyond SUPG.” *Computer Methods in Applied Mechanics and Engineering*, 54, 341–355.

- Islam, M. N. and Azaiez, J. (2005). “Fully implicit finite difference pseudo-spectral method for simulating high mobility-ratio miscible displacements.” *International Journal for Numerical Methods in Fluids*, 47, 161–183.
- Islam, M. N. and Azaiez, J. (2007). “New viscous fingering mechanisms at high viscosity ratio and Péclet number miscible displacements.” *Journal of Porous Media*, 10, 357–375.
- Islam, M. N. and Azaiez, J. (2010a). “Miscible thermo-viscous fingering instability in porous media. Part 1: Linear stability analysis.” *Transport in Porous Media*, 84, 821–844.
- Islam, M. N. and Azaiez, J. (2010b). “Miscible thermo-viscous fingering instability in porous media. Part 2: Numerical simulations.” *Transport in Porous Media*, 84, 845–861.
- Jha, B., C-Felgueroso, L., and Juanes, R. (2011). “Quantifying mixing in viscously unstable porous media flows.” *Physical Review E*, 84, 066312.
- Jha, B., C-Felgueroso, L., and Juanes, R. (2013). “Synergetic fluid mixing from viscous fingering and alternating injection.” *Physical Review Letters*, 111, 144501.
- John, V. and Knobloch, P. (2007). “On spurious oscillations at layers diminishing (SOLD) methods for convection–diffusion equations: Part I – A review.” *Computer Methods in Applied Mechanics and Engineering*, 196, 2197–2215.
- Johnson, C., Schatz, A. H., and Wahlbin, L. B. (1987). “Crosswind smear and pointwise errors in streamline diffusion finite element methods.” *Mathematics of Computation*, 49, 25–38.
- Karimi, S. and Nakshatrala, K. B. (2016). “Do current lattice Boltzmann methods for diffusion-type equations respect maximum principles and the

- non-negative constraint?.” *Communications in Computational Physics*, DOI: 10.4208/cicp.181015.270416a.
- Kellogg, O. D. (2010). *Foundations of Potential Theory*. Dover Publications, New York.
- Klimes, L. (2014). “Seismic Waves in Complex 3-D Structures (SW3D), Marmousi model and data set, Department of Geophysics, Charles University in Prague, <<http://seis.karlov.mff.cuni.cz/software/marmousi/marmousi.htm>>.
- Knupp, P. M. and Salari, K. (2003). *Verification of Computer Codes in Computational Science and Engineering*. Chapman & Hall/CRC, Boca Raton.
- Lee, S. H., Yang, M., Song, Y. S., Kim, S. Y., and Youn, J. R. (2009). “Three-dimensional flow simulation of resin transfer molding utilizing multilayered fiber preform.” *Journal of Applied Polymer Science*, 114, 1803–1812.
- Lewis, D. J. (1950). “The instability of liquid surfaces when accelerated in a direction perpendicular to their planes. II.” *Proceedings of the Royal Society of London A: Mathematical, Physical and Engineering Sciences*, The Royal Society, 202, 81–96.
- Li, J. and Riviere, B. (2015). “High order discontinuous Galerkin method for simulating miscible flooding in porous media.” *Computational Geosciences*, 19, 1–18.
- Lighthill, M. J. (1958). *An Introduction to Fourier Analysis and Generalised Functions*. Cambridge University Press, Cambridge, U.K.
- Liska, R. and Shashkov, M. (2008). “Enforcing the discrete maximum principle for linear finite element solutions of second-order elliptic problems.” *Communications in Computational Physics*, 3, 852–877.
- Maes, R., Rousseaux, G., Scheid, B., Mishra, M., Colinet, P., and Wit, A. D. (2010).

- “Experimental study of dispersion and miscible viscous fingering of initially circular samples in Hele-Shaw cells.” *Physics of Fluids*, 22, 123104.
- Masud, A. and Hughes, T. J. R. (2002). “A stabilized mixed finite element method for Darcy flow.” *Computer Methods in Applied Mechanics and Engineering*, 191, 4341–4370.
- Meng, X. and Guo, Z. (2015). “Multiple-relaxation-time lattice Boltzmann model for incompressible miscible flow with large viscosity ratio and high Péclet number.” *Physical Review E*, 92, 043305.
- Minkoff, S. E., Stone, C. M., Bryant, S., Peszynska, M., and Wheeler, M. F. (2003). “Coupled fluid flow and geomechanical deformation modeling.” *Journal of Petroleum Science and Engineering*, 38, 37–56.
- Mishra, M., Trevelyan, P. M. J., Almarcha, C., and Wit, A. D. (2010). “Influence of double diffusive effects on miscible viscous fingering.” *Physical Review Letters*, 105, 204501.
- Mishra, M., Wit, A. D., and Sahu, K. C. (2012). “Double diffusive effects on pressure-driven miscible displacement flows in a channel.” *Journal of Fluid Mechanics*, 712, 579–597.
- Moissis, D. E., Miller, C. A., and Wheeler, M. F. (1988). “A parametric study of viscous fingering in miscible displacement by numerical simulation.” *Numerical Simulation in Oil Recovery*, 11, 227–247.
- Mudunuru, M. K. and Nakshatrala, K. B. (2016). “On enforcing maximum principles and achieving element-wise species balance for advection-diffusion-reaction equations under the finite element method.” *Journal of Computational Physics*, 305, 448–493.

- Mudunuru, M. K., Shabouei, M., and Nakshatrala, K. B. (2015). “On local and global species conservation errors for nonlinear ecological models and chemical reacting flows.” *ASME 2015 International Mechanical Engineering Congress and Exposition*, V009T12A018.
- Munaf, D., Lee, D., Wineman, A. S., and Rajagopal, K. R. (1993). “A boundary value problem in groundwater motion analysis - Comparison of predictions based on Darcy’s law and the continuum theory of mixtures.” *Mathematical Models and Methods in Applied Sciences*, 3, 231–248.
- Nagatsu, Y., Fujita, N., Kato, Y., and Tada, Y. (2009). “An experimental study of non-isothermal miscible displacements in a Hele-Shaw cell.” *Experimental Thermal and Fluid Science*, 33, 695–705.
- Nagatsu, Y. and Wit, A. D. (2011). “Viscous fingering of a miscible reactive $a + b \rightarrow c$ interface for an infinitely fast chemical reaction: Nonlinear simulations.” *Physics of Fluids*, 23, 043103.
- Nakshatrala, K. B., Joodat, S. H. S., and Ballarini, R. (2016a). “Modeling flow in porous media with double porosity/permeability: Mathematical model, properties, and analytical solutions.” *Available on arXiv: 1605.07658*.
- Nakshatrala, K. B., Mudunuru, M. K., and Valocchi, A. J. (2013). “A numerical framework for diffusion-controlled bimolecular-reactive systems to enforce maximum principles and the non-negative constraint.” *Journal of Computational Physics*, 253, 278–307.
- Nakshatrala, K. B., Nagarajan, H., and Shabouei, M. (2016b). “A numerical methodology for enforcing maximum principles and the non-negative constraint for transient diffusion equations.” *Communications in Computational Physics*, 19, 53–93.

- Nakshatrala, K. B. and Rajagopal, K. R. (2011). “A numerical study of fluids with pressure-dependent viscosity flowing through a rigid porous medium.” *International Journal for Numerical Methods in Fluids*, 67, 342–368.
- Nakshatrala, K. B., Turner, D. Z., Hjelmstad, K. D., and Masud, A. (2006). “A stabilized mixed finite element formulation for Darcy flow based on a multiscale decomposition of the solution.” *Computer Methods in Applied Mechanics and Engineering*, 195, 4036–4049.
- Nicolaides, C., Jha, B., C-Felgueroso, L., and Juanes, R. (2015). “Impact of viscous fingering and permeability heterogeneity on fluid mixing in porous media.” *Water Resources Research*, 51, 2634–2647.
- Norouzi, M. and Shoghi, M. R. (2014). “A numerical study on miscible viscous fingering instability in anisotropic porous media.” *Physics of Fluids*, 26, 084102.
- Oberkampf, W. L. and Blottner, F. G. (1998). “Issues in computational fluid dynamics: Code verification and validation.” *AIAA Journal*, 36, 687–695.
- Oberkampf, W. L., Trucano, T. G., and Hirsch, C. (2004). “Verification, validation, and predictive capability in computational engineering and physics.” *Applied Mechanics Reviews*, 57, 345–384.
- Oden, J. T., Feng, Y., and Prudhomme, S. (1998). “Local and pollution error estimation for Stokesian flows.” *International Journal for Numerical Methods in Fluids*, 27, 33–39.
- Pal, R. K., Abedi, R., Madhukar, A., and Haber, R. B. (2016). “Adaptive space-time discontinuous Galerkin method for hyperbolic advection–diffusion with a non-negativity constraint.” *International Journal for Numerical Methods in Engineering*, 105, 963–989.

- Pao, C. V. (1993). *Nonlinear Parabolic and Elliptic Equations*. Springer-Verlag, New York, USA.
- Petitjeans, P. and Maxworthy, T. (1996). “Miscible displacements in capillary tubes. Part 1. Experiments.” *Journal of Fluid Mechanics*, 326, 37–56.
- Pingen, G., Evgrafov, A., and Maute, K. (2009). “Adjoint parameter sensitivity analysis for the hydrodynamic lattice Boltzmann method with applications to design optimization.” *Computers and Fluids*, 38, 910–923.
- Potier, C. L. (2005). “Finite volume monotone scheme for highly anisotropic diffusion operators on unstructured triangular meshes.” *Comptes Rendus Mathematique*, 341, 787–792.
- Pramanik, S. and Mishra, M. (2013). “Linear stability analysis of Korteweg stresses effect on miscible viscous fingering in porous media.” *Physics of Fluids*, 25, 074104.
- Pritchard, D. (2004). “The instability of thermal and fluid fronts during radial injection in a porous medium.” *Journal of Fluid Mechanics*, 508, 133–163.
- Pritchard, D. (2009). “The linear stability of double-diffusive miscible rectilinear displacements in a Hele-Shaw cell.” *European Journal of Mechanics-B/Fluids*, 28, 564–577.
- Protter, M. H. and Weinberger, H. F. (2012). *Maximum Principles in Differential Equations*. Springer Science & Business Media, New York.
- Raats, P. A. C. (1984). *Applications of the theory of mixtures in soil physics*. Springer, New York.
- Raghavan, R. and Marsden, S. S. (1971). “The stability of immiscible liquid layers in a porous medium.” *Journal of Fluid Mechanics*, 48, 143–159.

- Riaz, A. and Tchelepi, H. A. (2004). “Linear stability analysis of immiscible two-phase flow in porous media with capillary dispersion and density variation.” *Physics of Fluids*, 16, 4727–4737.
- Riaz, A. and Tchelepi, H. A. (2006). “Numerical simulation of immiscible two-phase flow in porous media.” *Physics of Fluids*, 18, 014104.
- Riviere, B. and Wheeler, M. F. (2002). “Discontinuous Galerkin methods for flow and transport problems in porous media.” *Communications in Numerical Methods in Engineering*, 18, 63–68.
- Roache, P. J. (1997). “Quantification of uncertainty in computational fluid dynamics.” *Annual Review of Fluid Mechanics*, 29, 123–160.
- Roache, P. J. (1998). *Verification and Validation in Computational Science and Engineering*. Hermosa Publishers, New Mexico.
- Roy, C. J., Nelson, C. C., Smith, T. M., and Ober, C. C. (2004). “Verification of Euler/Navier-Stokes codes using the method of manufactured solutions.” *International Journal for Numerical Methods in Fluids*, 44, 599–620.
- Sadd, M. H. (2009). *Elasticity: Theory, Applications, and Numerics*. Academic Press, Burlington, Massachusetts.
- Saffman, P. G. (1986). “Viscous fingering in Hele-Shaw cells.” *Journal of Fluid Mechanics*, 173, 73–94.
- Saffman, P. G. and Taylor, G. (1958). “The penetration of a fluid into a porous medium or Hele-Shaw cell containing a more viscous liquid.” *Proceedings of the Royal Society of London A*, The Royal Society, 245, 312–329.
- Sajjadi, M. and Azaiez, J. (2013). “Scaling and unified characterization of flow instabilities in layered heterogeneous porous media.” *Physical Review E*, 88, 033017.

- Salari, K. and Knupp, P. M. (2000). “Code Verification by the Method of Manufactured Solutions.” *Report No. SAND2000-1444*, Sandia National Laboratories, Albuquerque.
- Scovazzi, G., Huang, H., Collis, S. S., and Yin, J. (2013). “A fully-coupled upwind discontinuous Galerkin method for incompressible porous media flows: High-order computations of viscous fingering instabilities in complex geometry.” *Journal of Computational Physics*, 252, 86–108.
- Shabouei, M. and Nakshatrala, K. B. (2016). “Mechanics-based solution verification for porous media models.” *Accepted in Communications in Computational Physics. Available on arXiv: 1501.02581*.
- Sheorey, T. and Muralidhar, K. (2003). “Isothermal and non-isothermal oil-water flow and viscous fingering in a porous medium.” *International Journal of Thermal Sciences*, 42, 665–676.
- Srinivasan, S. and Nakshatrala, K. B. (2012). “A stabilized mixed formulation for unsteady Brinkman equation based on the method of horizontal lines.” *International Journal for Numerical Methods in Fluids*, 68, 642–670.
- Steinberg, S. and Roache, P. J. (1985). “Symbolic manipulation and computational fluid dynamics.” *Journal of Computational Physics*, 57, 251–284.
- Tan, C. T. and Homsy, G. M. (1986). “Stability of miscible displacements in porous media: Rectilinear flow.” *Physics of Fluids*, 29, 3549–3556.
- Tan, C. T. and Homsy, G. M. (1987). “Stability of miscible displacements in porous media: Radial source flow.” *Physics of Fluids*, 30, 1239–1245.
- Tan, C. T. and Homsy, G. M. (1988). “Simulation of nonlinear viscous fingering in miscible displacement.” *Physics of Fluids*, 31, 1330–1338.

- Tan, C. T. and Homsy, G. M. (1992). “Viscous fingering with permeability heterogeneity.” *Physics of Fluids*, 4, 1099–1101.
- Taylor, G. (1950). “The instability of liquid surfaces when accelerated in a direction perpendicular to their planes. I.” *Proceedings of the Royal Society of London A: Mathematical, Physical and Engineering Sciences*, The Royal Society, 201, 192–196.
- Trevelyan, P. M. J., Almarcha, C., and Wit, A. D. (2011). “Buoyancy-driven instabilities of miscible two-layer stratifications in porous media and Hele-Shaw cells.” *Journal of Fluid Mechanics*, 670, 38–65.
- Truesdell, C. and Noll, W. (2004). *The Non-Linear Field Theories of Mechanics*. Springer, Berlin, third edition.
- Turner, D. Z., Nakshatrala, K. B., and Hjelmstad, K. D. (2006). “Finite element approach to composite mold design based on Darcy flow with velocity clipping.” *Polymer Composites*, 27, 65–70.
- Versteeg, R. J. (1993). “Sensitivity of prestack depth migration to the velocity model.” *Geophysics*, 58, 873–882.
- Versteeg, R. J. and Grau, G. (1990). “The Marmousi experience.” *Practical aspects of seismic data inversion*, European Association of Exploration Geophysicists, EAEG Workshop, 52nd EAEG Meeting, Copenhagen, 1–194.
- Versteeg, R. J. and Lailly, P. (1991).” *Practical aspects of seismic data inversion*, European Association of Exploration Geophysicists, EAEG workshop report: First Break, 75–80.
- Vogel, T., Gerke, H. H., Zhang, R., and Genuchten, M. V. (2000). “Modeling flow

- and transport in a two-dimensional dual-permeability system with spatially variable hydraulic properties.” *Journal of Hydrology*, 238, 78–89.
- Wit, A. D., Bertho, Y., and Martin, M. (2005). “Viscous fingering of miscible slices.” *Physics of Fluids*, 17, 054114.
- Wit, A. D. and Homsy, G. M. (1997). “Viscous fingering in periodically heterogeneous porous media. I. Formulation and linear instability.” *The Journal of chemical physics*, 107, 9609–9618.
- Zik, O., Olami, Z., and Moses, E. (1998). “Fingering instability in combustion.” *Physical Review Letters*, 81, 3868.
- Zimmerman, W. B. and Homsy, G. M. (1991). “Nonlinear viscous fingering in miscible displacement with anisotropic dispersion.” *Physics of Fluids*, 3, 1859–1872.
- Zimmerman, W. B. and Homsy, G. M. (1992a). “Three-dimensional viscous fingering: A numerical study.” *Physics of Fluids*, 4, 1901–1914.
- Zimmerman, W. B. and Homsy, G. M. (1992b). “Viscous fingering in miscible displacements: Unification of effects of viscosity contrast, anisotropic dispersion, and velocity dependence of dispersion on nonlinear finger propagation.” *Physics of Fluids*, 4, 2348–2359.